Ph.D. DISSERTATION

EXPERIMENTAL STUDY ON NANOPARTICLE-BASED HIGH CURRENT DENSITY CATHODE FOR TERAHERTZ DEVICES

테라헤르츠장치를 위한 나노입자기반의 높은 전류 밀도 음극에 관한 실험적 연구

BY
RANJAN KUMAR BARIK

AUGUST 2014

DEPARTMENT OF ELECTRICAL ENGINEERING AND COMPUTER SCIENCE

SEOUL NATIONAL UNIVERSITY

공학박사 학위논문

EXPERIMENTAL STUDY ON NANOPARTICLE-BASED HIGH CURRENT DENSITY CATHODE FOR TERAHERTZ DEVICES

테라헤르츠장치를 위한 나노입자기반의 높은 전류 밀도 음극에 관한 실험적 연구

2014 년 8 월

서울대학교 대학원

전기·컴퓨터 공학부

란잔 쿠말 바릭

EXPERIMENTAL STUDY ON NANOPARTICLE-BASED HIGH CURRENT DENSITY CATHODE FOR TERAHERTZ DEVICES

Supervised by

Professor Gun-Sik Park

Submitting a doctoral thesis of Electrical Engineering

August 2014

Department of Electrical Engineering and Computer Science

Seoul National University

Ranjan Kumar Barik

Confirming the doctoral thesis written by

Ranjan Kumar Barik

August 2014

Chair Nam, Sangwook (Seal)

Vice Chair Park, Gun-Sik (Seal)

Examiner Lee, Byoungho (Seal)

Examiner Kim, Yong Hyup (Seal)

Examiner Jeong, Young-Uk (Seal)

Abstract

Vacuum electron devices (VED) in terahertz (THz) regime demand a high current density beam, which can be generated from a cathode capable of delivering current density close to 100A/cm^2. A conventional impregnated cathode (B-type) can produce current density of about 10A/cm^2. Therefore, the development of a high current density electron source with a high emission uniformity in a miniature size is a challenge.

The primary aim of this thesis work is to design and development of a dispenser cathode using nanotechnology that could deliver current density up to 100A/cm^2 for use in a THz VED. Theoretical studies were carried out on the influence of various cathode parameters such as surface roughness, porosity, pore geometry, pore distribution, inter-pore connectivity and thermal aspects with a view to understand the emission mechanism and to improve emission capability. The analytical results show that the emission is influenced by particle morphology, its size, homogeneous doping, and particle distribution. Accordingly, a chemical process was developed to make nanopowder with its particles closely meeting the above requirements. It is known that addition of scandia (Sc_2O_3) to tungsten enhances the emission by more than ten-fold. Simulations of barium flow have shown that diffusivity, a measure of evaporation rate of the active material from the bulk to the surface will be lowered if the particles possess a spherical shape. Scandia-doped tungsten nanoparticles of spherical morphology were synthesized using a controlled *sol-gel* process. The powder was characterized using: Scanning Electron Microscope (SEM) in conjunction with Tunneling Electron Microscope (TEM) to study the morphology, Energy-dispersive X-ray Spectroscopy (EDS) to study the doping homogeneity, X-ray Diffraction (XRD) to study the phase purity, and Dynamic Light Spectroscopy (DLS) to study the uniformity of particle size. It was found that the powder contained nanoparticles of uniform spherical shape with homogeneous doping.

Studies were also carried out on the surface roughness to understand the influence on the emissivity and hence the emission. It was found that it is desirable to keep the roughness below 500nm for low radiation loss from the emitting

surface. The nanopowder was pressed using a specially designed die-punch having mirror-finish surface to make pellets. The pellets were sintered and integrated with individual potted heaters. These were tested in a UHV chamber containing: Auger Electron Spectroscopy (AES) for characterization of surface, and plane anode to measure the emission. The emission results are highly encouraging. Current density of up to 100A/cm^2 was achieved at 1080^{0}C$_B$ from such cathodes. The work function, as determined from the zero-field emission, is about 1.75eV. It is interesting to note that the I-V characteristics exhibited a non-saturation behavior at higher anode fields. This behavior is attributed to the formation of a substantially thick semiconducting active layer on the surface which causes field enhancement. This is further corroborated with the AES data which showed a high coverage of active material as compared to a B-type cathode.

Keywords: Sol-gel synthesis, nanoparticle cathode, dispenser cathode, Auger electron spectroscopy, THz cathode, nanoparticle characterization.

Student ID: 2009-31253

Contents

List of Figures

List of Tables

CHAPTER 1
Introduction of thermionic cathode

1.1 Introduction
1.2 Historical background
1.2.1. Evolution of dispenser cathode
1.2.2 Evolution of scandate cathode
1.2.3 Evolution of nanoparticle scandate cathode
1.3 Emission mechanism of dispenser cathode
1.4 Motivation
1.5 Goal
1.6 Organization of the thesis

1.1 Introduction

High power vacuum electron devices (VED) at millimeter wave and terahertz (THz) range find applications in medical, communication, security, and imaging. The development of such devices demands cathodes of high current density with stable and uniform emission. Therefore, the study of electron emission mechanism has become a key requirement.

Electron emission is a process in which the electrons are emitted from a solid surface into vacuum. The work function (Φ) may be defined as the minimum energy required for the electron to escape from Fermi level to vacuum. In order to remove electrons from a solid surface, energy must be applied to the solid through various processes to overcome the potential barrier and emit into vacuum. The most common processes for electron emission are thermionic emission and field emission. In these processes, energies in the form of heat or electric field are exerted to obtain electron emission. The mechanism of emission can be explained with the help of the energy band diagram of a metal-vacuum system as shown in figure 1.1

In thermionic emission electrons emit into vacuum, mainly, due to thermal energy supplied. At an absolute temperature all electrons in a metal have energy below the Fermi level (E_F). As temperature increases, some electrons gain kinetic energy higher than the Fermi level. If temperature is sufficiently high, some electrons can gain energy higher than vacuum level (E_{vac}). These electrons emit into vacuum with no applied potential. Thermionic emission from metal is normally obtained at a high temperature in the range of 1000-2000°C depending on the metal work function. The reduction of work function is of prime importance to achieve good emission. The most common electron emitters used microwave tubes are of impregnated dispenser cathodes.

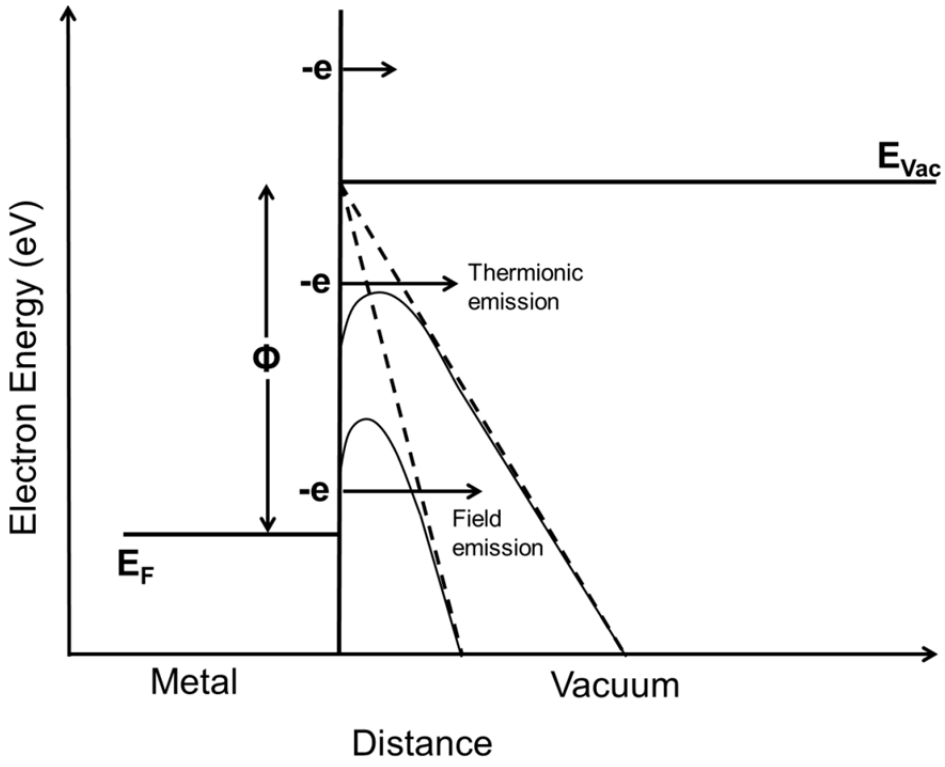

Figure 1.1: Mechanisms of thermionic and field emissions.

Impregnated cathode is made out of a porous tungsten pellet into which Barium-Calcium-Aluminates are introduced through a process called impregnation. Upon heating, a near monolayer of Ba/BaO smears the surface to reduce the work function. Improvement in emission by several folds is possible by coating a metal film/alloy-film which has a work function higher than that of base metal [1]. The improvement is also possible by an addition of materials to the impregnate as well as to the base matrix [2], [3]. Hence, the dispenser cathodes may be classified into: (a) Conventional impregnated (B-Type), (b) Metal-film-coated (M-Type /Alloy-coated) [2], (c) Scandate [4], and (d) Mixed matrix (MM-Type) [5]. Cathodes which produced good emission are W-Re-Os alloy-film, Scandate, and W-Os mixed-matrix. Typical dispenser cathodes together with the branching of developments are depicted in figure 1.2. The cathode consists of: (a) an impregnated button to produce emission, (b) a potted heater assembly to supply thermal energy, (c) outer sleeve to support the cathode, and (d) a spring to take care of mechanical and thermal stresses. A contra-wound filament is used for low inductance.

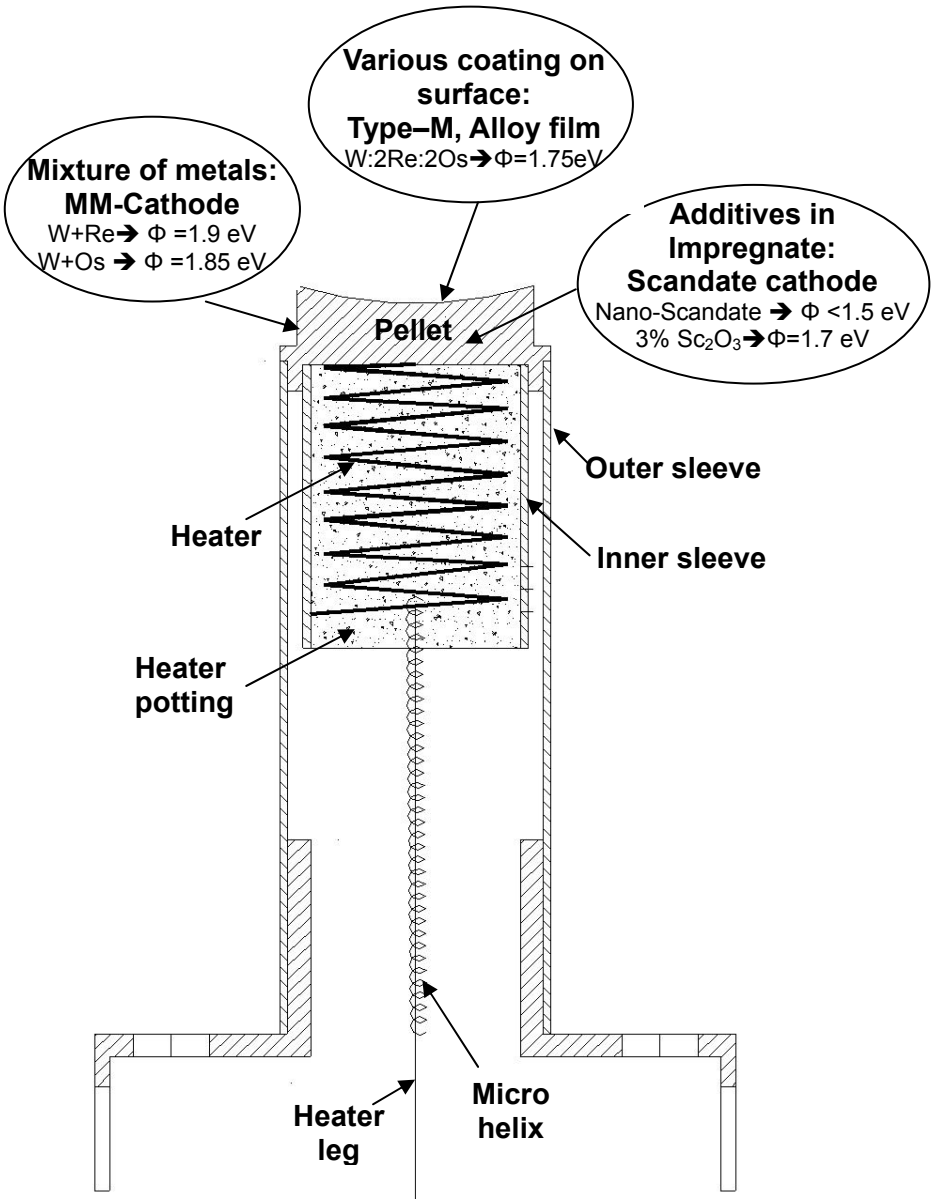

Figure 1.2: A cross-sectional view of a typical dispenser cathode. The directions in which further research developments took place in the emission enhancement are also shown.

1.2 Historical background

1.2.1 Evolution of dispenser cathode

The thermionic cathode work was started in early 1900 by simply heating pure tungsten wire. Subsequently thorium was added to enhance current density from 0.1-0.7A/cm^2.

Oxide cathode: Oxide cathode was developed by Wehnelt in 1904 [6], which produced emission density of 1A/cm^2 in CW operation. The cathode consists of a sprayed coating of alkaline earth oxides on a nickel base. Mg, Mn, Si, Al, Ti and C are added to the nickel base as impurities to reduce the interface resistance and supply free barium through a reduction process. Although the cathode possesses a low work function (about 1.5 eV), it has a limited use for the following reasons.

i. The current density that can be drawn is limited to 1A/cm^2 under CW condition due to joule heating and the consequent damage to the coating.
ii. It is poisoned in poor vacuum conditions and cannot withstand continuous ion bombardment.
iii. The coating is brittle and may easily be damage by mechanical shock.

To overcome the above limitations a new version of cathode was developed by Lemmens [7] called L-cathode at Philips Research Laboratories, Holland. It is the first commercially important dispenser cathode introduced by Lemmens et al.

The term “dispenser cathode” can be used to describe any cathode on which a thin-film of emitting material is produced at the surface and continuously replenished at the operating temperature.

L-cathode: It comprises a porous tungsten disc attached to a molybdenum sleeve. Behind the tungsten disk is a reservoir containing a solid solution of barium and strontium carbonates. Upon heating, the carbonates break down to oxides and the gas is pumped off through the pores in the tungsten. The chemical reaction between the oxides and the hot tungsten lead to the production of free barium which diffuses through the pores and reaches the surface to maintain a near monolayer surface. In spite of the good performance there are limitations with the

use of these cathodes. The cathode requires a long activation time. Also it is difficult to manufacture these types of cathode due to barium leakage which degrades vacuum condition.

To make the manufacturing techniques simpler and reduce the processing time, Hughes, Coppola and Rittner [8] modified L-cathode by pressing barium aluminate and tungsten powder which was vastly superior to the L-cathode. Hughes [9] found that further improvements could be made if the cathode was first formed from porous tungsten and then impregnated with barium aluminate. This cathode was found to be superior to the pressed cathode, because this type of cathode could be easily machined to required tolerances and with better dimensional accuracies.

Coated cathode: A coating on an impregnated cathode with a metal of higher work function than that of a base metal improves the emission. This phenomenon was first explained by Zalm and van Stratum [1] using an electrostatic model. According to this model, effective work function reduces with the higher work function of the coated metal. This model stimulated the study of metal coatings [1] and alloy coatings [5]. However, this model does not agree with certain metal coatings such as platinum, gold and copper. The study by Raju [2] suggests that it is possible to achieve a work function as small as 1.75eV by depositing an alloy of ratio 2Os:2Re:W on a B-type cathode.

1.2.2 Evolution of scandate cathode

Among the many varieties of impregnated cathode, the scandium oxide type cathodes developed by Figner et al. in 1967 [4], called as pressed scandate cathode, made an important breakthrough. Van Oostrom et al. [10] in 1977 realized 10A/cm^2 current density can be achieved at 950^{0}C operating temperature by adding Sc_2O_3. A comparable emission was achieved with the impregnated scandate cathode invented by Van Stratum et al. at Philips Research Laboratory [11] in 1979, wherein Sc_2O_3 was added to the standard impregnate. Mixed matrix scandate cathodes were first introduced by Taguchi in 1984 [12], wherein the matrix consisted of a mixture of tungsten and Sc_2O_3. Hasker et al. [13] improved this in

1990 by using W + ScH_3 as a starting powder mixture, yielding about 100A/cm^2 at the standard operating temperature. In 1986 Hasker et al. [14] also pioneered the top-layer scandate cathode by introducing a layer of 5μm thickness consisting of a mixed matrix of W+ Sc_2O_3 impregnated with Ba-Ca-Aluminate on top of a porous W body. Further variants of top-layer scandate cathodes were introduced by S. Yamamoto et al. in 1988 [15] by sputter coating the W-base with W + Sc_2O_3. In 1989, S. Yamamoto [16] published results with a combination of mixed matrix scandate cathode with lr, Os, Pt and Mo surface coating.

1.2.3 Evolution of nanoparticle scandate cathode

Recently, researchers have improved the emission density and uniformity by adopting nano technology using a *sol-gel* method [17], [18], [19]. This technique enhanced the emission capability and improved the emission uniformity [20]. In 2007, Yiman Wang et al. [21] reported nanoparticle scandate cathode using *sol-gel* technique capable of emission current density of about 100A/cm^2. The recent work by Young-Min Shin et al. [22] shows current density of up to 120A/cm^2 is achieved using the same technique. Due to nano-sized particles of Sc_2O_3, dispersed uniformly in near atomic scale in the matrix, is the key factor for high emission. A typical plot of historical development of dispenser cathode [23] is shown in figure 1.3.

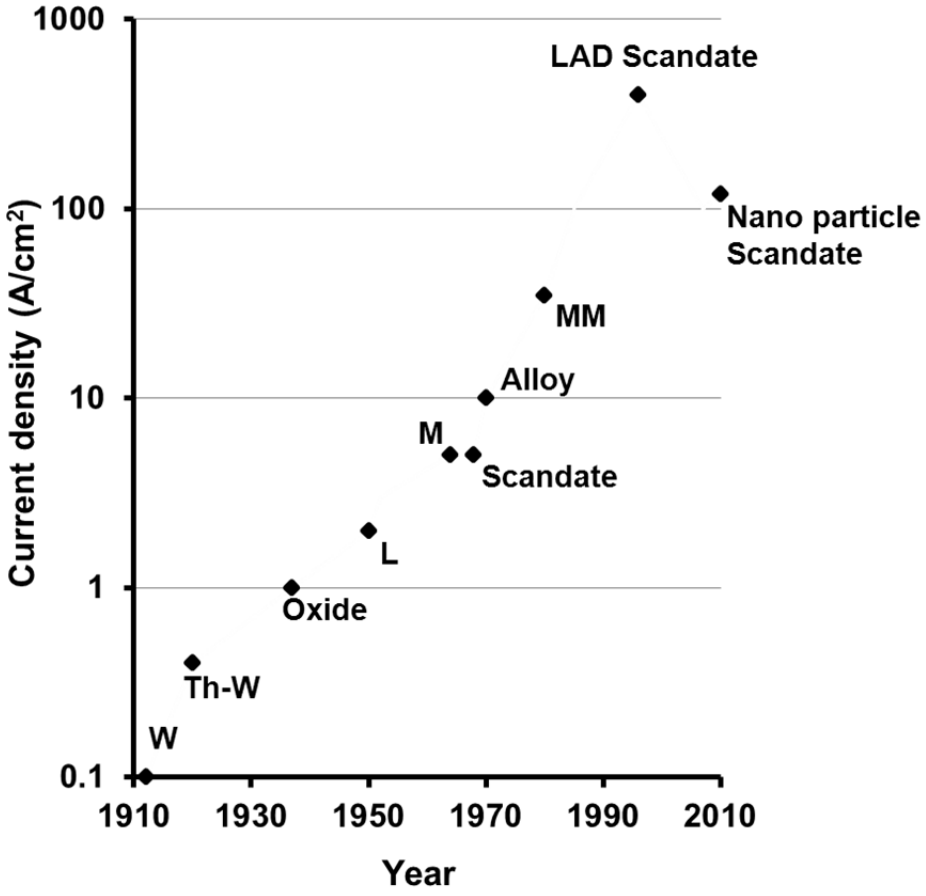

Figure1.3: Historical development of dispenser cathode.

1.3 Emission mechanism of dispenser cathode

The Porous W pellet of a conventional B-type cathode is impregnated with barium calcium aluminates at 1650^0C in a dry hydrogen atmosphere. The impregnated mixture is in the ratio of 4:1:1 and forms a eutectic at the impregnation temperature. During normal operation of the cathode, the impregnate reacts with W pore walls to generate free Ba. The Ba/BaO generation occurs through the following reactions (1.1) – (1.3) as given by Rittner et al. [24].

$$5BaO + 2Al_2O_3 \rightarrow \frac{3}{2}Ba_3Al_2O_6 + \frac{1}{2}BaAl_2O_4 \tag{1.1}$$

$$\frac{2}{3}Ba_3Al_2O_6 + \frac{1}{3}W \rightarrow \frac{1}{3}BaWO_4 + \frac{1}{2}BaAl_2O_4 + Ba \tag{1.2}$$

$$\frac{2}{3}Ba_3Al_2O_6 \rightarrow \frac{1}{2}BaAl_2O_4 + BaO \tag{1.3}$$

The transport of Ba/BaO thus generated is not well understood. Rutledge and Rittner [24] claim that the vapor transport of Ba/BaO from the bulk to the surface is through Knudsen flow from the point of generation. On reaching the surface, active materials migrate out away from pore edges by diffusion. To have a complete Ba coverage over the surface, the diffusion length should be comparable to average pore separation.

During normal operation there exists a near monolayer of barium and oxygen over the surface. The electropositive barium atoms and the electronegative oxygen atom forms positive dipole along with their image charges in the metal. The dipole field reduces the potential at the surface and hence the work function of the surface is lowered by the adsorbed atoms [6].

Figure 1.4 attempts to explain the effect of charged atomic layer on the work function of the surface. Figure 1.4(a) shows the energy level diagram of the metal

surface with no adsorbed atoms. Atoms having low ionization potential give up electron to the surface and reduce the potential at the surface as shown in figure 1.4(b). As more and more atoms get adsorbed the work function is further lowered as depicted in figure 1.4(c). This reduction in potential only occurs till a near monolayer is formed. As more atoms are brought near the surface, due to repulsion between the ions, a point is reached where probability of ionization tend to zero.

P. Zalm and van Stratum [1], using electrostatic model have explained that coating of osmium or other high work function material on tungsten substrate results in very low work function of about 1.9eV. Due to high work function of the coating material, the field at the surface increases and so large number of Ba atoms can be adsorbed. The argument does not agree with the platinum coating and the reason is attributed to the atomic structure of the metal cathode surface in relation to adsorbed oxygen and barium atoms.

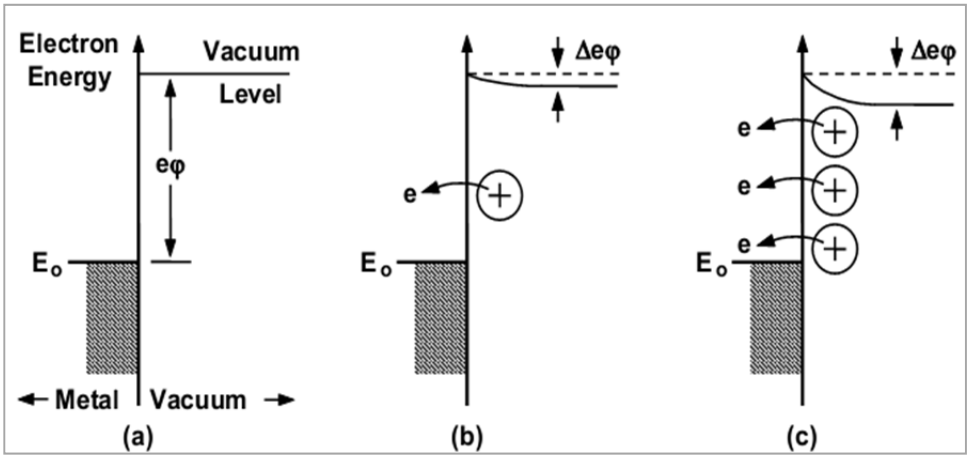

Figure 1.4: Energy level diagrams of a metal surface with: (a) no foreign ions on surface, (b) a few foreign ions on the surface, and (c) many foreign ions on the surface.

1.4 Motivation

THz waves have found applications in many different fields, such as physics, material science, engineering, chemistry and forensics. There is a new research potential area in biology and medicine; therefore, an exploration of the THz range is now-a-days a trend as well as a challenge in vacuum electron device (VED). THz spectrum region is a transition between electron device and optical device; and, the frequency range between 100 GHz to 10 THz is also known as the "THz gap" as shown in figure 1.5. This gap exists because until now there is a lack of devices which can produce THz waves. Today there are two basic methods by which THz waves are generated. The first method is by using solid-state electronics. As a general rule, the maximum achievable solid state single device power scales as the inverse square of the frequency. Therefore solid state devices are still unable to produce such a higher frequency with a significant power level [25], [26]. The second method is by optical generation such as free electron LASER, in which the device is bulky and expensive [27], [28]. Therefore, generation of high power THz wave is still a challenge to the researches. A significant progress in research in the THz region is due to the technological advancements over the last few decades [29], [30], [31]. Researchers around the world are working on a comparatively small and compact THz sources using vacuum technology [32], [33], [34]. Out of many requirements, one of the critical needs for these THz VED is of high current density electron beam > 1000A/cm^2 which can be generated from a high current density cathode capable of delivering >100A/cm^2 current density [35]. Another critical requirement is of uniform emission from the cathode surface. However, producing such a high current density and uniform emission electron source of miniature size is left as a challenge.

A conventional tungsten-Ba cathode can produce a limited current density (<<100A/cm^2) and the new field emission sources (graphene, CNT, etc) are still not reliable. The main goal of this thesis is to design, fabricate and characterize a scandia-doped tungsten dispenser cathode using nano technology that can deliver current density greater than 100A/cm^2 for use in THz VED.

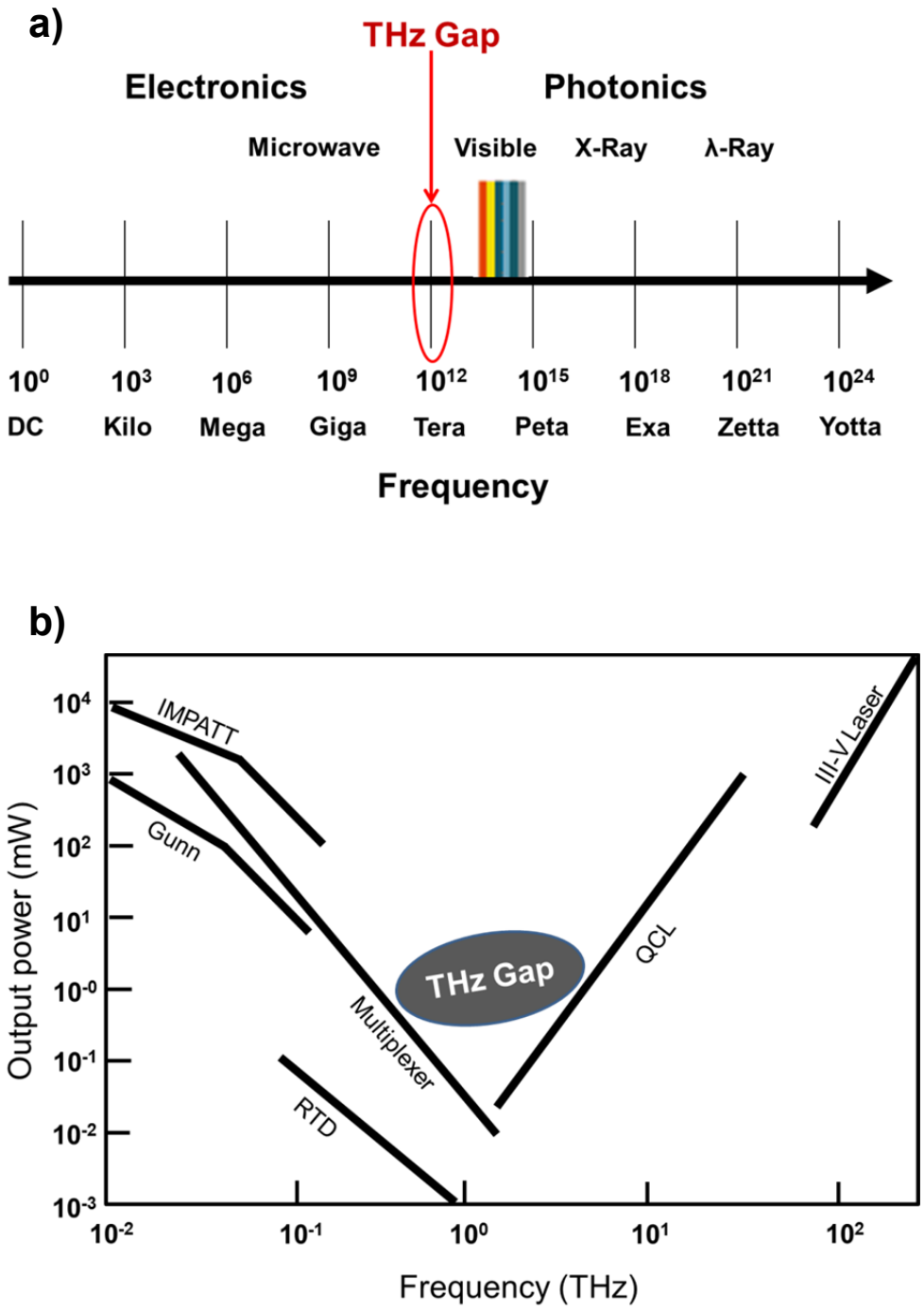

Figure 1.5: (a) EM spectrum (b) Available THz devices.

1.5 Goal

The emission properties are affected by the particle morphology, its size, and its distribution [19]-[21]. If the particles have a spherical geometry, the diffusion of doped material from the bulk to the surface is enhanced, resulting in better emission [19]. A uniform grain size distribution, which enhances the inter-pore connectivity and pore uniformity, will enhance the life of the cathode. The homogeneous mixing of the doping material also enhances the emission uniformity of the cathode. The synthesis of the spherical shape, a uniform grain size distribution, homogeneous mixing and a pure phase of scandia-doped tungsten nanoparticles are the critical requirements for the development of high-current-density cathodes for use in THz devices. The goal in this work is to develop a dispenser cathode capable of delivering current density more than 100A/cm^2 by using scandia-doped tungsten nanoparticles of spherical shape and uniform dispersion.

1.6 Organization of the thesis

There are five chapters in this thesis which are organized as following:

- Chapter I is devoted to the introduction to the thermionic emission. In this chapter an extensive survey of historical development of thermionic cathodes is also made. Finally, motivation and the goal of the research are mentioned.
- Chapter II contains various nanoparticle syntheses process. Different issues and choice of suitable synthesis process is mentioned from the application point of view. This chapter also provides an insight into the process of nanoparticle synthesis using *sol-gel* technique. The results on the characterization of synthesized nanoparticles are also given.
- Chapter III gives the theoretical design aspect of cathode.
- Chapter IV describes the experimental work on the device fabrication towards achieving the objectives. The results on the characterization of fabricated device are also presented.
- Chapter V concludes the results of proposed research and aspects of future work.

CHAPTER 2

Novel synthesis method and experimental characterization of nanoparticle for THz cathodes

2.1 Previous synthesis methods

2.2 Requirements of nanoparticle physical parameters for THz cathode

2.3 Choice of synthesis process of scandia-doped tungsten nanoparticle

2.4 Experimental synthesis of nanoparticle

2.5 Experimental characterizations of nanoparticle

2.5.1 Characterization of morphology

2.5.2 Characterization of doping homogeneity

2.5.3 Characterization of particle size distribution

2.5.4 Characterization of particle phase orientation

2.1 Previous synthesis methods

There are many different approaches of producing nanoparticles. The synthesis process can be classified into top-down and bottom-up approaches. In top-down approaches, the source material is reduced from bulk size to nano-scale e.g., grinding, thermal decomposition which operates on the solid phase. Bottom-up processes can be further subcategorized into vapor phase (e.g, pyrolysis, inert gas condensation) and liquid phase (e.g., solvothermal, *sol-gel*) synthesis process. A general classification of nanoparticle synthesis is given in figure 2.1.

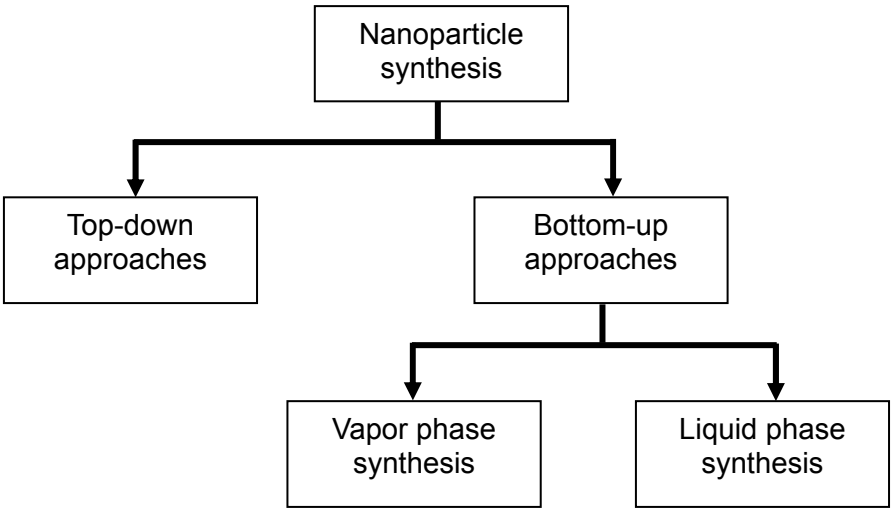

Figure 2.1: General classification of nanoparticle synthesis approach.

Synthesis of nanostructured tungsten powder has been widely studied in recent years due to its potential application in critical areas. As a refractory metal with excellent mechanical properties and good thermal and electrical conductivity, tungsten has been in use for decades in high temperature applications e.g., rocket nozzles, filaments, tungsten based carbide, disulfide and various alloys, etc. Several processes have been developed over the years for the production of nanostructured tungsten. Among them some processes are widely used such as plasma synthesis [36]-[37], high energy ball milling [38], combustion method [39]-[40], electric wire explosion [41]-[42], chemical vapor synthesis in thermal plasma reactor [43], thermal decomposition [44] etc. High-temperature reduction process usually fails

to produce control shape nano-sized tungsten particles. Low-temperature synthesis methods, such as sono-electrochemistry method [45], Solvothermal decomposition [46], spray drying [47], *sol-gel* process [17]-[21] are easy to control particle parameters.

2.2 Requirements of nanoparticle physical parameters for THz cathode

It has been established that: (a) the emission uniformity of cathodes increases due to the homogeneous doping of scandium oxide with W nanoparticles [21]; (b) the uniform size distribution of these nanoparticles enhances the porosity and inter-pore connectivity of the pellets, which in turn improves the cathode life due to better diffusivity of doped material [18]; and (c) the emission current density increases if spherical particles are used [20]. Therefore, the synthesis of a spherical shape, a uniform distribution, homogeneous doping, and uniform-phase nanoparticles are the critical requirements related to the development of high-current-density cathodes for THz VED. The main aim in this section is to develop an easy, reproducible synthesis process addressing these issues in the development of scandia-doped tungsten nanoparticles for cathode applications.

2.3 Choice of synthesis process of scandia-doped tungsten nanoparticle

A considerable amount of research is going on to synthesize mono-disperse metallic nanoparticles with controlled sizes and morphologies [36]-[47]. Different approaches, including chemical, physical and biological methods, have been adopted for this purpose. However, there is no general strategy to create homogeneous composite tungsten nanoparticles with a narrow size distribution, spherical of morphology. Physical methods such as wire electrical exploration [41], [42], spray drying [47], microwave plasma synthesis [36], [37] and thermal decomposition [43], [44] are not suitable for doping of other materials. Chemical methods, such as Sono-electrochemistry method produces phase impure particles which are not suitable for cathode application [45]. Combustion synthesis produces

wide particle size distribution which will affect the pore uniformity and inter pore connectivity [39], [40]. In Reverse Microemulsion-Mediated Method [48], the particle size and uniformity are very sensitive to process parameters. Solvothermal decomposition [46] produced arbitrary shape of the particle which reduced the diffusion of the doping particles. This technique is not suitable for cathode application. Self-propagating high-temperature synthesis (SHS) [49] produce a wide range of particle sizes. Recently Jinshu Wang et al. [19] adopted a *sol-gel* process, followed by a high temperature reduction in hydrogen environment. Initially they prepared Sc_2O_3-doped tungsten oxide powder using a *sol-gel* process. Then the doped tungsten oxide powder was reduced into a metallic tungsten powder in two steps by dry hydrogen at a high temperature. However, in this process the particle size depends on the amount of scandium. However, this process appears to be rather cumbersome, motivates to suggest here a simple method of synthesizing scandia-doped tungsten nanoparticles using *sol-gel* process. In this work, scandia-doped tungsten nanopowders have been prepared by dissolving tungsten oxide at 300^0C in to the optimum mixture of nitric acid, citric acid and ammonia. It was found that the particle size can be easily controlled and morphology of the particle is spherical since it dissolved into solvent. At the same time scandium mixed homogeneously with tungsten nanoparticle which is responsible for the emission uniformity

2.4 Experimental synthesis of nanoparticle

A schematic flow diagram of the scandia-doped tungsten nanoparticle preparation is shown in figure 2.2. Tungsten oxide powder of 99.9% purity with an average particle size of about 80μm was used as the starting material. Scandia (Sc_2O_3)-doped tungsten powder was prepared using a *sol-gel* process by dissolving tungsten oxide in a mixture of nitric acid, citric acid and ammonia at 300^0C. An initial 3% aqueous solution of scandium nitrate ($Sc(NO_3)_3$) and an 8% aqueous solution of citric acid were added to 50ml of nitric acid. Then, 2 gram of tungsten oxide was added to the solution, which was stirred continuously for 2 minutes. Ammonia solution was added slowly to maintain a required pH of the solution by monitoring with a pH meter. Stirring of the solution continued under hot condition by maintaining the temperature at 300^0C for 1 hour to form a hydrolysis reaction. The solution was dried at 400^0C for 30 minutes under continuous stirring. During this process, the sol (solution) becomes a gel. After the formation of the gel, it was allowed to further dry at the same temperature for a few hours to remove residual organics and water molecules. After that, the powder was collected and ground in agate mortar. The powder was then calcined at 500^0C for 16 hours, after which it became a yellow tungsten trioxide nanopowder. Finally, scandia-doped tungsten nanopowder was produced by reducing the oxides under a dry hydrogen atmosphere at 700^0C for 1 hour in a furnace. The nano-Sc_2O_3-doped tungsten powder was characterized using several techniques mentioned in section 3.2.

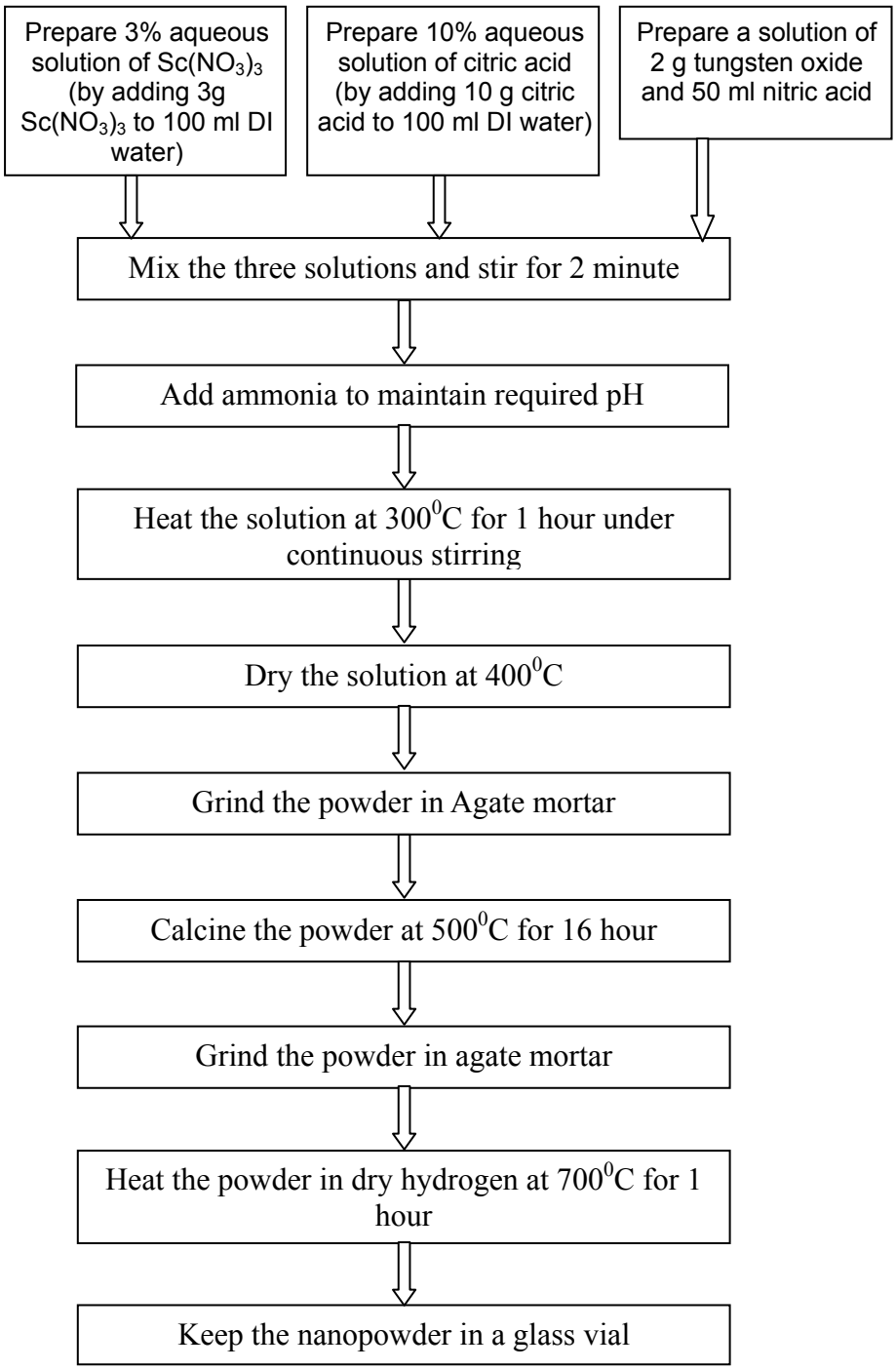

Figure 2.2: Flow diagram of the synthesis processes to prepare Sc_2O_3-doped tungsten nanoparticles using sol-gel method.

2.5 Experimental characterizations of nanoparticle

Several characterization tools were used to determine the particle size, phase orientation and the morphology of the nanoparticles. The particle size and phase of the powder were examined at room temperature by High-Resolution X-ray Diffraction (XRD) using Cu-Kα radiation. The analysis was carried out over the 2θ range of 10^0 to 90^0. The morphology and microstructure of the powder were examined using a Ultra-High-Resolution Thermal FE-SEM and a High-Resolution TEM (HRTEM). The FE-SEM equipped with an EDS apparatus used in this study was the ‘‘HITACHI S-4300’’. The TEM study of powder was carried out using the ‘‘JEM-3010 TEM’’. The samples for the analysis were prepared by dispersing nanoparticles in methanol and DI water at a ratio of 1:1. This was ultrasonically treated for 15 minutes and drop-casted onto a carbon-coated copper grid, which was followed by drying in air at room temperature.

2.5.1 Characterization of morphology

The microstructures of scandia-doped tungsten nanoparticles were examined by scanning electron microscopy (SEM) and transmission electron microscopy (TEM) observations. The schematic diagram of SEM and TEM are shown in figure 2.3 and 2.4 respectively.

Figure 2.5 shows the SEM image of nanoparticle. As the particles were agglomerated, it was somewhat difficult to observe the particle morphology and size. Therefore, high-resolution TEM was used for the purpose of imaging the nanoparticles after dispersing them by ultrasonic agitation. A spherical morphology with an average particle size of 100nm is found from the TEM images as shown in figure 2.6. In order to study the doping homogeneity, an energy dispersive analysis of X-rays (EDS) was carried out (figure 2.8(a)–(d)).

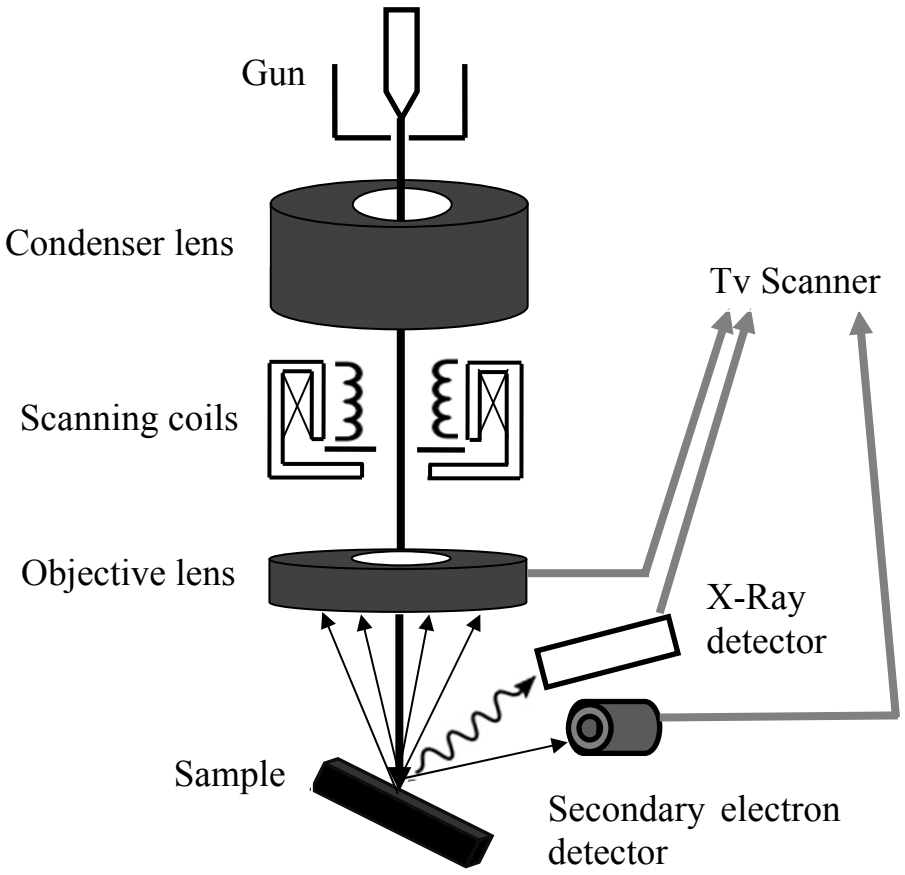

Figure 2.3: Schematic diagram of Scanning Electron Microscope.

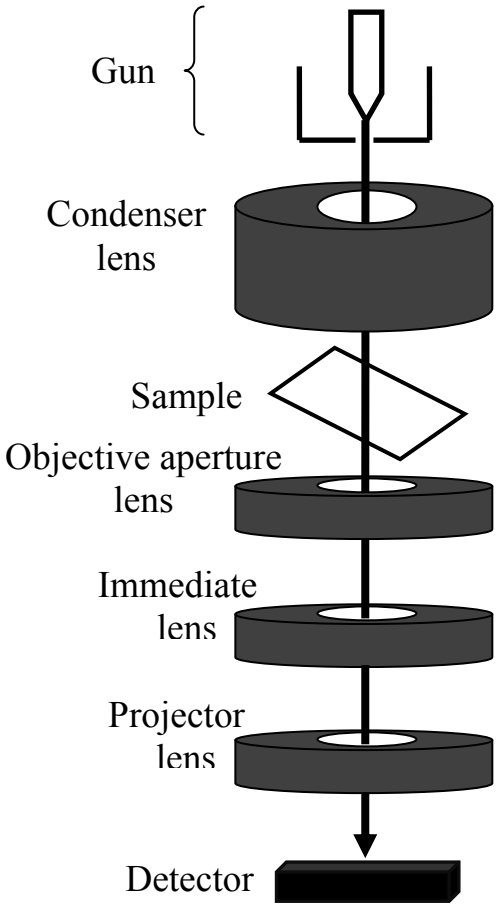

Figure 2.4: Schematic diagram of Tunneling Electron Microscope.

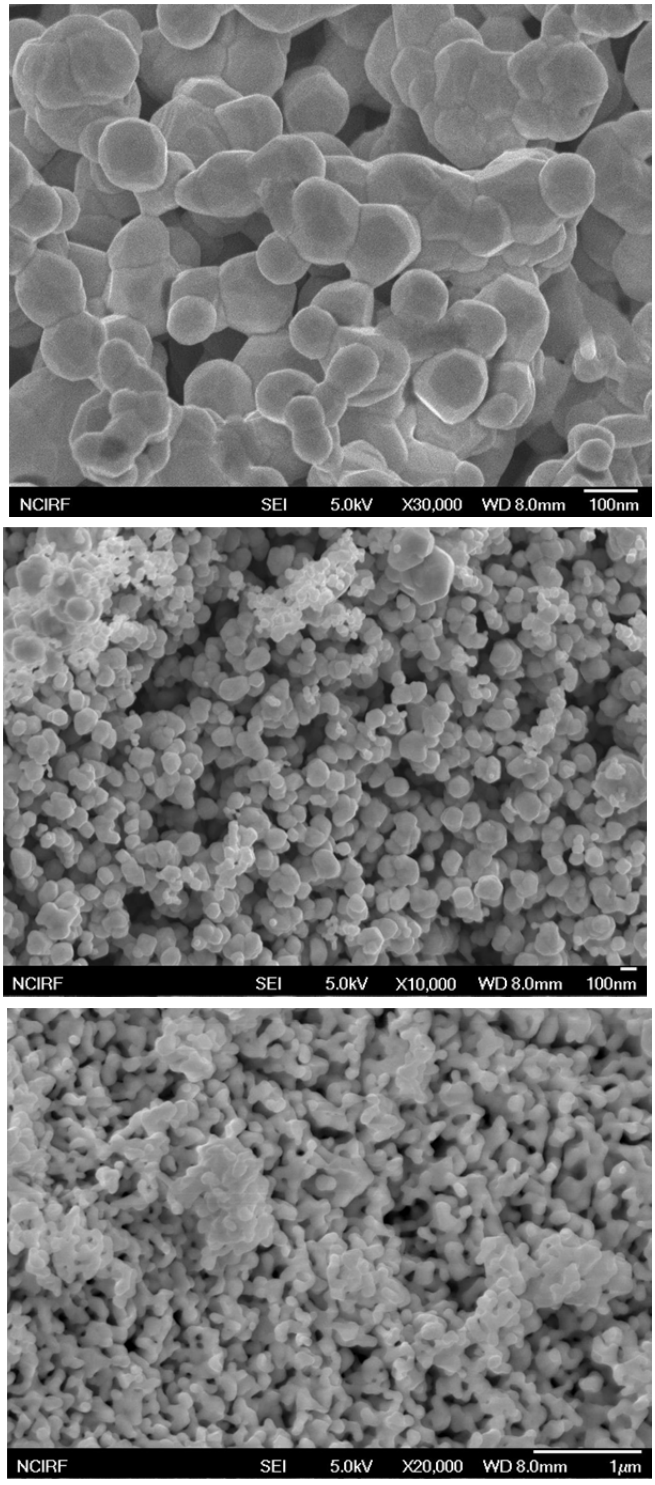

Figure 2.5: Morphology of tungsten nanoparticles obtained from SEM

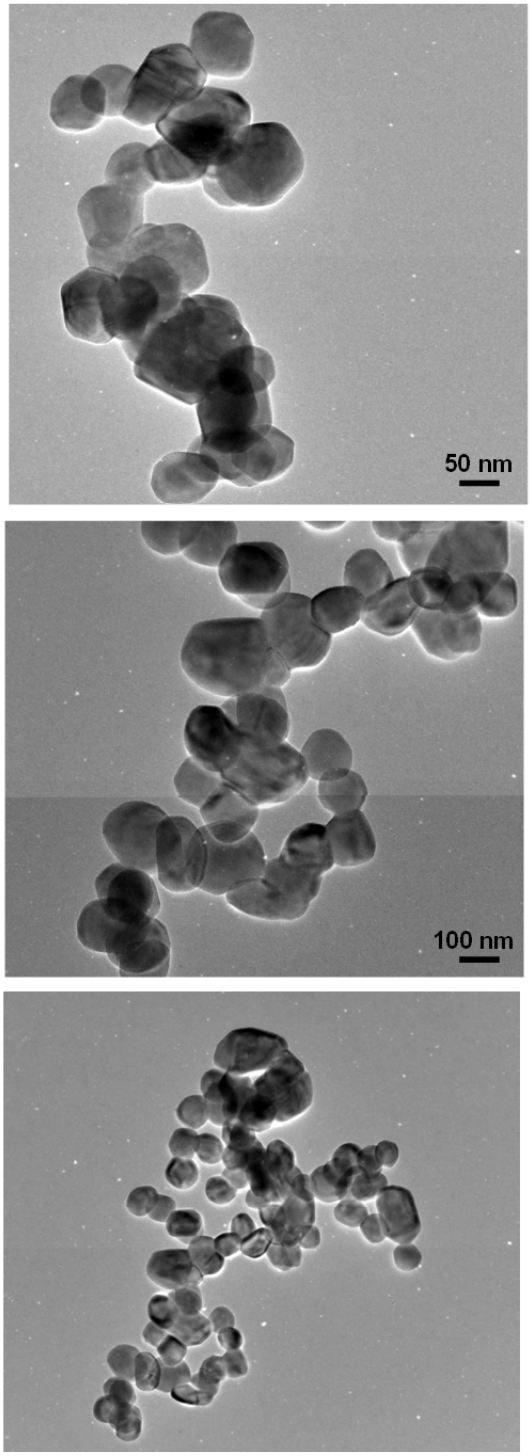

Figure 2.6: Morphology of tungsten nanoparticles obtained from TEM

2.5.2 Characterization of doping homogeneity

An EDS spectroscope attached to the FE-SEM device was used to analyze the doped nanoparticles in spots with a diameter of 50nm. Figure 2.8(a)–(d) depicts the EDS spectrum of a nanoparticle taken from four different sample positions (figure 2.7). Only tungsten, scandium and oxygen were found to be present, while no other elements were detected using EDS. Practically, oxygen and carbon elements were also detected by the EDS analysis, where the carbon elements originate from the sample holder. The trace of the element oxygen confirms that scandium becomes scandium oxide during the synthesis process. Table 2.1 represents the percentage in terms of the weights and atomic concentrations of the tungsten, scandium and oxygen elements as evaluated from the EDS measurements. From figure 2.8 and Table 2.1, it can be concluded that the scandium is uniformly doped with tungsten particles.

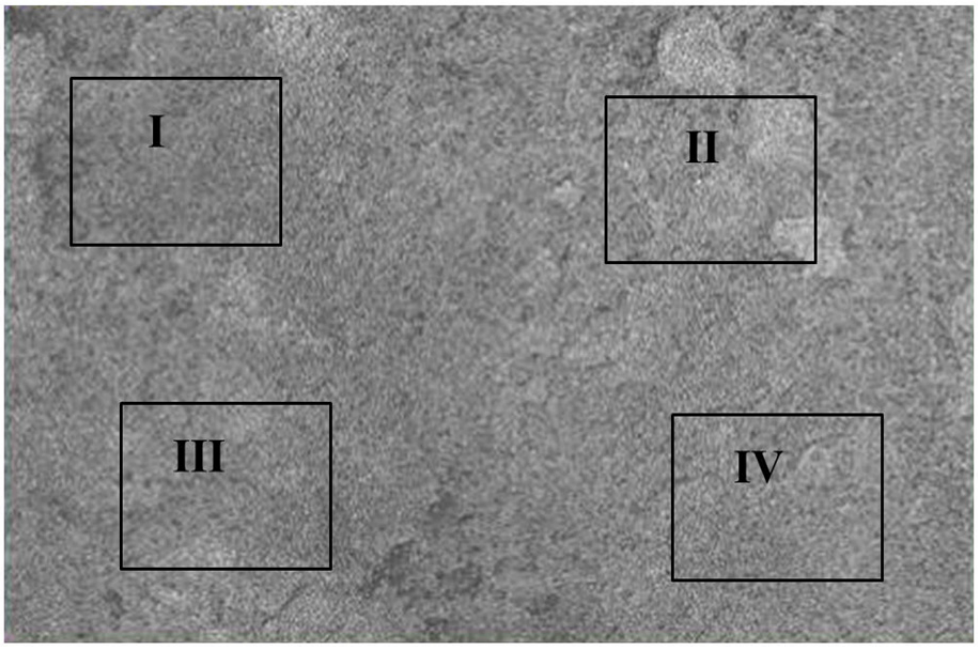

Figure 2.7: SEM image taken during the EDS analysis, indicating four locations (I, II, III and IV) on the image from where EDS spectra was taken.

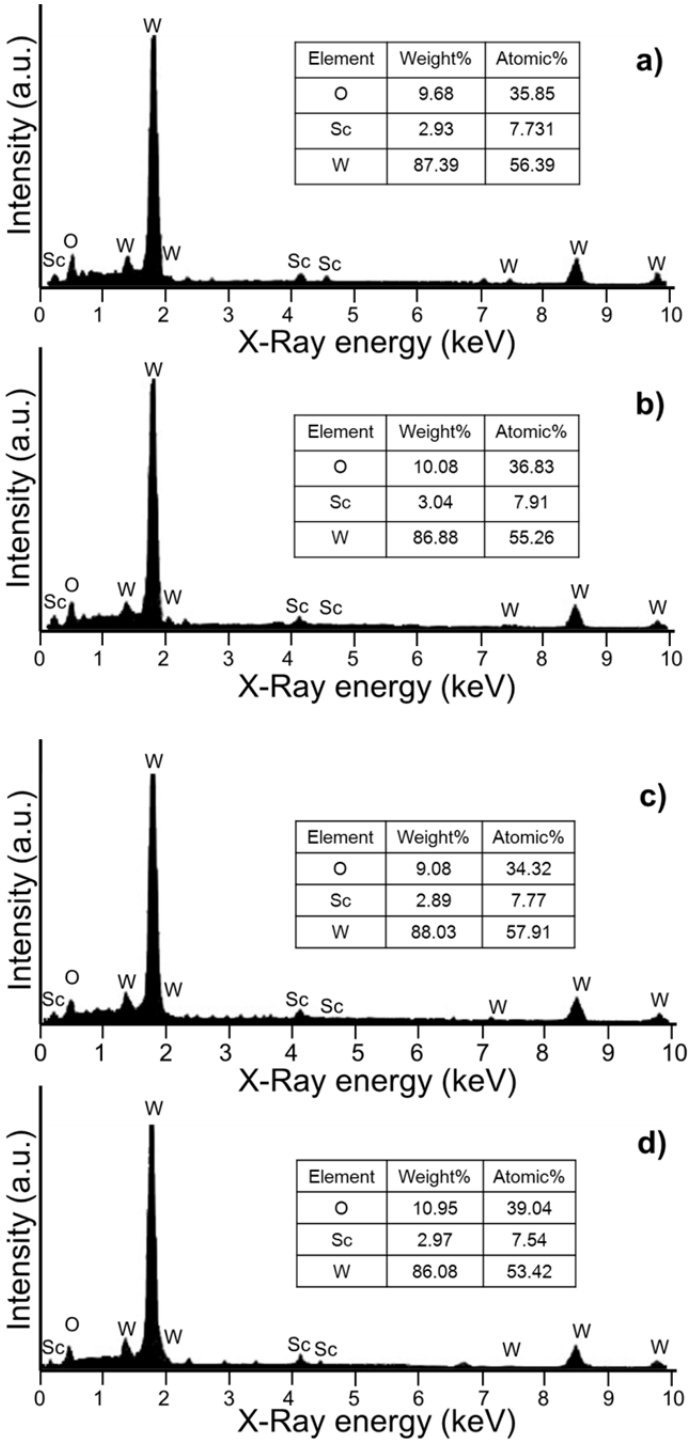

Figure 2.8: EDS spectra taken at (a) location I, (b) location II, (c) location III and (d) location IV.

Table 2.1: EDS Analysis of Sc-doped tungsten nanoparticles

Figure		Element		
		Tungsten	Scandium	Oxygen
a	Weight %	87.39	2.93	9.68
	Atomic %	56.39	7.731	35.85
b	Weight %	86.88	3.04	10.08
	Atomic %	55.26	7.91	36.83
c	Weight %	88.03	2.89	9.08
	Atomic %	57.91	7.77	34.32
d	Weight %	86.08	2.97	10.95
	Atomic %	53.42	7.54	39.04

2.5.3 Characterization of particle size distribution

The particle size distribution in the powder was determined using the dynamic light spectroscopy (DLS). A schematic diagram of DLS is shown in figure 2.9. Using the particle count data from figure 2.10, the average particle diameter, standard deviation and relative standard deviation are calculated with the help of the following equations (2.1) – (2.3):

$$D_g = \frac{\sum_{i=1}^{n} N_i D_{Pi}}{N} \tag{2.1}$$

$$S = \left(\frac{\sum_{i=1}^{n} N_i (D_{Pi} - D_g)}{N} \right)^{1/2} \tag{2.2}$$

$$\delta_{\text{rel}} = \frac{S}{D_g} \times 100 \tag{2.3}$$

where D_g is the average diameter, S is the standard deviation, D_{pi} is the diameter midpoint for the size channel i, N_i is the concentration within the channel i, N is the total number of counted particles, n is the number of channels, and δ_{rel} denotes the relative standard deviation.

The powder was prepared at different reduction temperatures of 1000, 900, 800 and 700°C, respectively. The corresponding measured average grain sizes were 119, 97, 71 and 46nm, with relative standard deviations of 17.2, 16.5, 13.5 and 12.7%, respectively. This finding shows that the relative standard deviation decreases with a decrease in the temperature at which the reduction is carried out. The phenomenon of a higher standard deviation at a higher temperature can be attributed to the diffusion of particles and/or inter-particle coagulation.

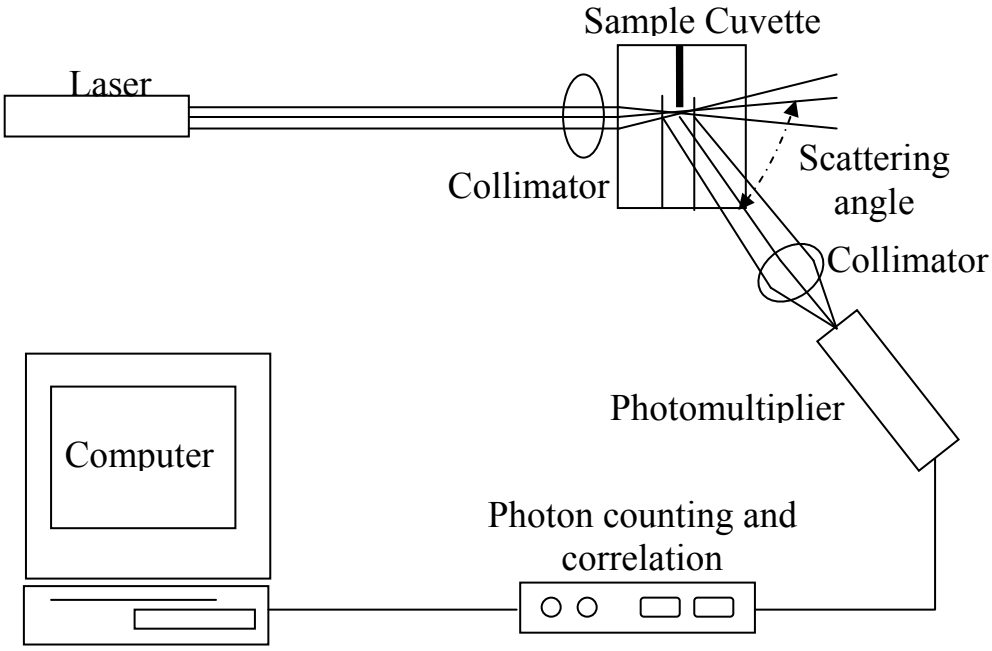

Figure 2.9: Schematic diagram of Dynamic Light Spectroscopy.

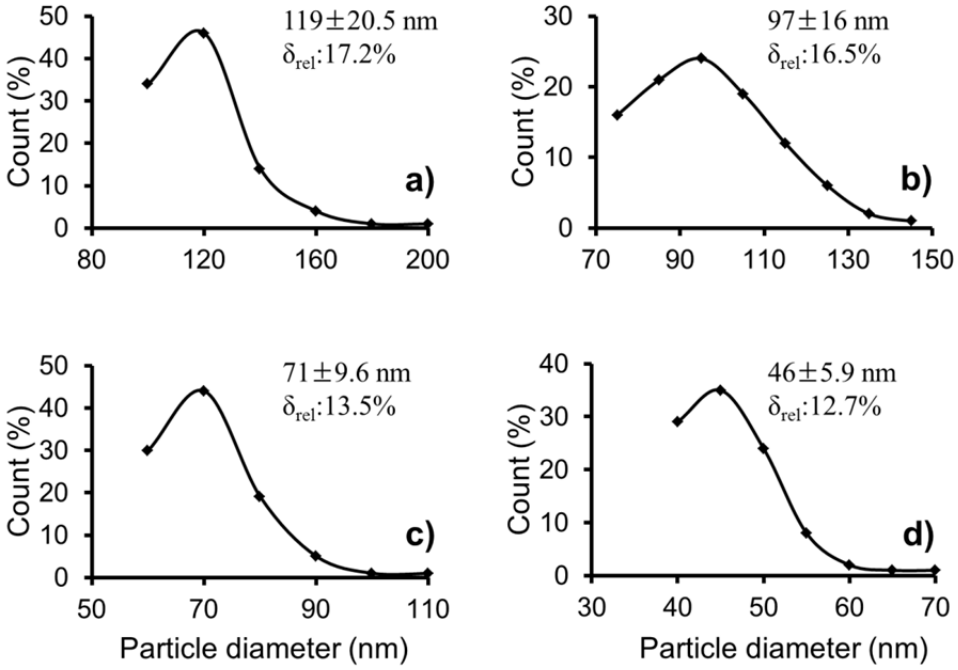

Figure 2.10: DLS spectra of the particle distributions of various tungsten nanoparticles after a reduction in hydrogen prepared under different temperatures: (a) 1000°C, (b) 900°C, (c) 800°C and (d) 700°C.

2.5.4 Characterization of particle phase orientation

The phase characterization assessment was carried out using a powder XRD Bruker D8 DISCOVER (Germany) device. A schematic diagram of XRD is shown in figure 2.11. The diffraction patterns were recorded from 30°-90° at a scan rate of 0.02° per step and at 5 second per point. Figure 2.12(a)–(d) shows typical XRD patterns of the nanoparticles. The absence of an extra peak claims the purity of the nanoparticles. The crystalline size of the sample was obtained from Scherer's formula [50]

$$D = k\lambda /(\beta \cos\theta) \qquad (2.4)$$

Where, D is the average grain size, k the shape factor (0.89), λ the X-ray wavelength (1.5418Å), β the full width at half maxima (FWHM) and θ the diffraction angle. The average crystalline size approximately 41, 65, 89, and 108nm were calculated using (2.4) for four different citric acid concentrations of 4, 6, 8, and 10% respectively.

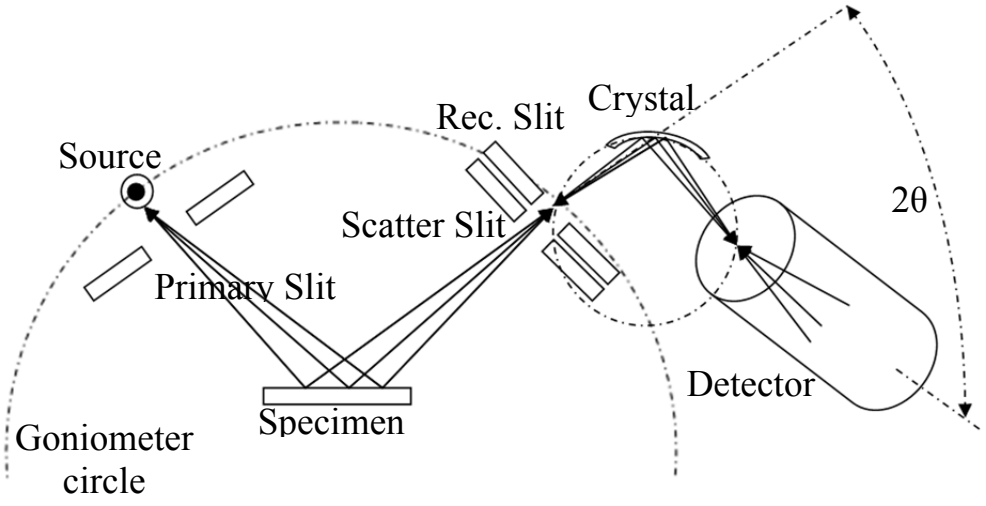

Figure 2.11: Schematic diagram of Scanning X-ray diffractometer.

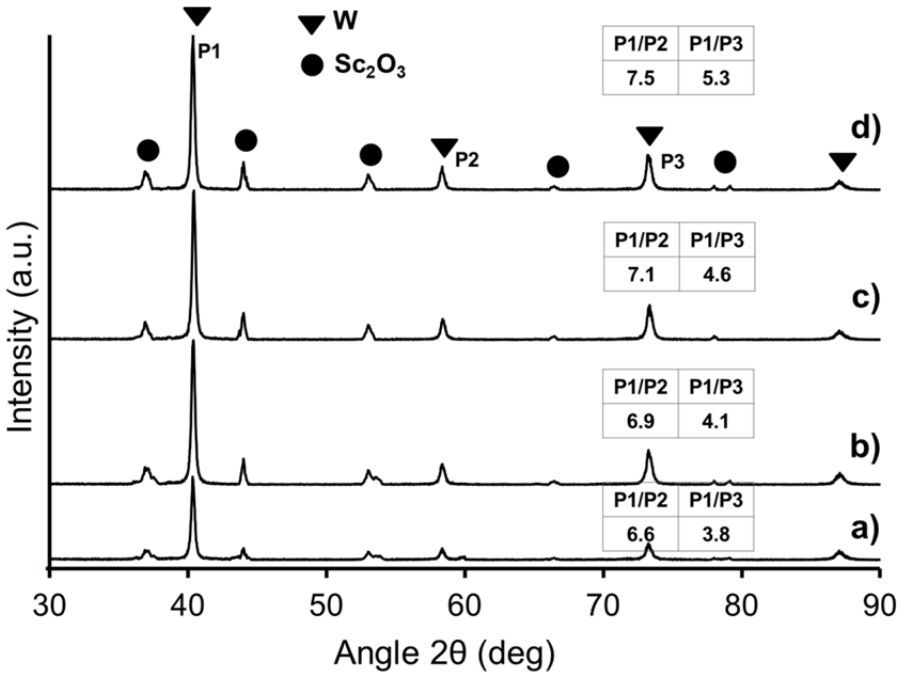

Figure 2.12: X-ray patterns of tungsten nanoparticles at different citric acid concentrations, viz. (a) 4%, (b) 6%, (c) 8%, and (d) 10%. The resulting particle sizes are 108 nm, 89 nm, 65 nm, and 41 nm respectively.

Table 2.2: Tungsten peak ratios of the XRD spectrum corresponding to different citric acid concentrations

Sample	Citric Acid (%)	1st Peak/ 2nd Peak	1st Peak/ 3rd Peak
a	10	7.5	5.3
b	8	7.1	4.6
c	6	6.9	4.1
d	4	6.6	3.8

Table 2.2 shows that as the citric acid concentration increases the tungsten peak-to-peak ratio of XRD spectrum also increases, which indicates the formation of a pure-phase oriented material. The concentration of the citric acid in the aqueous solution can affect the hydrolysis reactions, leading to the formation of many types of complexes. In addition, the phase purity and particle size are influenced by the acid concentration during the gelling and calcination processes. Therefore, the particle size and phase orientation can be controlled by means of the citric acid concentration.

CHAPTER 3

Design and experimental characterization of nanoparticle-based pellet for the cathode fabrication

3.1 Design of Pellet

3.1.1 Optimization of pore parameters

3.1.2 Estimation of required porosity

3.1.3 Influence on the geometry of nanoparticles

3.1.4 Estimation of equilibrium Ba/BaO pressure (P_0) inside the pore of matrix

3.2 Experimental characterization of porosity and pore uniformity

3.3 Optimization of cathode surface roughness

3.4 Thermal design and experimental validation of cathode assembly

3.1 Design of pellet

The work function of a dispenser cathode reduces due to the formation of a dipole monolayer of barium with tungsten. Barium transfers its two outer most electrons to tungsten form a dipole. Oxygen competes with tungsten in sharing the electrons. The studies by Gibson and Thomas [51] using electron energy loss spectroscopy (EELS), indicate that barium and oxygen are “near” coplanar.

Upon heating, barium is transported from the bulk to the surface through the pores, through diffusion and Knudsen flow, to form a Ba/BaO monolayer [52]. Therefore, the parameters associated with the pore, viz. pore size, porosity, inter-pore connectivity, and pore distribution play a critical role in the emission uniformity and life. In this section, the following are discussed:

(a) The requirement of particle physical parameters in order to obtain required pore characteristics for optimum transportation of barium from the bulk to the surface.
(b) Design of pressing tools to form pellet.
(c) Thermal design of cathode structure.

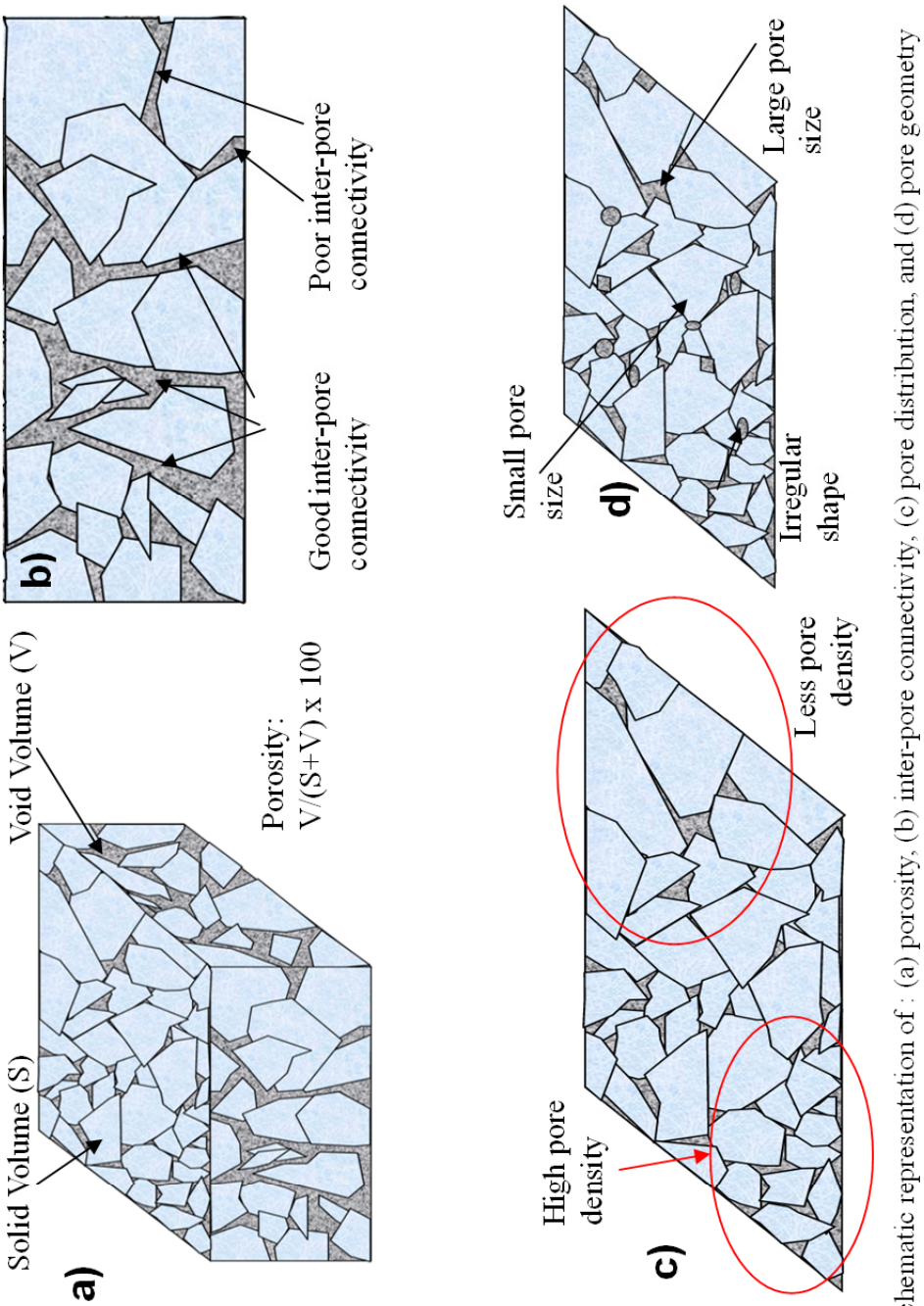

Figure 3.1: Schematic representation of : (a) porosity, (b) inter-pore connectivity, (c) pore distribution, and (d) pore geometry

3.1.1 Optimization of pore parameters

The optimizations of the following parameters have a critical importance on the emission of dispenser cathode. These parameters are graphically explained in figure 3.1.

(a) Porosity: The porosity is the volumetric void space in the pellet which may be defined as [void volume /total volume]x100. The porosity has a bearing on the life of cathode. Cathodes possessing low porosity will have low evaporation rate at the expense of barium coverage and hence low emission. In the case of high porosity, the coverage and evaporation increases, resulting in high emission at the expense of poor life.

(b) Inter-pore connectivity: The second parameter of importance is the pore connectivity. If the pellet has a poor inter-pore connectivity, the supply of Ba/BaO from the bulk to the surface is affected resulting in poor emission and short life.

(c) Pore distribution: The pores in the cathode button are distributed in random sizes and shapes across the surface, as shown in figure 3.1(c), resulting in non-uniform barium coverage which leads to large variation in work function over the surface. The emission from such an emitting surface would introduce noise at the output. Emission uniformity has been an important issue with dispenser cathodes [2]. Figure 3.2 illustrates the importance of using a uniform emission cathode. The simulated I-V characteristics of two different cathodes having work function distributions narrower and wider, respectively, are shown in the figure 3.2. The cathode of wider work function has a higher emission at higher anode voltages; however, the available emission at design voltage is low. This cathode is of no use when operated at low temperatures. Therefore, a direct control on pore distribution is an obvious solution. Uniform barium coverage can be achieved through uniform pore arrangement, rendering a uniform work function distribution across the cathode surface.

(d) Pore geometry: The two parameters of importance are pore size and the pore shape. For small pore size (densely distributed across the surface), the coverage is expected to be more uniform and the evaporation rate is expected to be low. If the pore size is too small (<2 micron average diameter), the barium supply from the bulk is restricted due to narrow paths. For large size pores (lower pore density), the inter-pore spacing is larger and the coverage is not expected to be lower at the middle of inter-pore region. Typical average pore size in dispenser cathodes is about 5 micron.

In addition to pore size, the shape also plays a role in the coverage of active material. Irregular shapes are undesirable. The desired shape is of circular geometry for a better transport of active material from the bulk to the surface.

The non-uniform pore size, shape and its distribution across the surface leads to non-uniform Ba coverage resulting in a “patchy surface”. A surface exhibiting wide work function distribution is said to be “patchy”.

W. C. Rutledge [53] carried out a measurement of cathode emission *vs*. barium arrival rate (figure 3.3). It was found that the barium arrival rate increases emission from zero to maximum value and then saturated. At very low barium arrival rate, the emission is low. On the other hand at very high barium arrival rate, the barium evaporation will be high which will reduce cathode life. This observation supports the need of porosity optimization for long life, high current density cathode application.

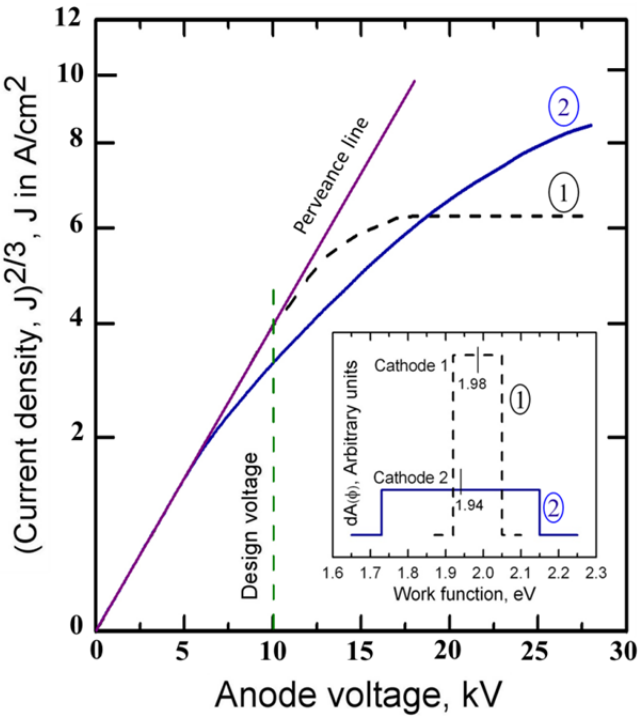

Figure 3.2: Comparison of the I-V characteristics of a diode with cathode of different work function distribution at the same operating temperature.

(Note that at the design voltage the cathode with the lower saturated emission will be satisfactory while the other will not even though the total current it gives at high voltage is larger) [2].

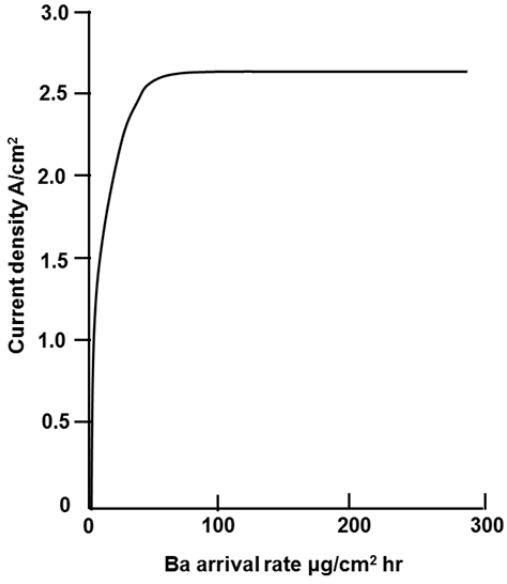

Figure 3.3: Cathode emission versus barium arrival rate. [53]

3.1.2 Estimation of required porosity

There are two possible ways of transporting barium through the porous tungsten pellet. One is migration of barium through internal pore surfaces, and the other by the vapor flow through the pores [53], [54]. To determine the dominant transport mechanism, measurements have been carried out by flowing of an inert gas through tungsten plugs of varying porosities [54]. From these data and the estimated barium pressure in the cavity, it is possible to compute the Knudsen flow component and to compare it with the cathode evaporation rate [54].

Consider a porous plug of cross-sectional area A with one side maintained at negligible pressure and the other connected to an isolated volume V containing a gas of molecular weight M at a pressure P and temperature T in kelvin. The mass rate of Knudsen flow through the plug is given by

$$\frac{dm}{dt} = -\frac{\alpha A P \sqrt{M}}{N_A \sqrt{2\pi m_0 kT}} \tag{3.1}$$

where α is the transmission coefficient (ratio of number of particles emerging/sec from top of plug to that impinging/sec on bottom), N_A is Avogadro's number, m_0 is the mass associated with unit atomic weight, and k is Boltzmann's constant. Barium pressure declines with time as the gas is pumped from the reservoir through the plug. At the low pressures in question the gas will obey the perfect gas law, which together with (3.1) leads to

$$P = P_0 e^{-\lambda t} \tag{3.2}$$

Where,

$$\lambda = \frac{\alpha A \sqrt{kT}}{V \sqrt{2\pi m_0 M}} \tag{3.3}$$

And P_0 represents the initial pressure. Thus, measurement of the decay constant λ determines the transmission coefficient α. Equation (3.1) may then be evaluated for the steady state Knudsen flow rate of barium by employing for P the estimated

pressure (3.2), for *M* the atomic weight of barium, and for T the cathode operating temperature.

Finally it can be written as,

$$\frac{dm}{dt} = -\frac{\alpha A P_0 e^{-\lambda t}\sqrt{M}}{N_A\sqrt{2\pi m_0 kT}} \tag{3.4}$$

The value of λ for a porous tungsten plug assembly was experimentally determined by Rutledge and Rittner [53]. One side of the tungsten plug was connected with a high pressure barium vapor chamber and the other side was welded with a chamber with negligible pressure and monitor by a Pirani gauge.

The observed barium evaporation rate with porosity is shown in figure 3.4(a) and transmission coefficient with porosity is shown in figure 3.4(b). The result depicts that transmission coefficient is a critical parameter of porosity.

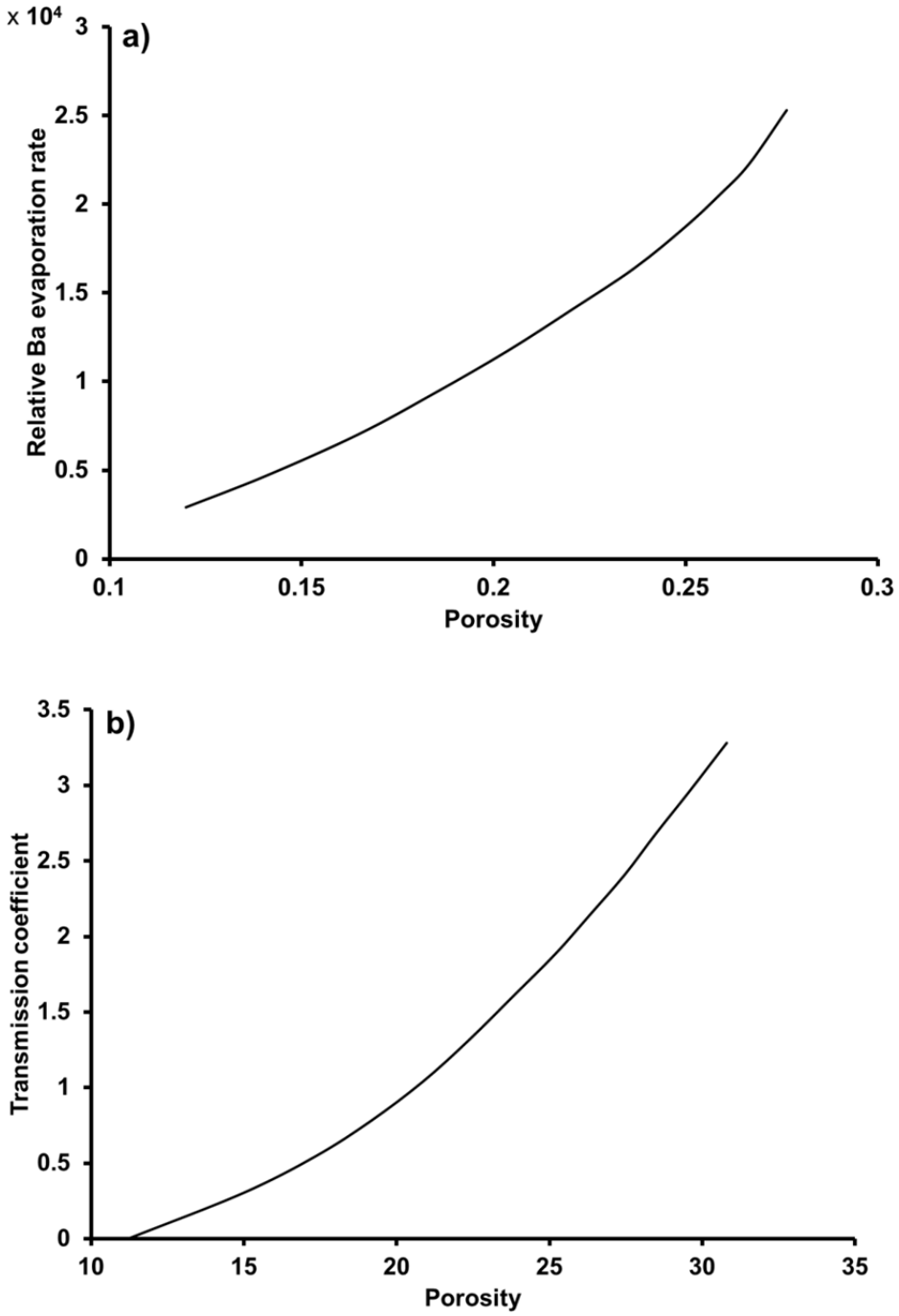

Figure 3.4: (a) Barium evaporation rate and (b) transmission coefficient with porosity [53]

By solving equation (3.4), one can get,

$$m = -\frac{\alpha A P_0 \sqrt{M}}{N_A \sqrt{2\pi m_0 kT}} \int e^{-\lambda t} dt \tag{3.5}$$

$$m = \frac{VMP_0}{N_A kT} e^{-\lambda t} + \mathrm{C} \tag{3.6}$$

$at, t = 0, m = m_t$

$$C = m_t - \frac{VMP_0}{N_A kT} \tag{3.7}$$

Where, m_t is the initial mass.

Therefore,

$$m = m_t - \frac{VMP_0}{N_A kT}\left(1 - e^{-\lambda t}\right) \tag{3.8}$$

Figure 3.5 shows that, barium transmission coefficient increases with porosity. At the same time cathode life decreases exponentially with porosity. Therefore in order to obtain long life, high current cathode the range of optimum porosity will be between 15 to 20%.

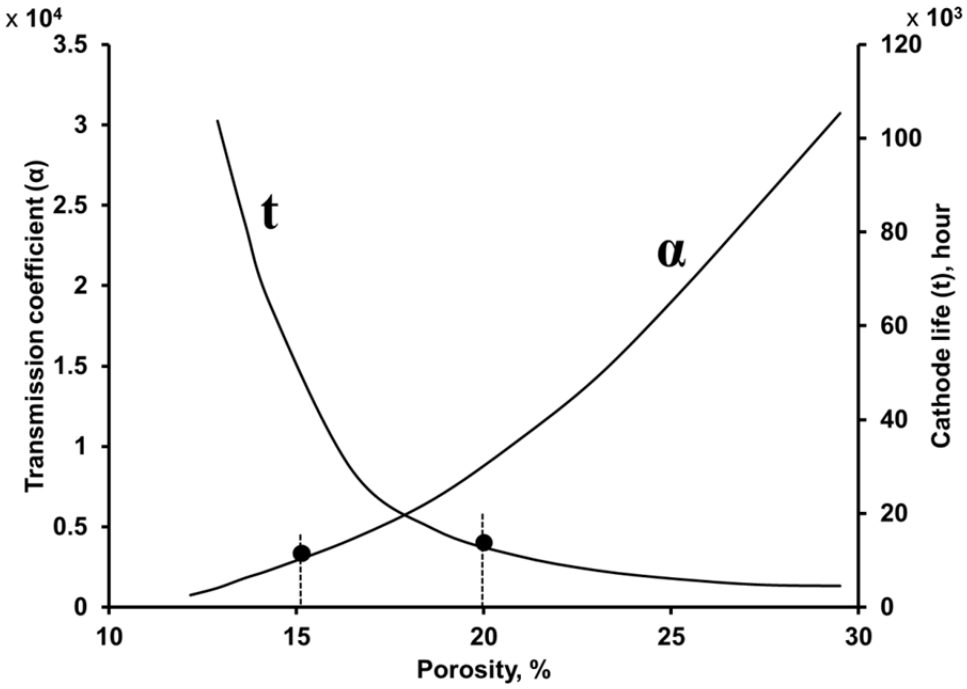

Figure 3.5: Plots of transmission coefficient (α) and life of cathode (t) as a function of porosity.

3.1.3 Influence on the geometry of nanoparticles

The effect of nanoparticle physical parameters on barium flow rate and its distribution across the cathode surface is studied in this section. In order to study the above phenomena, three different pellets was modeled (using COMSOL multi-physics software) using nanoparticles. The particles for three different pellets are as follows: (a) arbitrary shape (figure 3.6), (b) spherical shape with non-uniform distribution (figure 3.7), and (c) spherical shape with uniform distribution (figure 3.8). In the simulation, one of the boundaries is of high pressure (P_0) of barium vapor zone and the other boundary is of very low pressure zone. Based on these conditions, the equilibrium Ba/BaO pressure (P_0) inside the pore of the cathode pellet is estimated. The details of methodology for estimation of Ba/BaO pressure (P_0) inside the pore is given in section 3.1.4.

The simulated results are given in figures 3.6 to 3.8 for the above three different cases (a)-(c). In simulation results dark blue color represents the void pore region, white region indicates the solid particle region, and the green color depicts the flow of Ba/BaO due to pressure difference between two surfaces.

A Schematic 3-D view of cathode pellet made out of random shaped particles, dispersed randomly in the volume is shown in figure 3.6(a). A typical cross sectional view of the matrix is considered as shown in figure 3.6(c). The Ba arrival rate from the pore channels is also shown. Using COMSOL, the Ba arrival rate has been estimated based on differential pressures as explained above. A plot showing the arrival rate along top line of cross section is shown in figure 3.6(b). The aggregate effect over the entire surface due to the Ba arrival from the bulk volume is shown in figure 3.6(d).

The results (a)-(d) obtained corresponding to case 2 and case 3 are shown in figure 3.7(a)-(d) and figure 3.8(a)-(d), respectively. Simulated plot showing Ba arrival rate corresponding to each pore channel are shown in the figure 3.7(b) and 3.8(b), 2-D view used for simulation are shown in the figure 3.7(c) and 3.8(c), and barium arrival rate across the surface from the bulk of matrix are shown in the figure 3.7(d) and 3.8(d).

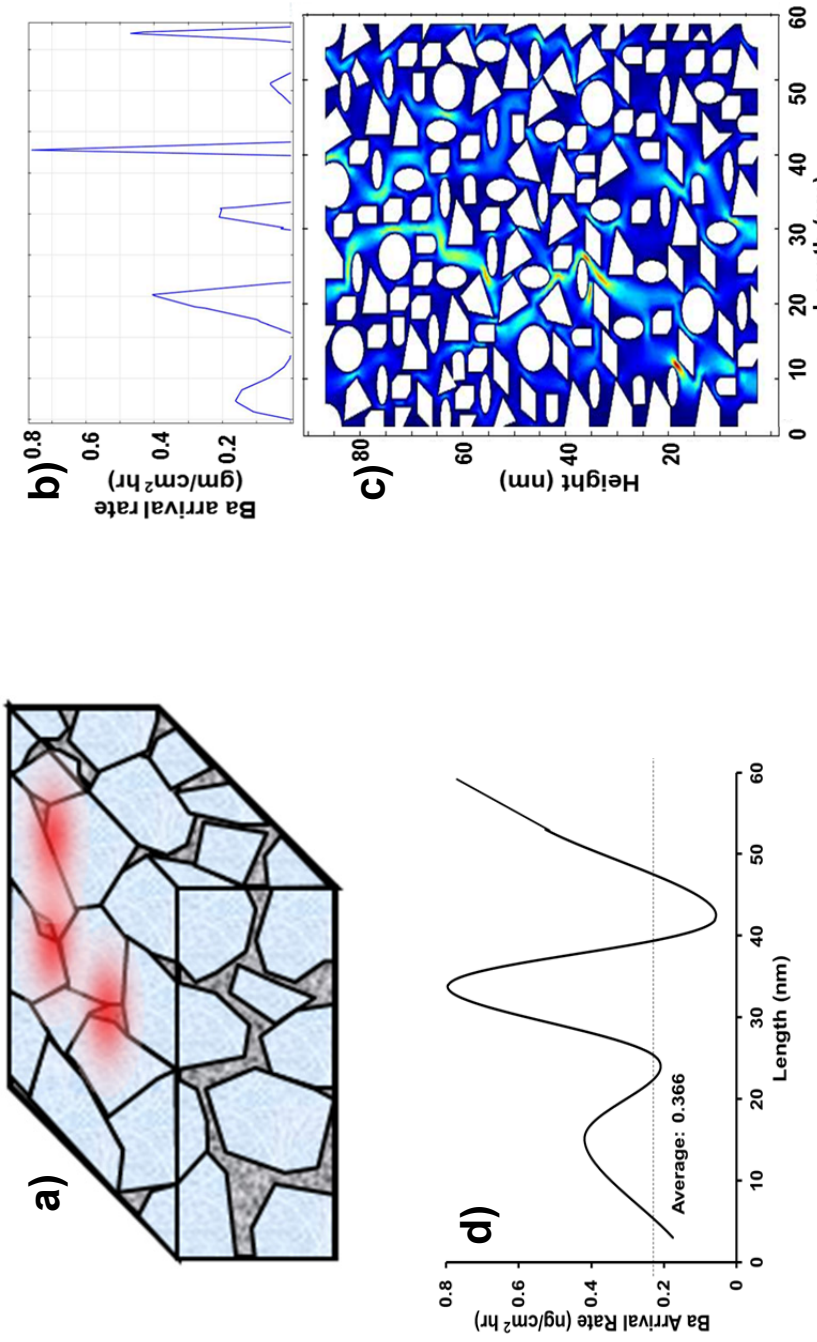

Figure 3.6: (a) Schematic 3-D view of cathode pellet made out of random shaped particles, dispersed randomly in the volume, (b) simulated plot showing Ba arrival rate corresponding to each pore channel, (c) 2-D view used for simulation , and (d) barium arrival rate across the surface from the bulk of matrix

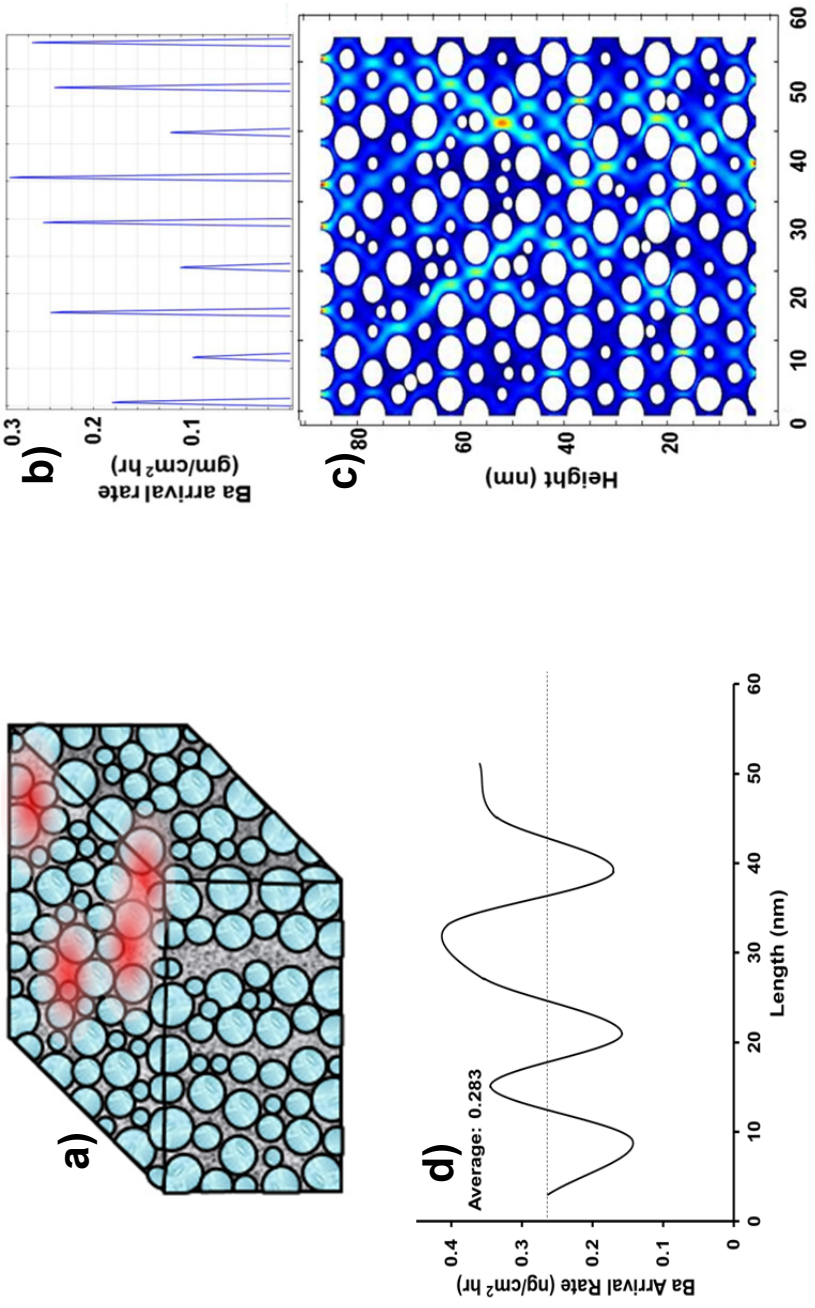

Figure 3.7: (a) Schematic 3-D view of cathode pellet made out of spherical shaped with non-uniform size particles in the volume, (b) simulated plot showing Ba arrival rate corresponding to each pore channel, (c) 2-D view used for simulation , and (d) barium arrival rate across the surface from the bulk of matrix.

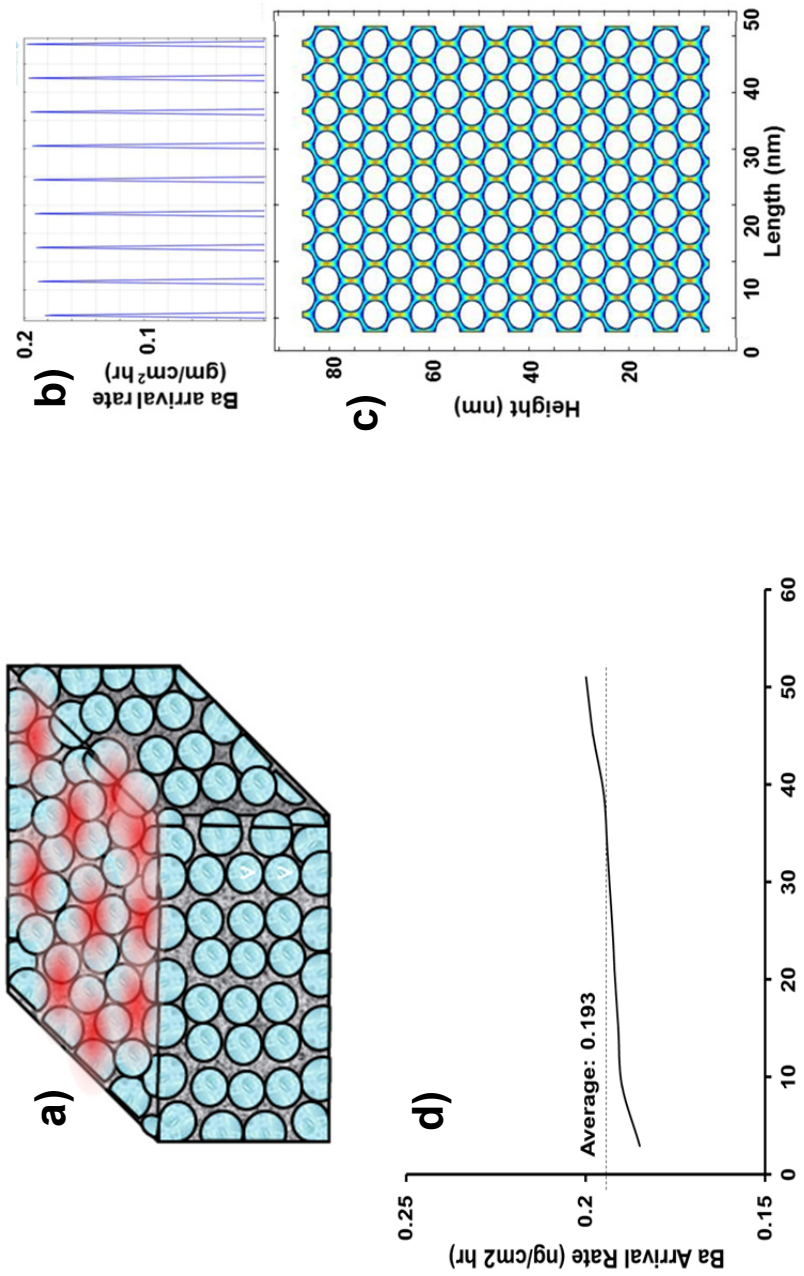

Figure 3.8: (a) Schematic 3-D view of cathode pellet made out of spherical shaped with uniform size particles, in the volume, (b) simulated plot showing Ba arrival rate corresponding to each pore channel, (c) 2-D view used for simulation , and (d) barium arrival rate across the surface from the bulk of matrix

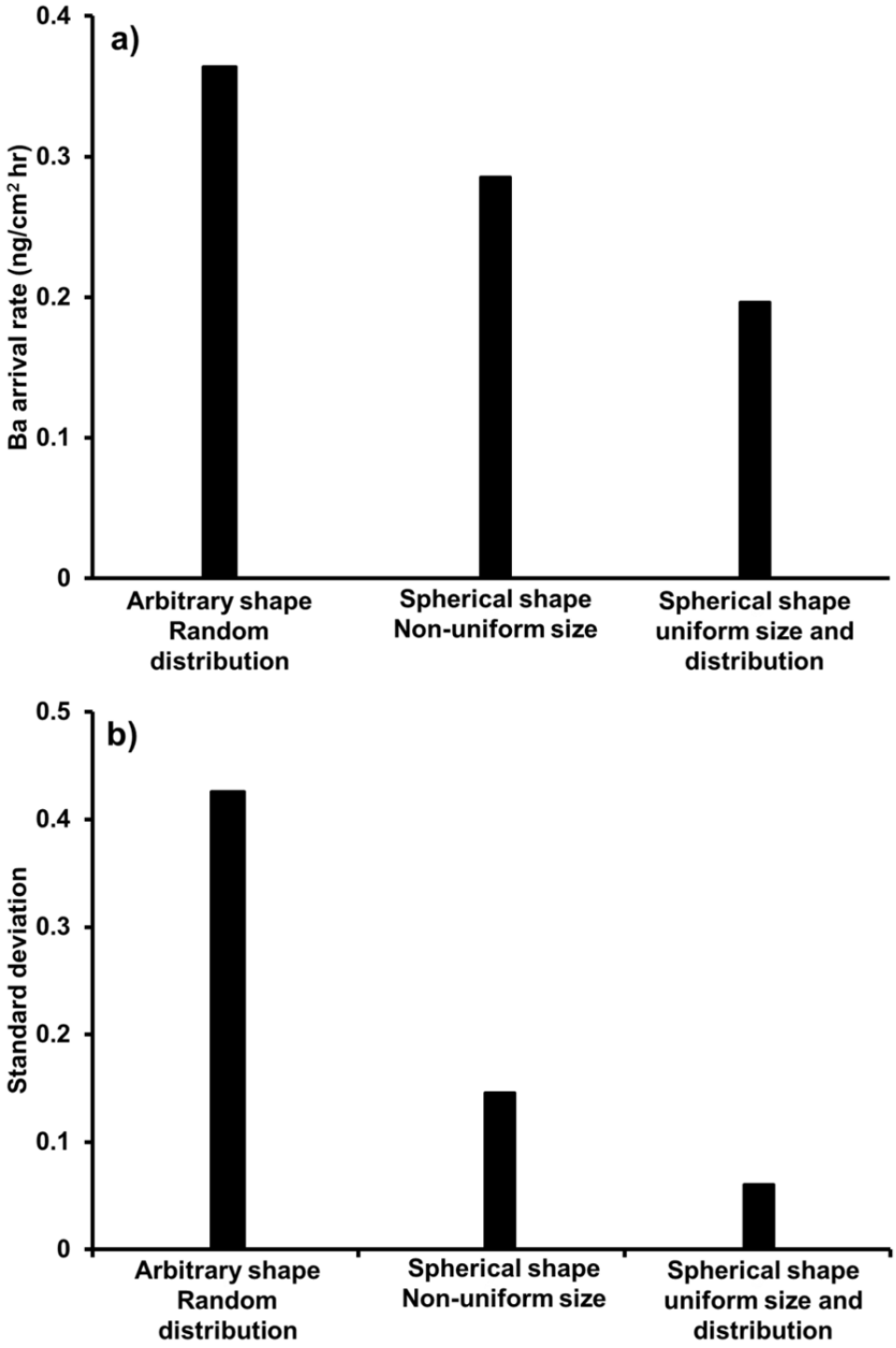

Figure 3.9: Comparison of: (a) barium arrival rate averaged over the entire surface, and (b) corresponding standard deviation for three different cases.

A schematic diagram of a cathode matrix made out of random shaped particles is shown in figure 3.6. For the geometry which has a cross-sectional view as shown in figure 3.6(c) the inter-pore connectivity is poor due to the arbitrary shape of particles, which restrict the Ba/BaO flow through the pores. Figure 3.6 (d) depicts the non-uniform barium coverage across the surface resulting non-uniform emission.

Figure 3.7(a) shows a schematic diagram of a matrix, made out of the particles of spherical in shape, with non-uniform particle size and distribution. The simulation results on the Ba flow (figure 3.7(c)) show that, due to spherical particle shape, the inter-pore connectivity improved as a result the Ba/BaO coverage relatively increased as compared to that of arbitrary shaped particles (as shown in figure 3.6(d)).

Figure 3.8(c) shows the simulated results of Ba/BaO flowing through the pore of an emission matrix made out of spherical shape with uniform particle size and distribution. It shows that (figure 3.8(d)) coverage of Ba/BaO is uniform across the surface. The results indicate that the spherical shape together with uniform size particles improve inter-pore connectivity and uniform pore distribution.

The results corresponding to three different cases are compared at figures 3.9 (a) and (b). The data are plotted in the form of bars separated arbitrarily to illustrate the Ba/BaO arrival rates and standard deviation depicting data for three different cases. It is observed that, in the case of matrix made out of spherical shaped and uniform size particles, the barium arrival rate is lowest at the same time coverage is uniform all across the cross section. Therefore, spherical shape uniform distribution nanoparticle is an optimum choice for high current density long life cathode application.

3.1.4 Estimation of equilibrium Ba/BaO pressure (P_0) inside the pore of matrix

In the cathode under consideration, the barium is impregnated into its porous pellet using barium carbonate. At high temperature $BaCO_3$ reacts with tungsten and decomposed into Ba_3WO_6 and CO as shown in following reaction [54].

$$BaCO_3 + \frac{1}{3}W = \frac{1}{3}Ba_3WO_6 + CO \tag{3.9}$$

The barium necessary to activate the cathode and to maintain the monolayer during life is generated by the reaction

$$2BaO + \frac{1}{3}W = \frac{1}{3}Ba_3WO_6 + Ba \tag{3.10}$$

At equilibrium Ba/BaO pressure (P_0) inside the pore of the cathode pellet is estimated using the following relation [54]

$$\log P_0(mm) = -\frac{16400}{T} + 8.02 \tag{3.11}$$

$For, T = 1100C$

$$P_0 = 1.2 \times 10^{-4} mm = 0.016 Pa \tag{3.12}$$

3.2 Experimental characterization of porosity and pore uniformity

In order to study the particle and pore parameters of the matrix, powder of Sc_2O_3-doped tungsten nanoparticles was taken to form a pellet. Six pellets were made by a die-punch technique. The pellets were sintered at six different temperatures ranging from 1000^0C to 1600°C for 15 minute in a dry hydrogen atmosphere to obtain proper compaction. Next, the pellets were analyzed using SEM in order to observe the porosity, the pore uniformity and the agglomeration tendency of the tungsten nanoparticles. The results are given in figure 3.10(a)–(f). The effective particle size increases with the sintering temperature and that the porosity reduces. It can be seen that for low temperatures the circular shape of the particles is clearly visible (figure 3.10 (a) & (b)). A further increase in temperature gives rise to distortion in shape (figure 3.10 (c) & (d)); while at elevated temperatures the circular shape fully lost and the agglomeration of particles can be clearly seen (figure 3.10 (e) & (f)). It is found essential to sinter at substantially high temperature to retain compactness of the pellet lest the pellet is expected to crumple during handling. It is concluded that in order to get a well sintered pellet it is essential to sinter at a high temperature at the cost of some distortion in spherical shape due to agglomeration of particles.

For a better understanding of the pore size distribution quantitatively across the cross section of the pellet, one of the SEM pictures (figure 3.10 (c)) is utilized. In-house software was developed to measure the effective diameter of the pore by accounting the dimensions in various directions and taking the average value. This data is fed as an input to the software. By knowing the dimension of each pore, a plot has been made to estimate the relative area as a function of pore size. A plot representing this is shown in figure 3.11(a). The peak is spread from 110nm to 260nm with top at the 180nm. It is clear that the maximum number of pores has an average diameter of about 180nm. This value is lower than that of a conventional impregnated cathode (B-type), which has a few microns. As explained at section 3.1.2, low pore size (and hence dense pores) will contribute to lower evaporation

rate and uniform coverage of Ba/BaO. Therefore, optimization of the matrix porosity is critical to achieve long life of cathode.

As the matrix porosity is a function of sintering temperature, it is required to study the effect of sintering temperature on porosity. The porosity of the above mentioned six pellets were estimated using water dip technique [55]. The pellet was heated at 1000^0C temperature in a dry hydrogen atmosphere in order to remove any impurities and water molecules from the matrix. The pellet was dipped into de-ionized water. The weight of pellet before and after dip was noted. By knowing the volume of the pellet and the volume of soaked water, the porosity is estimated using the following relation "porosity = 100 x [void space] / [total space]". The porosity as a function of sintering temperature is plotted in figure 3.11(b). It shows that as the sintering temperature increases from 1000^0C to 1600^0C the porosity decreases from 42% to 11%. It is inferred that the porosity of the pellet can be controlled for a set pressure by sintering temperature which has a bearing on the evaporation and hence the life.

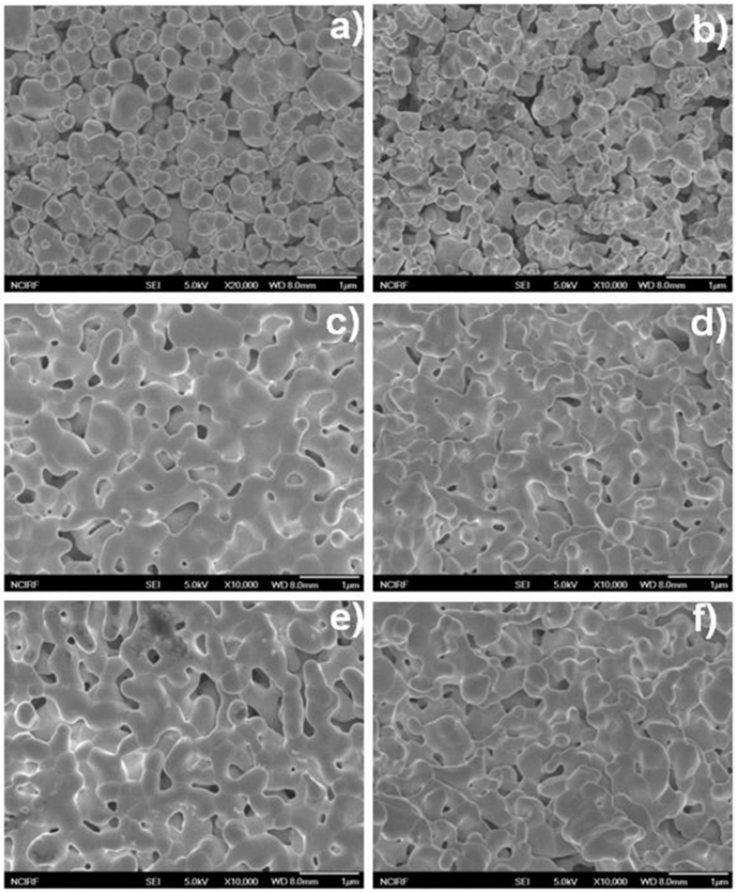

Figure 3.10: SEM images of Sc_2O_3-doped tungsten pellets sintered at different temperatures: (a) 1000^0C, (b) 1200^0C, (c) 1300^0C, (d) 1400^0C, (e) 1500^0C, and (f) 1600^0C.

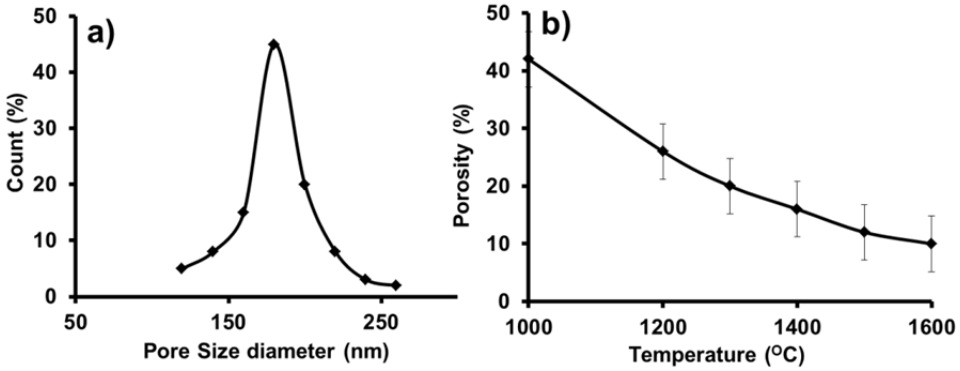

Figure 3.11: (a) Pore size distribution and (b) porosity of the sintered pellets.

Another factor of importance in the emission process is of diffusion of active

material (from the bulk to the surface), which contributes to the surface coverage. Therefore, it is essential to study the diffusion of the material as a function of sintering temperature to estimate the relative compositions of various materials on the surface. To understand this, the pellets were loaded into the analytical chamber containing X-ray photoelectron spectroscopy (XPS) facility. The XPS spectra of five different pellets are shown in figure 3.12. From these spectra it is clear that W signal increases with sintering temperature. The relative concentrations of W, Sc and O are plotted in figure 3.13. From these figures, it can be seen that the concentration of W signal increases with temperature while those of O and Sc reduces. This can be attributed to: (a) partial evaporation of Sc and O at elevated temperatures, and/or (b) inter-diffusion of these elements.

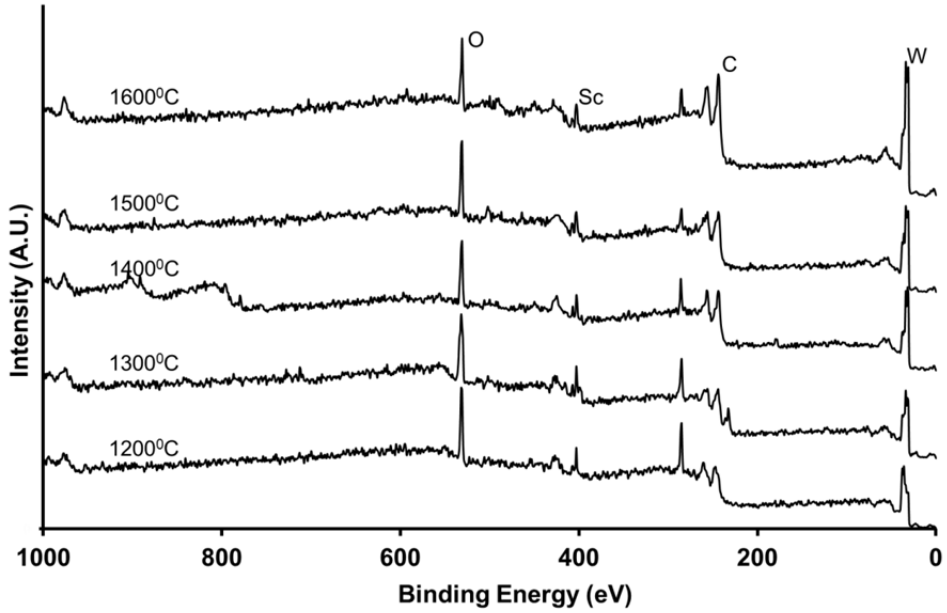

Figure 3.12: X-ray photoelectron spectra of Sc_2O_3-doped tungsten nanoparticle pellets sintered at different temperatures: (a) 1200^0C, (b) 1300^0C, (c) 1400^0C, (d) 1500^0C, and (e) 1600^0C

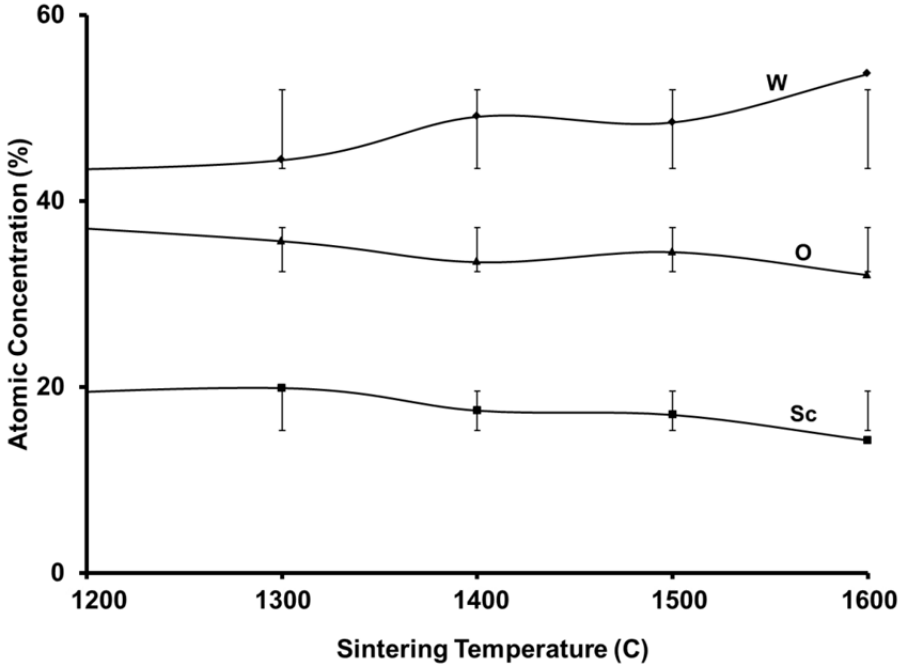

Figure 3.13: Changes of the Sc, W and O atomic concentrations at the surfaces of pellets with the sintering temperature.

3.3 Optimization of cathode surface roughness

The parameters such as surface temperature, roughness, and patchiness influence the beam quality [56]. For a cathode made out of nanoparticles, the surface roughness is primarily decided by the roughness of the die-punch used. The surface finish of the pellet takes exact surface finish of die-punch used at high pressures as the particles of the powder are in nano-scale. Therefore, it is essential to keep the surface of the di-punch ultra-smooth by using electro-polishing technique.

In this section the influence of surface roughness on emission is described quantitatively using analytical relations. The emission current density J as a function of cathode surface temperature T under temperature limited region is given by [57]

$$J = A_0 T^2 \exp\left(\frac{-\varphi}{kT}\right) \tag{3.13}$$

Where, $A_0 = 4\pi mk^2e/h^3 = 120 A/cm^2 \bullet K^{-2}$ is a fundamental constant, T is the temperature in K, and φ is the work function of the surface. Here, the temperature T of emission surface is a critical factor that determines the current density J, which is dependent on emissivity E_n of the emission surface. The energy radiated by a hot body to its surroundings P can be written as [57]

$$P = E_n \sigma' A(T^4 - T_c^4) \tag{3.14}$$

E_n is the emissivity of the emission surface, A is the radiating area. σ' is the Stefan-Boltzmann constant, T is the surface temperature and T_c is the surrounding temperature. The emissivity of a material E_n is the relative ability of its surface to emit energy by radiation which is a depending factor of the surface roughness of the material [58]

$$E_n = \left[1 + \left(\frac{1}{E_s} - 1\right) R\right]^{-1} \tag{3.15}$$

where R is the roughness factor which is given by

$$R = \left(1 + \left(\pi n \sigma\right)^2\right)^{-1} \tag{3.16}$$

where, E_s is the effective emissivity of smooth surface, n is the number of intersections of the surface profile with the mean per unit length of the mean line, and σ the mean-square deviation of the profile from the mean. For rough surfaces, σ can be expressed in terms of the mean arithmetic deviation, R_a, of the profile according to relation $\sigma = 1.25\ R_a$. Therefore, (3.16) can be written as

$$R = \left(1 + \left(1.25\pi n R_a\right)^2\right)^{-1} \qquad (3.17)$$

From above equation one can found that as the surface roughness R_a increases, the roughness factor R decreases which increase the emissivity. As a result radiation power loss P will increase, effective surface temperature T decreases and drastically reduced the emission current density J.

The above studies suggest that it is essential to mirror polish the surfaces of die-punch system while making the pellets out of nanopowder. The surface roughness profile and corresponding roughness histogram are shown in figure 3.14. The histogram is made by accounting the number of points which lie in different ranges of the roughness height. The average value of roughness of cathode surface is found to be about 250 nm.

From the above surface roughness data the estimated emissivity value and the corresponding emission current density are found out. The sequence of calculation is as following:

(a) after machining/pressing of pellet the values R_a, σ and n are obtained from profile measurement
(b) using (3.16) or (3.17), the roughness factor R is estimated.
(c) using (3.15), the emissivity value E_n is found out.
(d) using the above value of E_n, the surface temperature T is estimated for a chosen radiated power P by using (3.14).
(e) Finally, the value of J is estimated for chosen value of work function using (3.13).

The variation of emission current density (J) with average surface roughness (R_a) has been plotted in Figure 3.15. It can be seen that J falls rapidly beyond surface roughness of 0.5μm. From this plot it can be inferred that it is necessary to keep the roughness below 0.5μm.

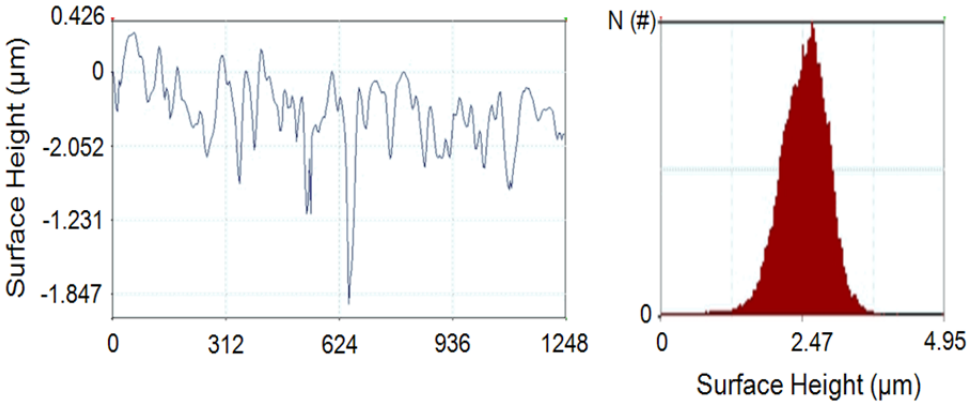

Figure 3.14: Experimental results on surface roughness measurement: (a) Surface profile and (b) histogram representing the relative percentage of heights as a function of surface height.

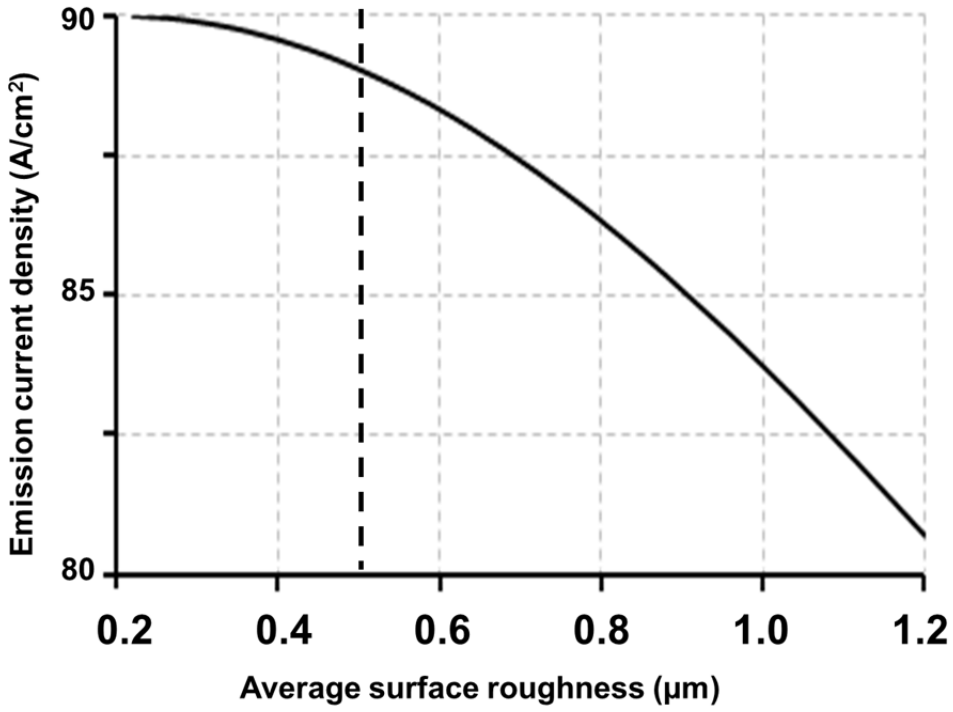

Figure 3.15: Average surface roughness vs. emission current density plot.

3.4 Thermal design and experimental validation of cathode assembly

The operation of tube begins only after the cathode attains its operating temperature. The transfer of thermal energy from the heater to the cathode surface depends significantly on the intermediate potting medium, which is conventionally made out of non-shrinkable alumina. At high temperature the heat loss is primarily due to radiation. The conduction loss through mechanical support is also a prominent factor in a thermal design. Extensive thermal analysis is required in order to obtain minimum heat loss and maximum pellet temperature with minimum heater power. It is to be noted that the choice of the materials for a cathode assembly is limited due to its operation at elevated temperatures. The materials like platinum, titanium, etc., cannot be used near the cathode as they may poison the cathode surface and degrade the emission [59], [60]. Mo, Mo–Re and Ta are some of the commonly used materials in cathode assembly. Thermal conductivity and the geometry of a supporting sleeve play a critical role in deciding the surface temperature. Lesser the thermal conductivity of the material the more will be the rise in temperature of the cathode button. The temperature of cathode button also varies with the thickness of the outer sleeve. The cathodes were designed considering: (a) a low thermal conductance, (b) good mechanical support, and (c) a set of thermal shields so that a maximum heater power can be directed towards the surface of the pellet.

Recently researchers have reported their theoretical analyses of a cathode considering a nonporous potted heater and ideal/non-ideal interface conditions [61], [62]. In their simulation studies, it was also considered that both the pellet and the potting cylinder are free of voids/pores (100% material compaction). However, in actual practice, 100% compaction cannot be possible in the potting due to the pores/ micro-voids exist even after sintering at elevated temperatures. In the case of the pellet, the voids, typically 20%, are necessary for impregnation.

In the present simulation work, effective densities are considered for both the pellet and the potting by accounting 20% porosity and possible voids, respectively. A steady state thermal analysis has been carried out at various heater powers levels

using ANSYS software. A solid model of cathode assembly used for simulation is shown in figure 3.16(a). The photograph of fabricated cathode assembly is shown in figure 3.16(b). The simulation result is depicted in figure 3.16(c). The simulation result shows that, at 5W input heater power the maximum pellet temperature obtained is 1100^0C. To validate the simulated results, a simple laboratory set up has been developed. A pellet was made by pressing the tungsten nanopowder and was sintered. The pellet is integrated with the molybdenum sleeve using laser welding. Subsequently heater potting was carried out. The cathode assembly was kept inside a bell jar of the above vacuum system. Vacuum is created in this bell jar with a combination of an ion pump and a turbo molecular pump. A photograph showing the cathode assembly inside the bell jar is shown in figure 3.17.

The system is evacuated and baked to obtain vacuum in the bell jar below $2x10^{-8}$ Torr. The surface temperature as various heater powder levels were measured using a disappearing filament pyrometer. The brightness temperature of the surface is converted into the actual temperature considering the emissivity on W surface. These results are compared with the simulated results obtained from ANSYS software. Figure 3.18 shows the simulated and the experimental results on the variation of surface temperature as a function of heater power. A good agreement is found between these two results. Slight mismatch at the higher wattages is attributed to the: (a) connecting lead losses, (b) slight inaccuracy in the assumption of interface resistance in the model, and (c) imperfections in the heater wire causing non-uniform resistance (and the hence consequent joule heating) all along the length of the wire.

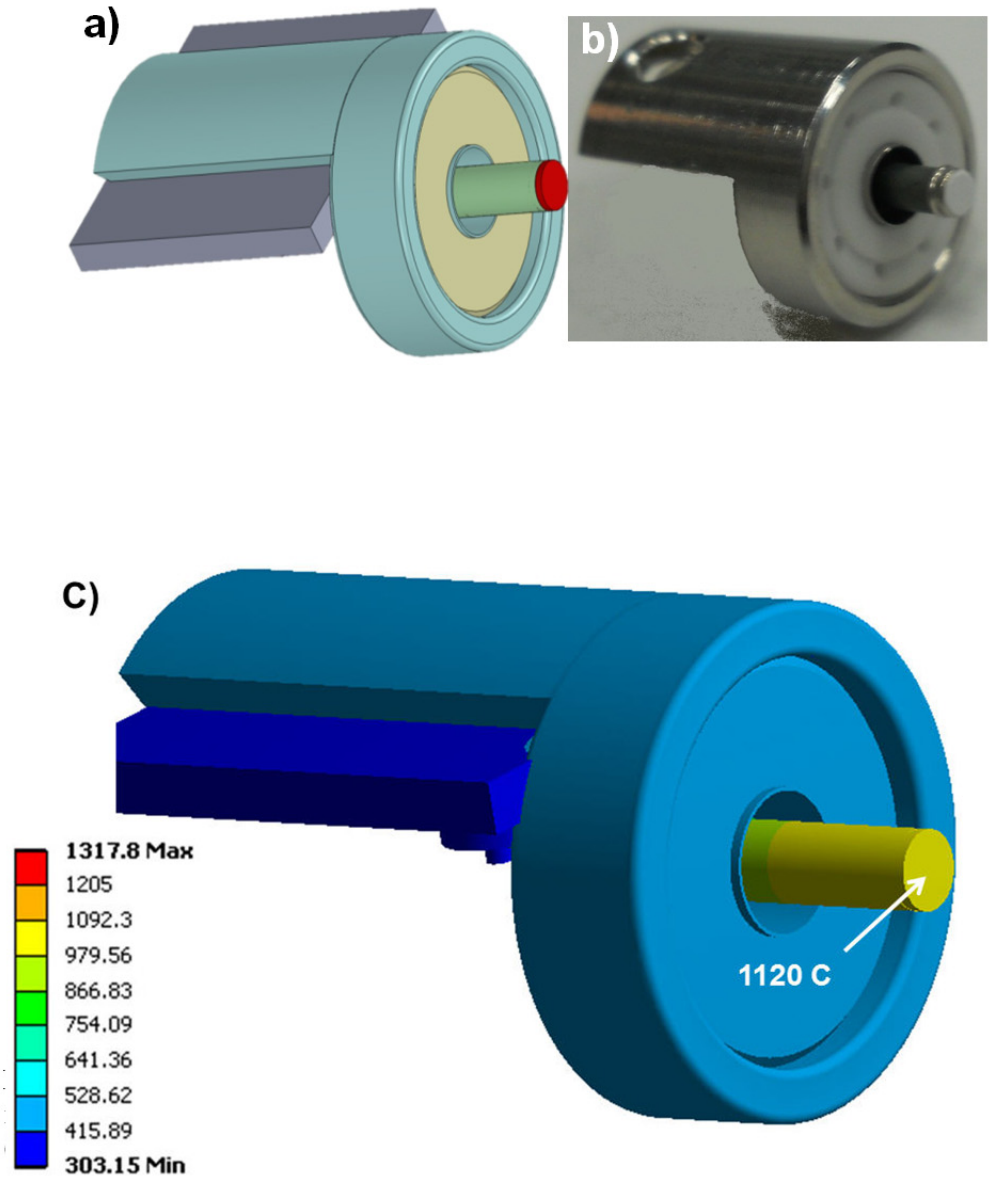

Figure 3.16: Geometry of cathode assembly: (a) solid model used in ANSYS and (b) photograph of the cathode assembly used in the analysis, and (c) figure generated by ANSYS software showing the temperature distribution.

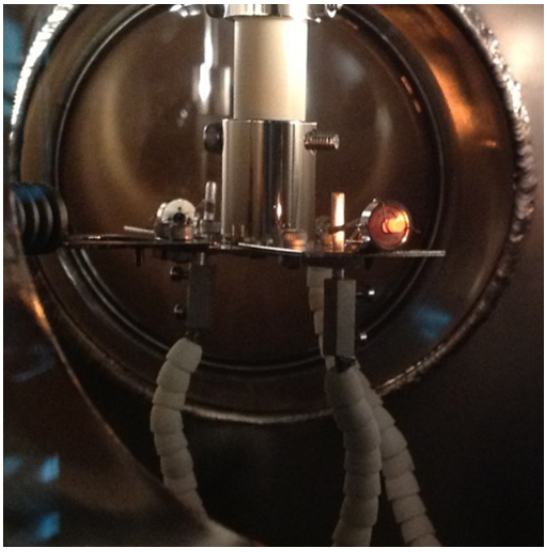

Figure 3.17: Photograph of cathode assembly inside the bell jar of vacuum system, used for temperature measurements.

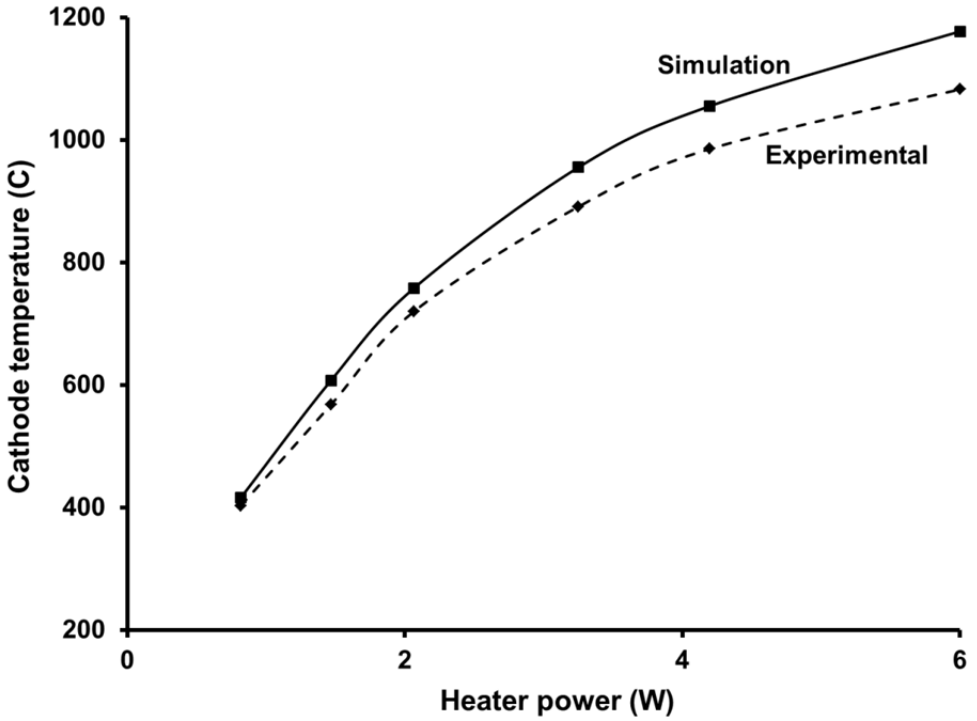

Figure 3.18: Plots of heater power versus cathode surface temperature: simulated and experimental results.

CHAPTER 4

Realization of nanoparticle based cathode

4.1 Fabrication of cathode

4.1.1 Conventional fabrication technique

4.1.2 Modified fabrication technique

4.2 Details of experimental setup for emission measurements and surface characterization

4.3 Characterization of cathode

4.3.1 Emission measurement

4.3.2 Characterization of emission surface using AES

4.3.3 Estimation of cathode life using accelerated life testing

4.1 Fabrication of cathode

A scandia-doped tungsten nanoparticles powder was made using *sol-gel* method as discussed in section 2.4. The average particle size was found to be about 100nm. This powder was used as a raw material for fabrication of cathode pellet. The detail of fabrication process using conventional technique is explained in following section.

4.1.1 Conventional fabrication technique

Two molybdenum sleeves were made for containing the nanopowder and for potting of heater, respectively. The first one was made by turning while the latter was made by wrapping technique. The pellet was made by pressing the pre-determined amount of powder to obtain a thickness of 1.0mm. Heater potting was carried out by burying the filament into the wrapped sleeve and subsequently sintering. The pellet was integrated with the potting assembly by laser shining. A schematic process diagram of cathode fabrication using scandium-doped tungsten nano-particle is shown in figure 4.1.

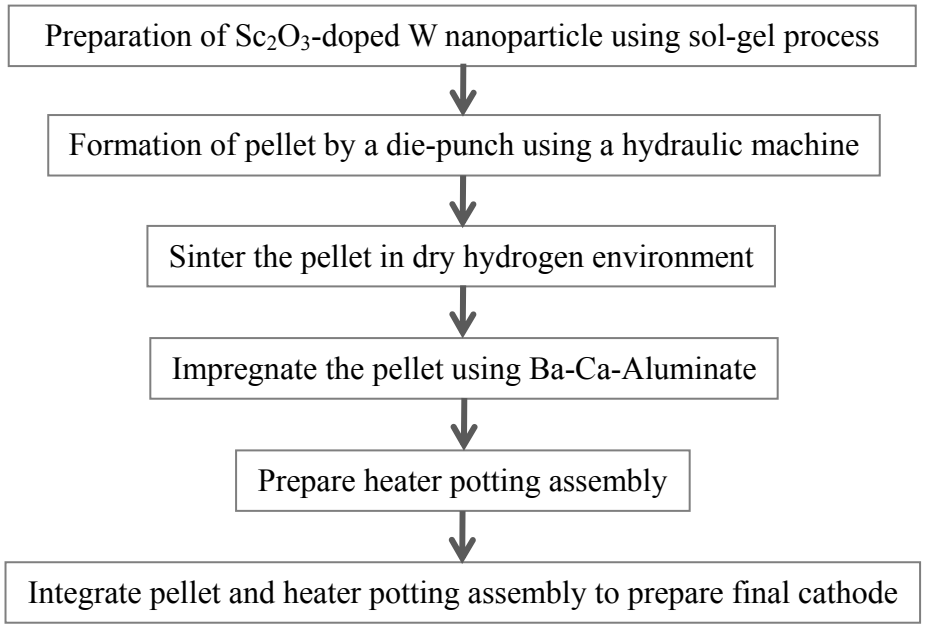

Figure 4.1: Schematic of conventional process diagram of cathode fabrication.

During pellet sintering process, compactness of the pellet achieved with the cost of low porosity and degradation of particle shape from spherical to arbitrary shape as discussed in section 3.2. Low porosity resists the impregnation of active material into the bulk through the pores. This failure to fabricate the cathode using conventional technique motivated to adopt a modified fabrication technique.

4.1.2 Modified fabrication technique

Schematic diagram of modified fabrication process using scandium-doped tungsten nano-particle is shown in figure 4.2. The detail explanation of fabrication process is explained below:

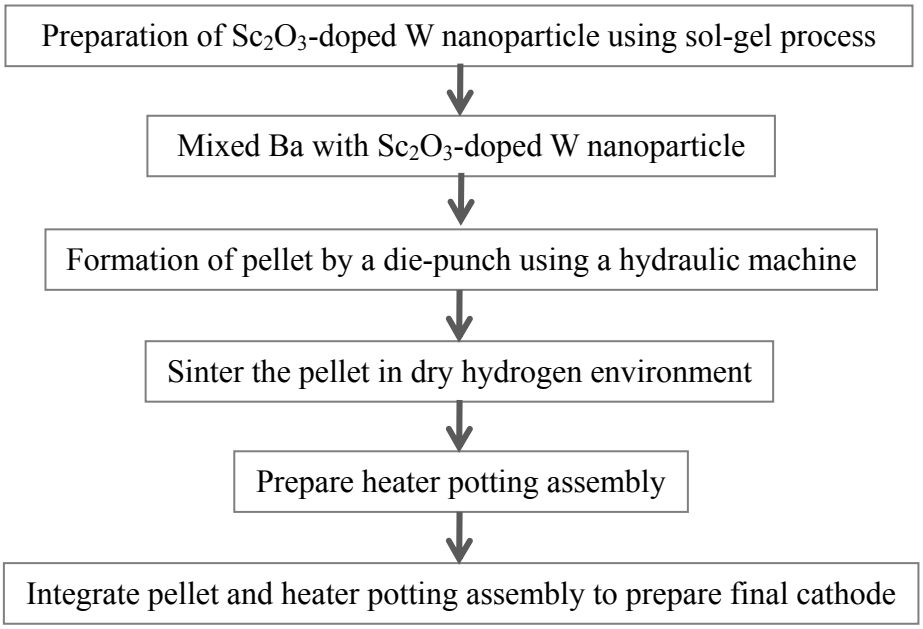

Figure 4.2: Schematic of modified process diagram of cathode fabrication.

1) **Fabrication of pressing jig:** A specially designed pressing die-punch was fabricated using die-steel. The surface was polished using a fine sand paper at very high rpm to achieve mirror finish.
2) **Preparation of active compounds:** $BaCO_3$, $CaCO_3$ and Al_2O_3 were taken in 4:1:1 molar ratio. The mixture was ground by ball milling for 72 hours. Finally 20% by weight of this powder was mixed with scandia-doped tungsten nanopowder. This mixture was ground again using agate mortar.
3) **Pressing and sintering of pellet:** Four pellets were made out of the above powder by pressing it into a molybdenum sleeve using a die-punch. The thickness of pellet (1.0mm) was controlled by taking a pre-determined amount of powder. Out of the above four two cathodes (named S-W_01 and S-W_02) were sintered at 1700^0C and the other two (named S-W_03 and S-W_04) at 1500^0C. A schematic diagram and its photograph of S-W_03 is shown in figure 4.3.
4) **Assembly of cathode:** A filament was introduced into the molybdenum sleeve and was buried with a non-shrinkable alumina powder. For this potting the sintering of alumina was carried in a high temperature furnace at 1700^0C for a duration of 15 minutes. The above sintered pellet was integrated with this potted heater assembly using laser tagging to make a complete cathode assembly. The assembly is tested in an UHV chamber containing: (a) anode for emission measurement, and (b) Auger Electron Spectroscopy (AES) for surface characterization.

The geometrical details of the cathode assembly together with the photograph are shown in figure 4.3. The details of die-punch together with the photograph are shown in figure 4.4.

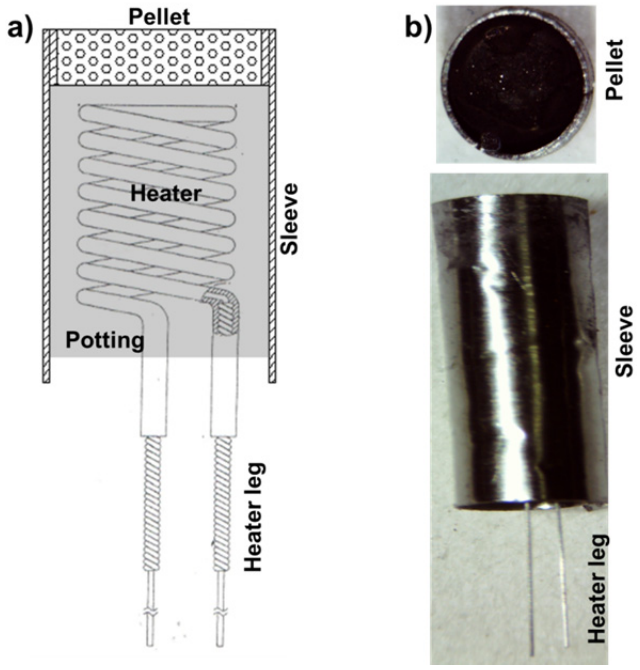

Figure 4.3: Cathode assembly: (a) cross sectional view and (b) photograph.

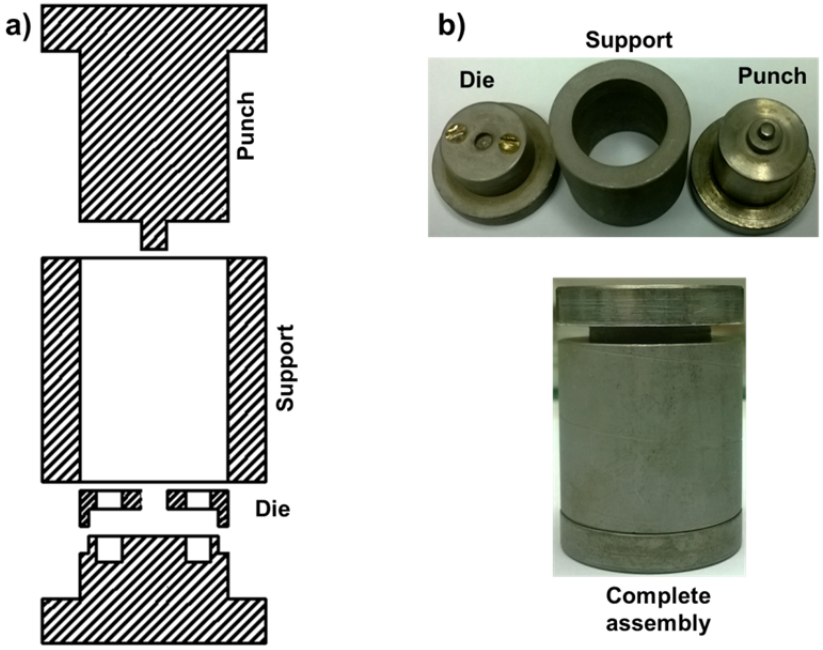

Figure 4.4: Die-punch assembly used for fabrication of pellet out of nanopowder: (a) cross sectional view and (b) photograph.

4.2 Details of experimental setup for emission measurements and surface characterization

The emission measurements and surface characterization were carried out in an analytical UHV system. A schematic diagram of the bell jar containing various facilities is shown in figure 4.5. The photograph of the system is shown in figure 4.6. The bell jar consists of: a) cylindrical mirror analyzer (CMA) for Auger electron spectroscopy (AES) analysis, b) mass spectrometer (MS) for studying residual gases, (c) anode for emission measurements, and (d) thermionic emission microscope (THEM) for emission topography. Several cathodes can be fixed onto the carousel which can be moved *in situ* by the sample manipulator to face the cathode towards any of the above analytical facilities. The chamber is pumped by a turbo molecular pump for the ion pump to take over. Heating tapes are used to heat the chamber enabling the removal of the trapped gases. Once the vacuum reached 10^{-5}Torr, ion pump is operated to achieve a vacuum of 10^{-9} Torr. A vacuum of 10^{-9} Torr is considered good for testing of cathodes. The system is baked for 50 hours to achieve a final vacuum of 7.0 x 10^{-9}Torr. A vacuum of 10^{-9} torr is considered good for testing of cathodes.

The fabricated cathodes were assembled and tested in an analytical system shown in figure 4.6, which is fitted with anode and Auger electron spectroscopy (AES). The cathodes are mounted on the carousel as shown in figure 4.7. The connections are made using nickel tapes and beads (glass to Kovar). The carousel is fitted inside the chamber and proper electrical connections are made by ensuring no cross connections.

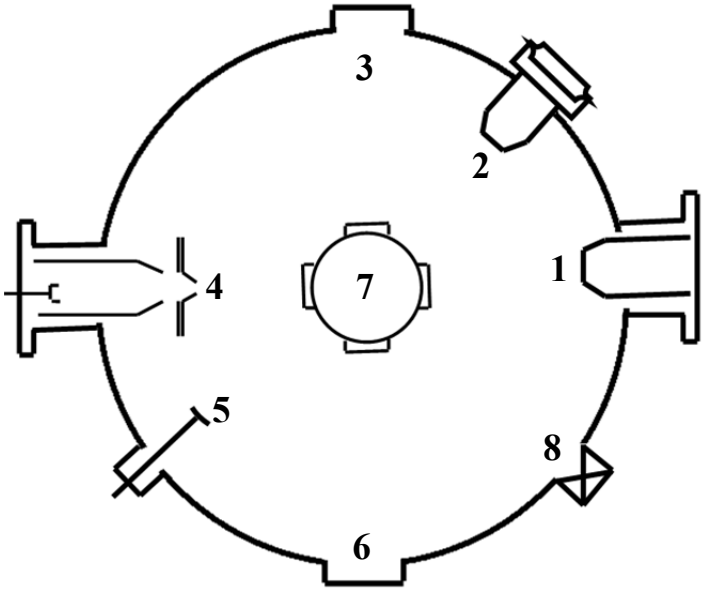

Figure 4.5: Schematic diagram of bell jar system: (1) CMA, (2) mass spectrometer, (3) viewing window, (4) THEM, (5) Planar anode, (6) flange for mounting, (7) carousel, and (8) vacuum gauge.

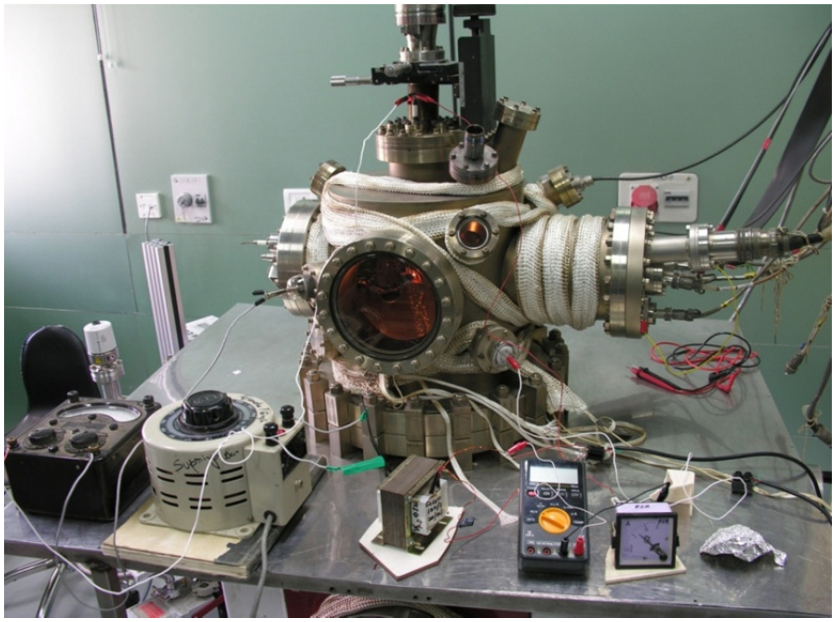

Figure 4.6: Photograph of analytical system.

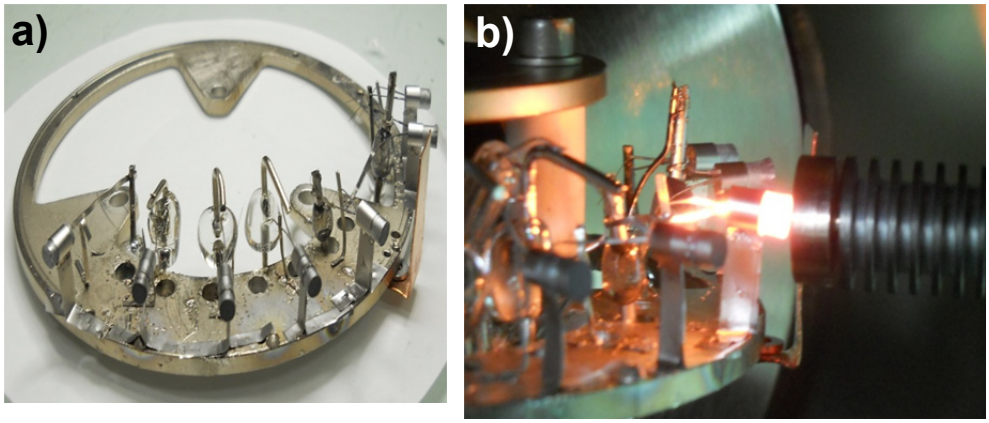

Figure 4.7: Photograph of (a) cathodes mounted on carousel (b) Cathode in front of molybdenum anode during activation.

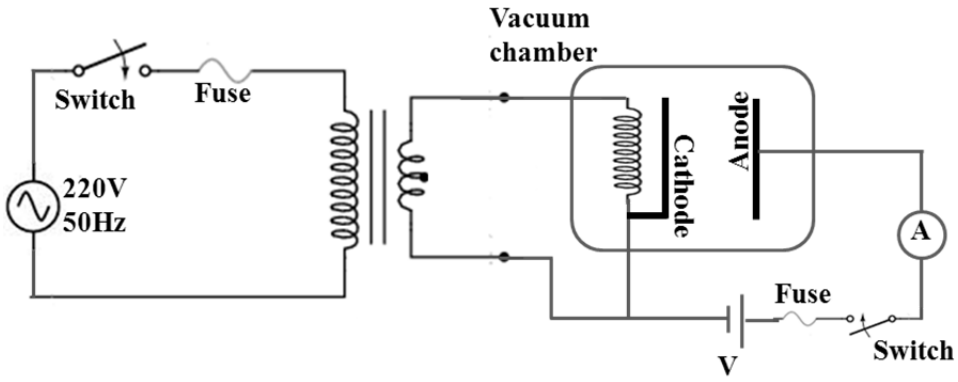

Figure 4.8: Circuit diagram for cathode testing

4.3 Characterization of cathode

Activation of cathode is very important in order to oxygenate the active monolayer over the surface. This oxygenating process being diffusion process takes time and is temperature dependent. The first step of activation is to remove any sort of surface contamination by heating the cathode to dull red condition. During this process, cathode should be far enough from anode in order to avoid anode contamination. Then the cathode is brought in front of the anode with the help of sample manipulator and current is drawn by supplying positive DC voltage to anode as shown in figure 4.8. In order to remove anode contamination, anode degassing is essential need by drawing large current till the molybdenum anode is dull red. After the vacuum stabilized, a high voltage in pulse mode is connected to the circuit to obtain pulse current.

One leg of the filament is shorted with the cathode body and other remains floating. An alternating current is supplied through the floating leg resulting in heating of cathode. The temperature of the cathode was measured using disappearance filament type optical pyrometer which gives the brightness temperature rather than the actual temperature. Voltage between the cathode and anode was measured by a CRO. High voltage probe was used to measure the voltage and is fed to CRO. Similarly current transformer is used and feed to CRO to measure anode current.

Pulsed current was drawn after the cathode is fully activated. For a particular cathode temperature, the pulsed voltage is varied and anode current is measured using CRO. The same procedure is followed for different cathode temperature. The main precautions that one needs to take while drawing currents are:

1. The vacuum level should not go beyond mid 10^{-8} Torr, to ensure poison free cathode surface.
2. It should be ensured that no arcing takes place between cathode and anode.
3. The anode does not become too hot in the process of drawing current.

4.3.1 Emission measurement

To find out the emission capability of the cathode pulsed emission measurements were carried out. The cathode was kept parallel to the anode at a distance of 1 mm to form a plane parallel diode. The out gassing of cathode was carried out by gradually rising the heater power and keeping the surface temperature at about 1100^0C_B for 15 minutes. DC voltage is applied across the diode to draw emission current of about 50mA for 100 hours. The DC is replaced by pulse to draw current densities of beyond 80A/cm^2. The I-V data were obtained at different cathode temperatures to make Childs' law plots. These plots are shown in figure 4.9. Along with these plots, the perveance line was drawn to show the deviation of curves from the line to depict the space charge and saturation regions. It is interesting to note that the I-V characteristics are exhibiting a non-saturation behavior (field enhancement) at higher anode fields. This behavior is attributed to the formation of a substantially thick semiconducting active layer on the surface after full activation. This can be further corroborated with the AES data as shown in figure 4.10 which shows a high coverage of active material as compared to a conventional B-type cathode [2]. It is concluded that the high emission and the field enhancement are attributed to the thick coverage of active material on the surface.

The work function is determined using 73% slope method [2]. The work function is found to be about 1.75eV. A space-charge limited emission of >60A/cm^2 is obtained at 1080^0C_B from this cathode. The work function is calculated using Richardson-Dushman equation as follows

$$J_0 = A_0 T^2 \exp\left[-\frac{\phi}{kT}\right] \tag{4.1}$$

$$\phi = kT \ln\left[\frac{A_0 T^2}{J_0}\right] \tag{4.2}$$

Here J_0 is the zero-field current density, A_0 = (120A/cm^2/K^2) is the Richardson's emission constant, T is the temperature in kelvin, Φ is the work function of cathode, and k is Boltzmann's constant.

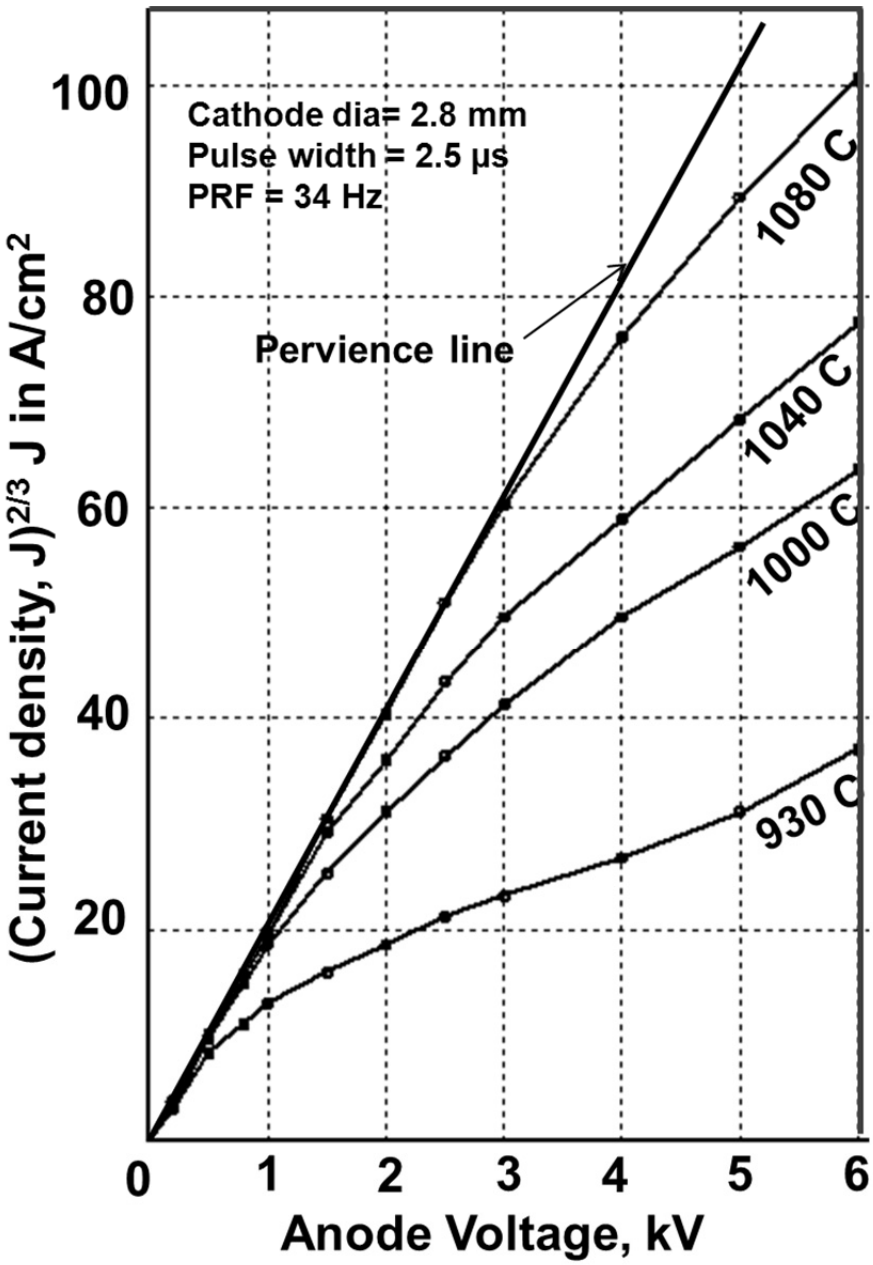

Figure 4.9: $J^{2/3}$ vs. V plots of Sc-doped cathode(S-W_03) at different temperatures.

4.3.2 Characterization of emission surface using AES

Emission depends on the formation of active layer on the surface. Therefore, the characterization of surface is needed in order to understand the role of chemical composition at different stages of cathode activation. One of the commonly used tools for cathode surface characterization is of Auger Electron Spectroscopy (AES). Since Auger electrons are characteristic electrons of an atom, the spectra obtained at different spots represent the elemental composition of the surface. The Auger peaks are found in the background of the secondary spectrum, hence to obtain Auger spectrum the secondary spectrum is differentiated with respect to energy. The peaks at different energy in the Auger spectrum are characteristics of different element found on the surface. Hence, the knowledge of peak at particular energy confirms the presence of that particular element.

AES spectra taken at several stages of activation are shown in figure 4.10. In this figure the characteristic peaks corresponding to various elements such as tungsten, scandium, oxygen, and barium are shown. The presence of scandium can be seen from the low energy peaks in figure 4.11(a). Scandium is present in the form of scandia (Sc_2O_3) which is evident from the doublet [2] at 360eV in figure 4.11(b). The variation of elemental concentration with time at different stages of activation is shown in figure 4.12. It was found before activation the concentration of tungsten was high and that of other element was low which indicates a clean tungsten surface in the infant stage. Over the time the concentration of tungsten gradually decreased while the concentration of other elements increases. The time taken for the formation of thick active layer is about 200 hours. It was also found that from the I-V characteristics the prominence of field enhancement starts from about 150 hours of operation at 1080^0C_B.

It was found that the emission of S-W_01 and S-W_02 was poor. The AES studies showed a low coverage of active material (Ba/BaO) on the surface. The AES spectra taken at two different stages of activation are shown in figure 4.13. This is attributed to the evaporation of Ba/BaO during the sintering at elevated temperature (1700^0C).

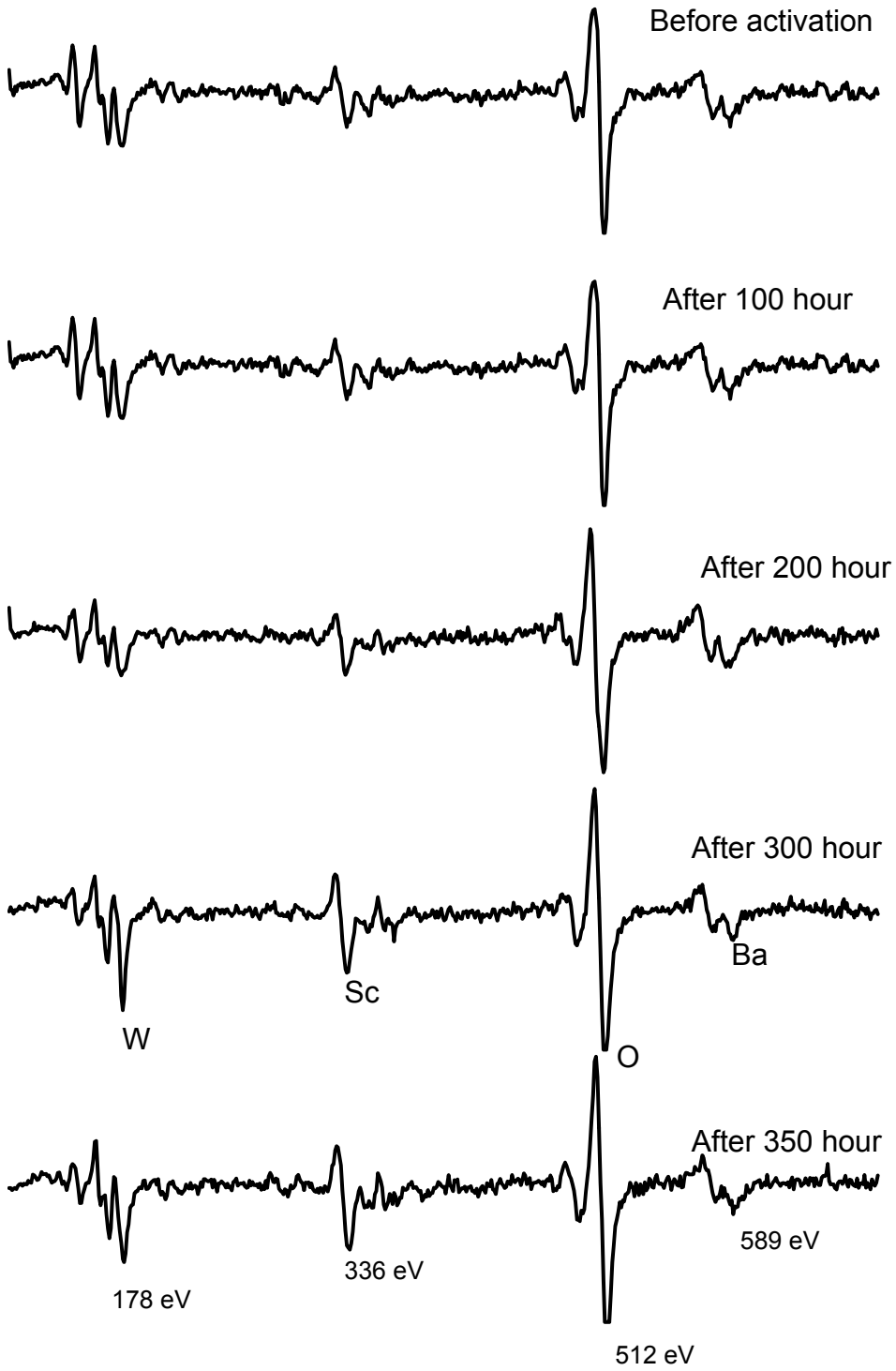

Figure 4.10: AES spectra of S-W_03 taken at several stages of cathode activation.

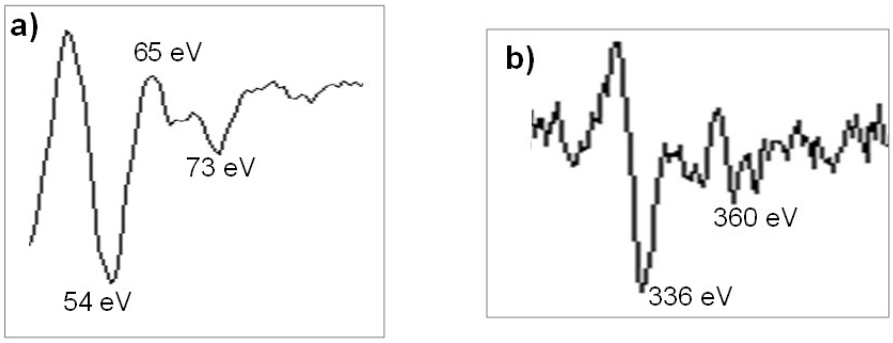

Figure 4.11: AES spectra of S-W_03: (a) Low energy peak and (b) expanded view of scandium signal

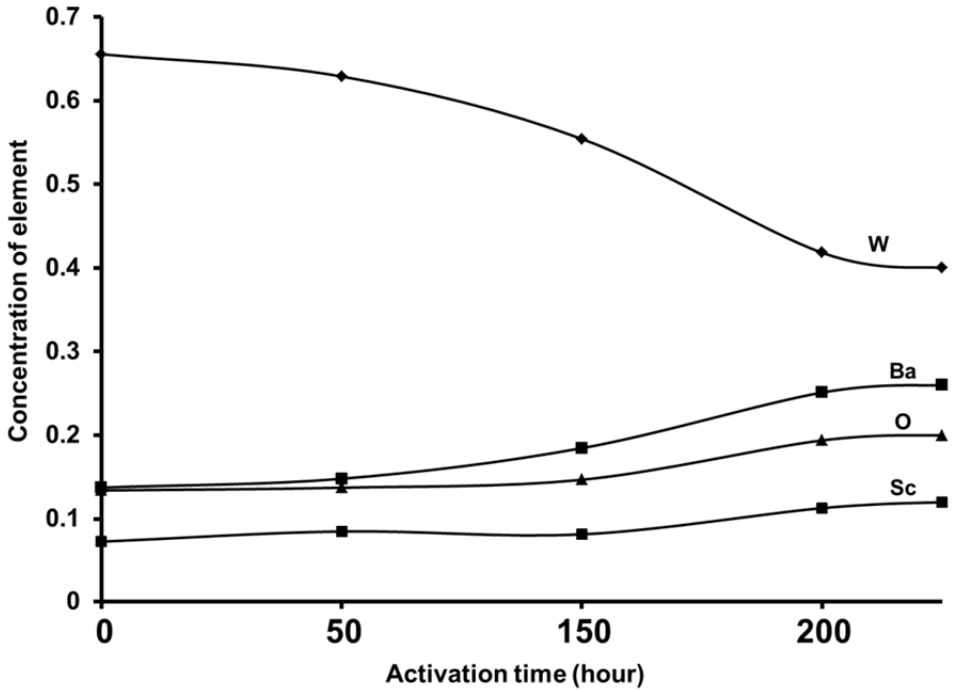

Figure 4.12: Concentration of various elements taken at several stages of cathode activation.

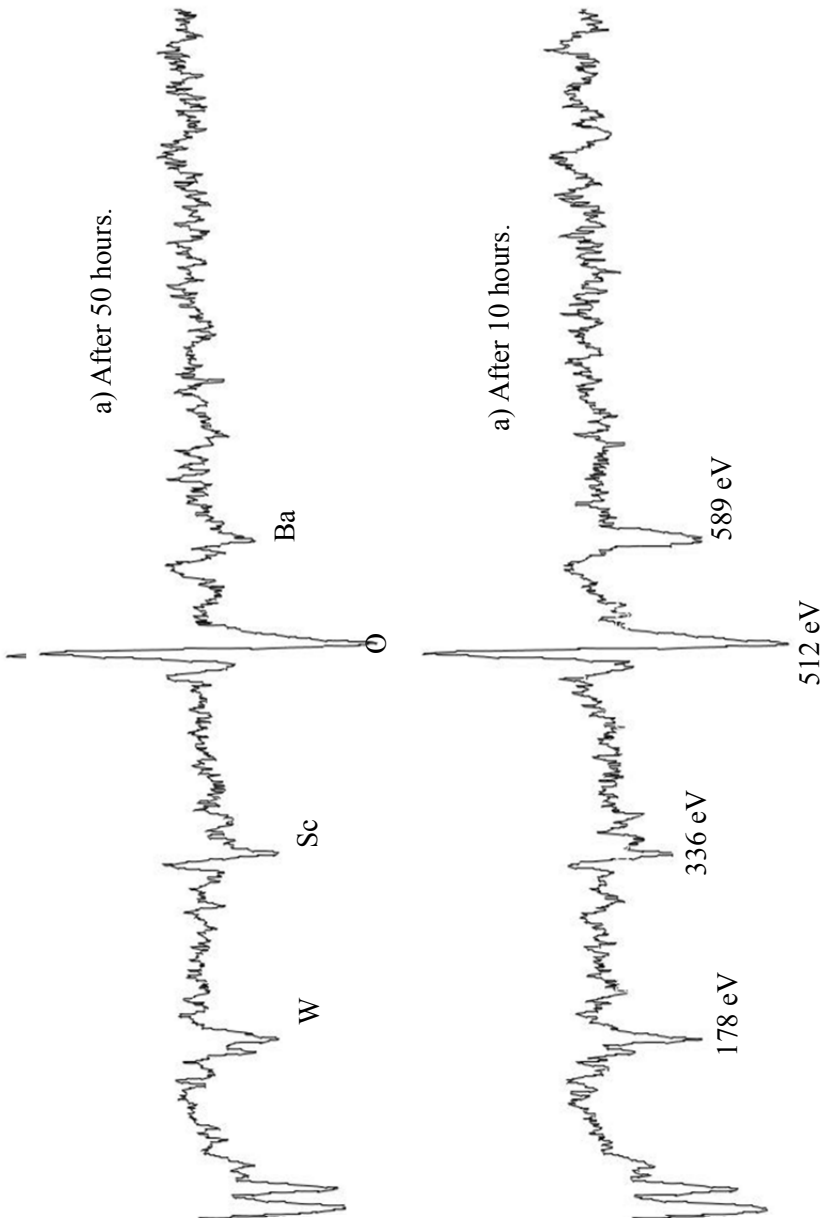

Figure 4.13: AES spectra of S-W_01 taken at two different stages of cathode activation: (a) after10 hours and (b) after 50 hours.

4.3.3 Estimation of cathode life using accelerated life testing

To ensure the life of the cathode two cathodes were mounted into continues life test in closed-spaced diode. The schematic diagram of closed-spaced diode is shown in figure 4.14(a). The cathode diameter was 2.8mm and cathode anode separation was maintained about 1 mm. The anode was fabricated in corrugated structure in order to increase heat dissipation.

To estimate the life of the cathode, the cathode was kept in an elevated temperature at 1120^0C. This process can be called as accelerate life test. During accelerated life test, 1A current was drawn using 1kV DC anode voltage in order to avoid anode overheating. If 10% drop of emission current occurred, the cathode will be presumed to reach the end of its life. The emission current is monitoring in every 500 hours. The average emission current density was found about 15A/cm^2. The emission current density remained constant without any deterioration for ~2500 h and the test is still ongoing.

From accelerated life test data, it is possible to extrapolate life of cathode at operating temperature by estimation the rate of barium evaporation. The rate of barium evaporation can be written as [2]

$$M = K \exp\left\{-\left(\frac{e\varphi}{kT}\right)\right\} \tag{4.3}$$

where, $e\Psi$ is activation energy for desorption in eV, k is the Boltzmann's constant and T is operating temperature in kelvin.

When the cathode operated at an elevated temperature $t_{Elevated}$ for a time of $T_{Elevated}$, then total amount of evaporated barium can be calculated using equation (4.3) as

$$M_{Total} = M \times t_{Elevated} = K \exp\left\{-\left(\frac{e\varphi}{kT_{Elevated}}\right)\right\}$$

$$M = \frac{1}{t_{Elevated}} \times K \exp\left\{-\left(\frac{e\varphi}{kT_{Elevated}}\right)\right\} \tag{4.4}$$

Since the barium evaporation is a function of time and temperature, it can be assumed that M_{Total} amount of barium can be evaporated at an operating

temperature ($t_{Operating}$) for a unknown time $T_{Operating}$. Again equation (4.3) can be written as

$$M_{Total} = M \times t_{Operating} = K \exp\left\{-\left(\frac{e\varphi}{kT_{Operating}}\right)\right\}$$

$$M = \frac{1}{t_{Operating}} \times K \exp\left\{-\left(\frac{e\varphi}{kT_{Operating}}\right)\right\} \tag{4.5}$$

Equation (4.4) and (4.5) can be written as

$$\frac{1}{t_{Elevated}} \times K \exp\left\{-\left(\frac{e\varphi}{kT_{Elevated}}\right)\right\} = \frac{1}{t_{Operating}} \times K \exp\left\{-\left(\frac{e\varphi}{kT_{Operating}}\right)\right\}$$

$$t_{Operating} = t_{Elevated} \times \frac{\exp\left\{-\left(\frac{e\varphi}{kT_{Operating}}\right)\right\}}{\exp\left\{-\left(\frac{e\varphi}{kT_{Elevated}}\right)\right\}}$$

$$t_{Operating} = t_{Elevated} \times \exp\left\{-\left(\frac{e\varphi}{k}\right) \times \left(\frac{1}{T_{Elevated}} - \frac{1}{T_{Operating}}\right)\right\} \tag{4.6}$$

From accelerated life test data and using equation (4.6) actual life at operating temperature can be estimated. The accelerated life test data showed that the cathode continues to operate of average current density 15 A/cm^2 at 1120°C for ~2500 hour without any emission degradation. The extrapolation data shows that this kind of cathode can be operated for ~12,000 hours at an operating temperature 1050^0C.

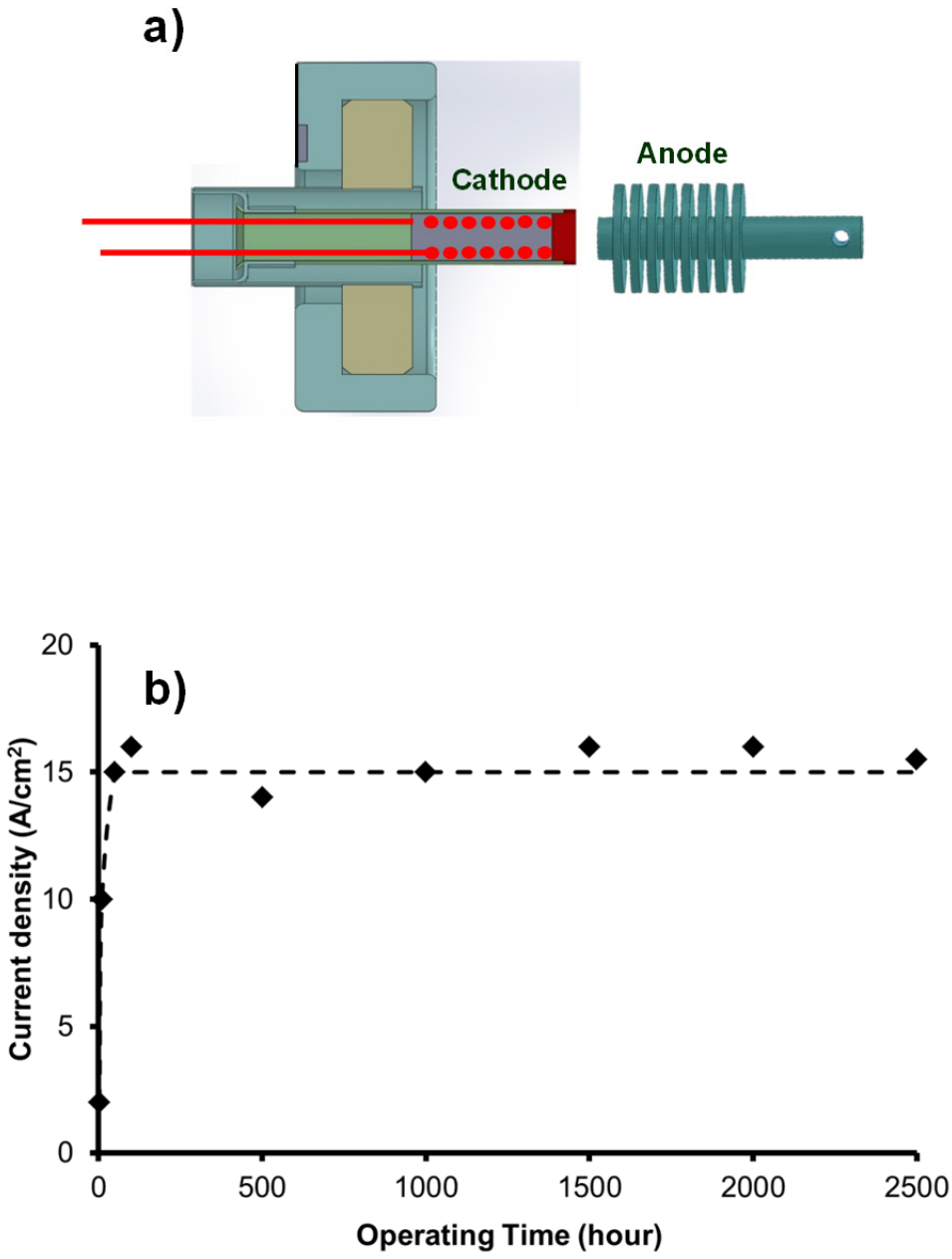

Figure 4.14: (a) Schematic diagram of diode assembly, (b) Plot of cathode life with time.

CHAPTER 5

Discussion of results, conclusions, and suggestions for future work

5.1 Study of cathode matrix parameters

5.2 Study of various physical parameters of nanoparticles

5.3 Synthesis and characterization of nanoparticles

5.4 Fabrication and characterization of cathode

5.5 Suggestions for future work

The primary influencing factor on emission is of the diffusion of active material from bulk to the surface which is influenced by the pore parameters. Therefore, simulations were carried out on the pore parameters such as porosity, pore geometry, pore distribution, and inter-pore connectivity. It was found that void porosity is to be kept between 15% to 20% for proper surface coverage of active material for better emission and longevity. The studies also reveal that the particle size should be spherical in shape for better transportation of active material from bulk to the surface. The parameters of the *sol-gel* process were required to be controlled to achieve spherical shaped particles of uniform size with homogeneous doping.

In addition to the diffusivity, another factor of importance is of surface roughness, which influences the emissivity and hence the emission from the cathode surface for a given heater power. Theoretical studies were carried out on the influence of various parameters of the emissivity. This exercise helps to understand, quantitatively, the maximum allowable roughness of the surface that has a bearing on the emission current. A few pellets were made out of the above nanopowder by using a die-punching technique. The surface roughness parameters of the pellet were measured using a surface profiler. The emissivity corresponding to these roughness parameters was estimated. A good agreement was found between the simulated and measured values.

To understand the influence of sintering temperature on the parameters of porosity, six pellets (made out the above powder) were sintered at different temperatures. It was observed that at elevated temperatures, the porosity is reduced, the shape is distorted, and that the particles started loosing their spherical shape due to the inter-particle diffusion/agglomeration. On the other hand at low sintering temperatures, the compactness is lost and the pellets cannot retain their shape. These studies revealed a vital information on the choice of the temperature that the sintered pellet has to have enough strength to retain its compactness while the nanoparticles do not grossly loose their spherical shape.

The cathodes were assembled in an UHV system for emission and for surface characterization. The current densities of up to 100A/cm^2 were drawn. The I-V characteristics exhibited field enhancement. This is attributed to the formation

of a thick active layer. AES studies supported this view. As the cathode has copious emission, it is proposed for use in a THz device where high current density is a critical requirement.

Discussion of results on the above work and the conclusions are given below. Future work to be carried is proposed for a better understanding of emission mechanism and for enhancement of emission.

5.1 Study of cathode matrix parameters

The following parameters are studied with a view to obtain high current density.

a) **Surface roughness:** For a cathode made out of nanoparticles, the surface roughness is primarily decided by the roughness of the die-punch used. The surface finish of the pellet takes exact surface finish of die-punch used as the particles of the powder are in nanoscale. Therefore, it became essential to estimate maximum allowable surface roughness in order to achieve high emission. As seen in the plot of current density (J) versus surface roughness (R_a) shown in figure 3.15, J falls rapidly beyond 0.5μm of R_a. From this plot it can be inferred that it is necessary to keep the roughness below 0.5μm.

b) **Optimization of porosity and pore parameters:** Pore parameters, *viz.* porosity, pore geometry, pore distribution and inter-pore connectivity, influence the cathode emission and its life. Therefore, a study was carried out on these pore parameters with an aim to achieve optimum coverage of active material that results in high emission. The porosity was theoretically calculated using transmission and evaporation rate of active material through the porous matrix. As per the plots of figure 3.5, higher the porosity higher the transmission, which is indicative of the diffusion of active material. On the contrary, lower the porosity lower would be the transmission and hence low emission. It is concluded that for long life and high emission, an optimum range of porosity would be between 15% to 20%.

5.2 Study of various physical parameters of nanoparticles

The influence of the physical parameters on the barium flow rate and its distribution across the cathode surface was studied using COMSOL multi-physics software. Three different types of particles, (i) arbitrary shape, (ii) spherical shape with non-uniform size and (iii) spherical shape with uniform size, were considered in this simulation. As per the results shown in figure 3.9, it is clear that in the case of a matrix made out of spherical shaped and uniform size particles, the Ba/BaO arrival rate is lowest and at the same time the coverage is uniform across the cross section. Therefore, the pellet of spherical shaped and uniformly distributed nanoparticles is an optimum choice for high current density and for long life.

5.3 Synthesis and characterization of nanoparticle

Sc_2O_3-doped tungsten nanoparticles were synthesized using a *sol-gel* method. The studies were carried out using SEM and TEM in order to find out the shape and size of the particles. As per the SEM and TEM images, it is clear that the shape of the particles is spherical with an average diameter of 100nm. The spherical morphology is desired from the view point of better pore distribution and inter-pore connectivity. In order to find out the homogeneity of scandium, EDS was carried out on the powder. As per the results of table 2.1, scandium is distributed fairly uniformly. This is desired to achieve uniform emission. Another parameter of importance is particle size distribution which has a bearing on the inter-pore connectivity. Dynamic light spectroscopy (DLS) technique was used to characterize the uniformity of size. As per figure 2.10, it is clear that the relative standard deviation increases from 12.7% to 17.2% with reduction temperature (of *sol-gel* process) increasing from 700^0C to 1000^0C. This is attributed to the diffusion of particles and/or inter-particle coagulation at high temperature. It is suggested that in final phase of sol-gel process, hydrogen reduction temperature should be kept below 700^0C to obtain uniform sized nanoparticles.

The synthesis method adopted here showed that the particle characteristics can be precisely controlled by the process parameters, demonstrating that this

method is capable of improving the particle quality. This synthesis approach is certainly superior as compared to other available synthesis methods [35]-[39]. Thus, the spherical shape, homogeneous doping, and uniform size distribution scandia-doped tungsten nanoparticles obtainable by the *sol-gel* method prove the potential application for the development of a high current density dispenser cathode.

5.4 Fabrication and characterization of cathode

To gain further confidence on the above studies related to pore parameters, surface roughness, particle geometry, and thermal aspects a complete cathode assembly has been made and characterized for emission and surface chemistry. The discussion and conclusions on the fabrication and characterization are as given below:

(a) Fabrication of cathode assembly: It was found that in the case of low temperature sintering, the pellet did not retain its shape and crumpled while handling. At higher temperature sintering, the pellet as well as the pores started shrinking. This posed a serious problem in introducing the active material into the matrix through impregnation. Therefore, an alternate method has been adopted to avoid impregnation. The active components Ba-Ca-aluminates were taken in carbonate form and were mixed with the Sc-doped tungsten powder using agate mortar. The mixture was then pressed using a specially designed die-punch. The surfaces of die and punch were polished to a mirror finish using a fine sand paper at high rpm. Four cathodes were made, out of which two (S-W_01 and S-W_02) were sintered at 1700^0C while the other two (S-W_03 and S-W_04) at 1500^0C.

(b) Characterization of cathodes: After full activation, which took about 200 hours, pulse emission measurements were carried out at a low duty ratio to avoid arcing and high joule heating. It was found that the emission of S-W_01 and S-W_02 was poor. The AES studies showed (figure 4.13) a low coverage of active material (Ba/BaO) on the surface. This is attributed to the evaporation

of Ba/BaO during the sintering at elevated temperature (1700^0C). The other two cathodes were also tested in the UHV system. The emission results are highly encouraging as shown in figure 4.9. The current density of up to 100A/cm^2 was obtained in the partial saturation region; while in full space charge region, emission of up to 60A/cm^2 was obtained. The work function was found to be 1.75eV, which is similar to that of an alloy coated cathode [2].

The I-V characteristics clearly depict a non-saturation behavior (field enhancement) at higher anode fields. This behavior is attributed to the formation of a substantially thick semiconducting active layer on the surface. This can be further corroborated with the AES data as shown in figure 4.10 which shows a high coverage of active material as compared to a conventional impregnated (B-type) cathode [3]. The presence of scandium can be seen from the low energy peaks in figure. 4.11(a) and figure 4.11(b). Scandium is present in the form of scandia (Sc_2O_3) which is evident from the doublet [2] at 360eV in figure 4.11(b).

It is concluded that the high emission and the field enhancement of the present cathodes are due to the formation of a thick active layer on the surface.

5.5 Suggestions for future work

Based on the work carried out so far, the following suggestions are made for future work for a better understanding of emission mechanism and for enhancement of emission.

(a) **Use of RGA for measurement of evaporation rate**: As explained in section 3.1.2 the transmission coefficient (α), which is also a measure of diffusion, depends on pore properties. From figure 3.5, the value of α increases with porosity which in turn affects the life of cathode. It will be highly useful to study these aspects by making pellets of different porosities and measure the evaporation rate using residual gas analyzer (RGA) to validate the present theoretical results.

(b) **Depth profiling using ion gun:** The field enhancement as observed from the I-V characteristics (figure 4.9) is attributed to the formation of a thick active layer. It would be helpful to carry out depth profiling studies by removing partial layers using an ion gun and finding out the corresponding surface composition using AES. These studies will help to find out the exact thickness of the active layer. Using Raju-Maloney model [3], it would be possible to estimate the exact field enhancement and validate the results with the experimental data.

(c) **Surface roughness:** The theoretical studies on the surface roughness (section 3.3) show that the surface roughness affects the emission as the radiating power would be higher for a higher value of roughness. It would be worthwhile to study cathodes of differing surface roughness and the corresponding emission to validate the theoretical results.

(d) **Use of THEM to study spatial emission distribution:** In the present work, tungsten and scandium were mixed homogeneously using sol-gel process. Due to this, the emission uniformity is expected to be better than that of a conventional impregnated scandate cathode. The studies using THEM will give insight into the emission distribution and will strengthen the R&D work on nanoparticle-based scandate cathode.

Bibliography

[1] P. Zalm and A. J. A. and Van Stratum, "Osmium dispenser cathodes," vol. 27, no. 3/4, pp. 69-75, 1966.

[2] R. S. Raju, "Impregnated cathodes for use in high power microwave tubes," Ph.D. Thesis, Corpus Christi College, Cambridge University, February 1987.

[3] R. S. Raju and C. E. and Maloney, "Characterization of Impregnated Scandate using a semiconductor model," *IEEE Transaction on Electron Devices*, vol. 41, pp. 2460-2465, Dec. 1994.

[4] A. Figner, A. Soloveichik, and I. and Judinskaya, "Metal Porous Body Having Pores Filled with Barium Scandate," US Patent 3358178, Dec. 1967.

[5] R. S. Raju, "Studies on W-Re Mixed-Matrix Cathodes," *IEEE Transactions on Electron Devices*, vol. 56, no. 5, pp. 786-793, 2009.

[6] A. Wehnelt, "Oxide coated cathode," *Annalen der Physik*, vol. 14, p. 425, 1904.

[7] H. J. Lemmens, M. J. Jansen, and R. and Loosjes, "A new thermionic cathode for heavy loads," *Philips Technical Review*, vol. 11, pp. 341-350, 1950.

[8] R. C. Hughes, P. P. Coppola, and E. S. and Rittner, US Patent 2 700 118, Nov. 1951.

[9] R. C. Hughes, P. P. Coppola, and H. T. and Evans, "Chemical reaction in barium oxide on tungsten emitters," *Journal of Applied Physics*, vol. 23, pp. 635-641, 1952.

[10] A. V. Stratum, J. V. Os, J. R. Blatter, and P. and Zalm, "Barium-Aluminum-Scandate Dispenser Cathode," US Patent 4007393, 1977.

[11] A. V. Oostrom and L. and Augustus, "Activation and early life of a pressed barium scandate cathode," *Applied Surface Science*, vol. 2, pp. 173-186, 1979.

[12] S. Taguchi, T. Aida, and S. and Yamamoto, "Investigation of Sc_2O_3 Mixed-Matrix Ba-Ca Aluminate-Impregnated Cathodes," *IEEE Transactions on Electron Devices*, vol. 31, no. 7, pp. 900-903, 1984.

[13] J. Hasker and J. E. and Crombeen, "Scandium Supply After Ion Bombardment on Scandate Cathodes," *IEEE Transactions on Electron Devices*, vol. 37, no. 12, pp. 2589-2594, 1990.

[14] J. Hasker, J. V. Esdonk, and J. E. and Crombeen, "Properties and manufacture of top-layer scandate cathodes," *Applied Surface Science*, vol. 26, pp. 173-195, 1986.

[15] S. Yamamoto, S. Sasaki, S. Taguchi, I. Watanabe, and N. and Koganezawa, "Application of an Impregnated Cathode Coated with W-Sc_2O_3 to a High Current Density Electron Gun," *Applied Surface Science*, vol. 33-34, pp. 1200-1207, 1988.

[16] S. Yamamoto, I. Watanabe, S. Taguchi, S. Sasaki, and T. and Taguchi, "Formation mechanism of a Monoatomic Order Surface Layer on a Sc-Type Impregnated Cathode," *Jpn. Journal of Applied Physics*, vol. 28, pp. 490-494,

1989.

[17] J. Wang, et al., "A study of Scandia doped tungsten nano-powders," *Journal of Rare Earths*, vol. 25, pp. 194-198, 2007.

[18] J. Wang, et al., "A study of scandia and rhenium doped tungsten matrix dispenser cathode," *Solid State Sciences*, vol. 9, pp. 924-932, 2007.

[19] Y. Wang, et al., "Correlation Between Emission Behavior and Surface Features of Scandate Cathodes," *IEEE Transactions on Electron Devices*, vol. 56, no. 5, pp. 776-785, 2009.

[20] J. Wang, et al., "Sc_2O_3–W matrix impregnated cathode with spherical grains," *Journal of Physics and Chemistry of Solids*, vol. 69, pp. 2103-2108, 2008.

[21] Y. Wang, J. Wang, W. Liu, K. Zhang, and J. and Li, "Development of High Current-Density Cathodes With Scandia-Doped Tungsten Powders," *IEEE Transactions on Electron Devices*, vol. 54, no. 5, 2007.

[22] Y. M. Shin, J. Zhao, L. R. Barnett, and N. C. and Lumann, "Investigation of terahertz sheet beam traveling wave tube amplifier with nanocomposite cathode," *Physics of Plasmas*, vol. 17, 2010.

[23] G. Gartner, P. Geittner, H. Lydtin, and A. and Ritz, "Emission properties of top-layer scandate cathodes prepared by LAD," *Applied Surface Science*, vol. 111, pp. 11-17, 1997.

[24] E. S. Rittner, R. H. Ahlert, and W. C. and Ruttledge, "Studies on mechanism of operation of L-cathode - I," *Journal of Applied Physics*, vol. 28, no. 2, Feb. 1957.

[25] H. Eisele, "Recent advances in the performance of InP Gunn devices and GaAs tunnel diodes for the 100-300 GHz frequency range and above," *IEEE Trans. on Microwave Theory and Techniques*, vol. 48, p. 626, 2000.

[26] P. Siegel, "Terahertz Technology," *IEEE Transactions on Microwave Theory and Techniques*, vol. 50, no. 3, pp. 910-928, 2002.

[27] J. e. a. Faist, "Quantum cascade laser," *Science*, vol. 264, p. 553, 1994.

[28] B. S. ,. e. a. Williams, "Terahertz quantum cascade laser operating up to 137 K," *Applied Physics Letter*, vol. 83, p. 5142, 2003.

[29] K. Kan, et al., "Multimode terahertz-wave generation using coherent Cherenkov radiation," *Applied Physics Letters*, vol. 99, 2011.

[30] J. H. Booske, et al., "Vacuum Electronic High Power Terahertz Sources," *IEEE Transactions on Terahertz Science and Technology*, vol. 1, no. 1, pp. 54-75, 2011.

[31] J. K. So, et al., "Experimental Study on 100GHz Two-Step LIGA-based Backward Wave Devices," *IEEE International Vacuum Electronics Conference*, pp. 1-2, 2007.

[32] S. S. Ponomarenko, et al., "400-GHz Continuous-Wave Clinotron Oscillator," *IEEE Transactions on Plasma Science*, vol. 41, no. 1, pp. 82-86, Jan. 2013.

[33] Q. L. Liu, et al., "A THz Backward-Wave Oscillator Based on a Double-Grating Rectangular Waveguide," *IEEE Transactions on Electron Devices*, vol. 60, no. 4, pp. 1463-1468, 2013.

[34] G. A. Komandin, et al., "BWO Generators for Terahertz Dielectric Measurements," *IEEE Transactions on Terahertz Science and Technology*, 2013.

[35] J. Zhao, et al., "Scandate Dispenser Cathode Fabrication for A High-Aspect-Ratio High-Current-Density Sheet Beam Electron Gun," *IEEE Transactions on Electron Devices*, vol. 59, no. 6, pp. 1792-1798, 2012.

[36] K. Murugan, S. B. Chandrasekhar, and J. and Joardar, "Nanostructured a/ß-tungsten by reduction of WO_3 under microwave plasma," *International Journal of Refractory Metals and Hard Materials*, vol. 29, pp. 128-133, 2011.

[37] H. Zhang, L. Bai, P. Hu, F. Yuan, and J. and Li, "Single-step pathway for the synthesis of tungsten nanosized powders by RF induction thermal plasma," *International Journal of Refractory Metals and Hard Materials*, vol. 31, pp. 33-38, 2012.

[38] E. Oda, H. Fujiwara, and K. and Ameyama, "Nano grain formation in tungsten by severe plastic deformation-mechanical milling process," *Mater Trans JIM*, vol. 49, pp. 54-70, 2008.

[39] H. H. Nersisyan, H. I. Won, C. W. Won, and K. C. and Cho, "Combustion synthesis of nanostructured tungsten and its morphological study," *Powder Technol*, vol. 189, pp. 422-425, 2009.

[40] Y. S. Kwon, et al., "Features of passivation, oxidation and combustion of tungsten nano-powders by air," *International Journal of Refractory Metals and Hard Materials*, vol. 22, no. 6, pp. 235-241, 2004.

[41] R. Sarathi, T. K. Sindhu, S. R. Chakravarthy, A. Sharma, and K. V. and Nagesh, "Generation and characterization of nano-tungsten particles formed by wire explosion process," *J Alloys Compd*, vol. 475, 2009.

[42] S. Aravinth, B. Sankar, S. R. Chakravarthy, and R. and Sarathi, "Generation and characterization of nano tungsten oxide particles by wire explosion process," *Materials Characterization*, vol. 62, pp. 248-255, 2011.

[43] Z. Zhou, Y. Ma, J. Du, and J. and Linke, "Fabrication and characterization of ultra-fine grained tungsten by resistance sintering under ultra-high pressure," *Materials Science and Engineering: A*, vol. 505, pp. 131-135, 2009.

[44] J. Ma, Y. Du, and Y. and Qian, "A convenient thermal decomposition-co-reduction synthesis of nano-crystalline tungsten disilicide," *Bulletin of Materials Science*, vol. 28, no. 5, pp. 511-513, 2005.

[45] H. Lei, et al., "Synthesis of tungsten nanoparticles by sonoelectrochemistry," *Ultrasonics Sonochemistry*, vol. 14, pp. 81-83, 2007.

[46] P. K. Sahoo, et al., "Synthesis of tungsten nanoparticles by solvothermal decomposition of tungsten hexacarbonyl," *International Journal of Refractory Metals and Hard Materials*, vol. 27, pp. 784-791, 2009.

[47] C. Yuntao, W. Jinshu, L. Wei, and X. and Wang, "Effect of scandia on tungsten oxide powder reduction process," *Journal of Rare Earths*, vol. 28, pp. 202-205, 2010.

[48] C. J. Hou, X. Z. Diao, Y. K. Tang, D. Q. Huo, and L. F. and Wei, "Preparation and characterization of WO_3 nano-powder with microemulsion method," *IEEE*

International on Nanoelectronics Conference, 2008.

[49] H. H. Nersisyan, J. H. Lee, and C. W. and Won, "A study of tungsten nanopowder formation by self-propagating high-temperature synthesis," *Combustion and Flame*, vol. 142, pp. 241-248, 2005.

[50] A. L. Patterson, "The Scherrer Formula for X-Ray Particle Size Determination," *Physical Review Letters*, vol. 56, p. 978, Nov. 1939.

[51] J. W. Gibson and R. E. and Thomas, *Applied Surface Science*, vol. 16, p. 163, 1983.

[52] R. T. Longo, "Long life high current density cathodes," *Int. Elect. Defr. Meet. Tech. Digest, IEEE*, vol. 152, 1978.

[53] W. C. Rutledge and E. S. and Rittner, "Studies on the Mechanism of Operation of the L Cathode," *Journal of Applied Physics*, vol. 28, 1957.

[54] J. M. Roquaisa, et al., "Barium depletion study of impregnated cathodes and lifetime prediction," *Applied Surface Science*, vol. 215, pp. 5-17, 2003.

[55] E. Haslund, B. D. Hansen, R. Hilfer, and N. and Bjarne, "Measurement of local porosities and dielectric dispersion for a water-saturated porous medium," *Journal of Applied Physics*, vol. 76, no. 9, pp. 5473-5480, 1994.

[56] Y. Y. Lau, "Effects of cathode surface roughness on the quality of electron beams," *AIP Journals & Magazines*, vol. 61, no. 1, pp. 36-44, 1987.

[57] J. L. Cronin, "Modern dispenser cathodes," *IEEE Proceding on Solid-State and Electron Devices*, vol. 128, no. 1, Feb. 1981.

[58] C. D. Wen and I. and Mudawar, "Modeling the effects of surface roughness on the emissivity of aluminum alloys," *International Journal of Heat and Mass Transfer*, vol. 49, pp. 4279-4289, 2006.

[59] R. O. Jenkins, "A review of thermionic cathodes," *Vacuum*, vol. 19, no. 8, pp. 353-359, 1966.

[60] A. S. Gilmour Jr, *Principles of Travelling Wave Tube*. Artech House, 1994.

[61] U. Singh, et al., "Thermal and structural analysis of MIG for gyrotron," *J. Fusion Energy*, vol. 30, no. 2, pp. 176-179, 2011.

[62] L. Yao, K. Zhang, H. Yu, T. Huang, and B. and Li, "Thermal-structural analysis of electron gun with control grid," *Review of Scientific Instruments*, vol. 83, 2012.

List of Publications

1. **R.K. Barik**, A. Bera, A.K. Tanwar, I.K. Baek, S.H. Min, O.J. Kwon, W.S. Lee, G.-S. Park, "A novel approach to synthesis of scandia-doped tungsten nano-particles for high-current-density cathode applications," *International Journal of Refractory Metals and Hard Materials*, vol. 38, pp. 60-66, May 2013.
2. **R.K. Barik**, A. Bera, R.S. Raju, A.K. Tanwar, I.K. Baek, S.H. Min, O.J. Kwon, M.A. Sattorov, K.W. Lee, G.-S. Park, "Development of alloy-film coated dispenser cathode for terahertz vacuum electron devices application," *Applied Surface Science*, vol 276, pp 817-822, July 2013.
3. A. Bera, **R. K. Barik**, M. A. Sattorov, O. Kwon, S. H. Min, I.-K. Beak, S. Kim, J.-K. So, and G.-S. Park, "Surface-coupling of Cerenkov radiation from a modified metallic metamaterial slab via Brillouin-band folding," *Optics Express*, 2014.
4. O. Kwon, J.-K. So, A. Srivastava, M. Sattorov, **R. K. Barik**, A. Bera, A. K. Tanwar, S.-H. Park, I.-K. Baik, J.-H. Choi, J. Kim, J.-W. Yang, J.-H. Kim, S.-S. Chang, and G.-S. Park. "Micro-fabricated millimeter wave vacuum electronic devices." *in Proc. 35th Int. Conf. IRMMW-THz, Rome, Italy*, Sep. 5-10, 2010.
5. **R. K. Barik**, A. K. Tanwar, A. Bera, O. Kwon, M. A. Sattorov, G.-S. Park, "High current density nano-particle dispenser cathode for THz vacuum electron devices." *in Proc. 2nd Int. THz-Bio Workshop, SNU, Seoul, Korea*, p. 47 (P-1), Jan. 19-20, 2011.
6. **R. K. Barik**, A. K. Tanwar, A. Bera, Ohjoon Kwon, M. A. Sattorov, G.-S. Park. "Investigation of emission mechanism of scandium doped nano particle dispenser cathode for THz vacuum electron devices." in Proc. 36th *Int. Conf. IRMMW-THz, Houston, TX, USA,* Oct. 2-7, 2011.
7. **R. K. Barik**, RS Raju, AK Tanwar, Supriyo Das and G. S. Park, "High Current Density Ternary-alloy-film Dispenser Cathode for Terahertz Vacuum Devices," *in Proc. IEEE IVEC, Bangalore, India*, Feb. 21-24, 2011.
8. **R. K. Barik**, RS Raju, Supriyo Das, and SnehRathore, "Design and Development of Thermionic Emission Microscope," in Proc. *IEEE IVEC, Bangalore, India,*Feb. 21-24, 2011.
9. A. Bera, O. Kwon, **R. K. Barik**, M. A. Sattorov, G.-S. Park, "Thermal issues in THz vacuum electron devices." *in Proc. 2nd Int. THz-Bio Workshop, SNU, Seoul, Korea*, p. 48 (P-2),Jan. 19-20, 2011.
10. M. A. Sattorov, A. Bera, **R. K. Barik**, O. Kwon, G.-S. Park, K. A. Lukin, A. S. Tishchenko, "Thermal velocity effects in sheet-beam for THz devices." *in Proc. 2nd Int. THz-Bio Workshop, SNU, Seoul, Korea*, p. 52 (P-5), Jan. 19-20, 2011.

11. O. Kwon, J.-K. So, M. Sattorov, **R. K. Barik**, A. Bera, A. K. Tanwar, S.-H. Park, I.-K. Baek, J.-H. Kim, S.-S. Chang, G.-S. Park, "CW/pulsed sub-THz wave system for biomedical applications." *in Proc. 2nd Int. THz-Bio Workshop, SNU, Seoul, Korea*, p. 59 (P-9),Jan. 19-20, 2011,

12. G.-S. Park, S. H. Min, M. A. Sattorov, O. J. Kwon, **R. K. Barik**, A. Bera. "High power terahertz activities at SNU." *in Proc. 8th International Workshop: Strong microwave and terahertz waves: sources and applications. Nizhniy Novgorod, Russia*, July 9-16, 2011.

13. A. Bera, O. Kwon, **R. K. Barik**, A. Tanwar, M. A. Sattorov, and G.-S. Park "Design of depressed collector for 95 GHz CCBWO." *in Proc. IEEE IVEC, Bangalore*, India, pp. 135-136, Feb. 21-24, 2011,

14. **R. K. Barik**, A. K. Tanwar, I. K. Baek, K. Eom, A. Bera, M. A. Sattorov, S. H. Min, O. Kwon, and G.-S. Park. "Effect of surface roughness of high current density nano-particle cathode for THz vacuum devices application." *in Proc. IEEE IVEC-IVESC, Monterey, USA*, p. 369, Apr. 24-26, 2012.

15. **R. K. Barik**, A. K. Tanwar, I. K. Baek. K. Eom, A. Bera, M. A. Sattorov, S.-H. Min, O. J. Kwon, G.-S. Park, "Development of high current density scandate cathode for terahertz vacuum devices application." *in Proc. 3rd Int. THz-Bio Workshop, SNU, Seoul, Korea*, p. P-2, Feb. 8-9, 2012.

16. **R. K. Barik**, A. Tanwar, I. K. Baek, K. Eom, A. Bera, M. Sattorov, S.-H. Min, O. Kwon, G.-S. Park. "Study of dispenser cathode development for terahertz vacuum devices application." *in Proc. 37th Int. Conf. IRMMW-THz, Wollongong (UOW), Australia*, Sep. 23-28, 2012.

17. A. Bera, M. A. Sattorov, O. J. Kwon, **R. K. Barik**, S.-H. Min, G.-S. Park, "Smith-Purcell radiation from metallic metamaterial grating." *in Proc. 3rd Int. THz-Bio Workshop, SNU, Seoul, Korea*, p. P-1, Feb. 8-9,2012.

18. M. A. Sattorov, E. Khutoryan, K. Lukin, G.-S. Park, A. Bera, **R. K. Barik**, O.-J. Kwon, S.-H. Min, A. Sharma, A. Tanwar, "Experimental analysis on 0.1 THz clinotron." *in Proc. 3rd Int. THz-Bio Workshop, SNU, Seoul, Korea*, p. P-3, Feb. 8-9,2012.

19. M. A. Sattorov, E. Khutoryan, K. Lukin, G.-S. Park, A. Bera, **R. K. Barik**, O.-J. Kwon, S.-H. Min, A. Sharma, A. Tanwar, "Automodulation processes in BWO with inclined electron beam at low focusing magnetic fields." *in Proc. 3rd Int. THz-Bio Workshop, SNU, Seoul, Korea,* p. P-4, Feb. 8-9,2012.

20. O. Kwon, J.-K. So, M. Sattorov, **R. K. Barik**, A. Bera, A. K. Tanwar, I.-K. Baek, S.-H. Min, J.-H. Kim, S.-S. Chang, G.-S. Park, "Microfabricated sub-terahertz vacuum electronic devices." *in Proc. 3rd Int. THz-Bio Workshop, SNU, Seoul, Korea*, p. P-5, Feb. 8-9, 2012.

21. S.-H. Min, O. Kwon, M. Sattorov, I. K. Baek, K.-H. Eom, H. Son, D-H. Choi, S.-H. Bak, S. Kim, A. Bera, **R. K. Barik**, K.-T. Kim, G.-H. Park, W.-Y. Park, J.-Y. Lee, S.-J. Cho, O. S. Kwon, G.-S. Park, "Biological effects by AC ns pulsed electromagnetic fields (EMF) at cm & mm waves exposures and DC ns

pulsed electric fields (nsPEF)." *in Proc. 3rd Int. THz-Bio Workshop, SNU, Seoul, Korea*, p. P-25, Feb. 8-9, 2012,.

22. A. Bera, **R. K. Barik**, S.-H. Min, O. Kwon, I. Baek, S. Kim, M. A. Sattorov, and G.-S. Park. "Enhanced SPR in frequency independent dielectric grating." *in Proc. IEEE IVEC-IVESC, Monterey, USA*, p. 157,Apr. 24-26, 2012,

23. M. Sattorov, E. Khutoryan, K. Lukin, G.-S. Park, A. Bera, **R. K. Barik**, O. Kwon, S.-H. Min, A. Sharma, A. Tanwar. "Experimental study on 0.1 THz Clinotron." *in Proc. IEEE IVEC-IVESC, Monterey, USA*, p. 453,Apr. 24-26, 2012.

24. S.-H. Min, O.-J. Kwon, M. A. Sattorov, J.-K. So, I.-K. Baek, S.-T. Kim, K.-H. Eom, A. Bera, **R. K. Barik**, Y.-M. Shin, W.-S. Lee, J.-H. S and G.-S. Park, "Studies on high power THz radiation using nanosecond pulse in oversized relativistic backward wave oscillator." *in Proc. IEEE IVEC-IVESC, Monterey, USA*, p. 4.19, Apr. 24-26, 2012.

25. A. Bera, **R. K. Barik**, O. Kwon, I. K. Baek, S. Kim, S.-H. Min, M. Sattorov, G.-S. Park. "Generation of THz radiation: Metamaterial grating versus lamellar grating." *in Proc. 37th Int. Conf. IRMMW-THz, Wollongong (UOW), Australia*, Sep. 23-28, 2012.

26. **R.K.Barik**, A. Bera, A.K. Tanwar, I.K. Baek, K. Eom, M.A. Sattorov, S.H. Min, O.J. Kwon, G-S. Park, "Sol-gel Synthesis of Sc_2O_3 Doped W Nano-particle for Cathode Application," in Proc. IEEE IVEC, Paris, May 21-23, 2013.

27. A. Bera, **R.K Barik**, M.A. Sattorov, O.J. Kwon, S.H. Min, G-S. Park, "Cherenkov-Like Radiation from Metallic Metamaterials," *in Proc. IEEE IVEC, Paris,* May 21-23, 2013.

28. S.H.Min,O.Kwon,M.Sattorov,I.K.Baek,S.T.Kim,A.Bera,**R.KBarik,**W.S.Lee,J. H.So,G.S.Park, "Power Estimation of Electromagnetic Coupling Effectiveness by a X-band Backward Wave Oscillator with Mode Conversion," *in Proc. IEEE IVEC, Paris*, May 21-23, 2013.

29. M. A.Sattorov, A. K.Tanwar,A.Bera,**R. K.Barik,** S. H.cMin,O.Kwon, G. S, Park, "Development on W-Band Coupled-Cavity Device," *in Proc. IEEE IVEC, Paris*, May 21-23, 2013.

30. A.K. Singh, M. Ravi, M.S. Bisht, **R.K. Barik**, S.K. Shukla, R. Prajesh, T.P. Singh, S.K. Saini, Asish Kumar, Rajesh Kumar, and R.S. Raju "Active sintered controlled porosity dispenser (CPD) cathode," *IVESC2014,* scheduled during 30th June to 4th July 2014 at Saint Petersburg, Russia.

31. M.S. Bisht, **R.K. Barik**, A.K. Singh, M. Ravi*, S.K. Shukla, and R.S. Raju, "Yttrium-doped Nano-Scandate Cathode for THz VED,"*IVESC201*4, scheduled during 30th June to 4th July 2014 at Saint Petersburg, Russia.

32. **R.K. Barik**, R.S Raju, M.S. Bisht, and G.S. Park , "Nano-particle Thermionic Cathode for THz Devices Application,"*IVESC2014*, scheduled during 30th June to 4th July 2014 at Saint Petersburg, Russia.

초 록

테라헤르츠(THz) 영역의 진공전자장치(VED)를 위해서는 100A/cm^{2}에 가까운 음극 전류밀도를 제공할 수 있는 음극으로부터 생성되는 높은 전류밀도의 전자빔이 필요하다. 기존의 B 타입의 음극으로는 대략 10A/cm^2 정도의 음극 전류밀도를 생성할 수 있기 때문에 높은 전류밀도와 높은 방출 균일도를 가진 소형 음극 개발이 요구되는 상황이다.

이 학위논문에서는 나노기술을 사용하여 테라헤르츠 진공전자장치에 사용될 수 있는 100A/cm^{2}의 전류밀도를 생성하는 음극을 설계하고 개발하는 것에 동기부여를 두었다. 열적 측면에 대한 이해와 방출 매커니즘 그리고 전자방출 능력을 향상시키기 위한 여러 파라미터(표면 거칠기, 기공률, 기공 형상, 기공 분포, 기공 간의 연결)의 영향에 대한 이론적 연구가 수행되었다. 분석결과 전자방출이 입자의 형태, 크기, 도핑의 균일성 및 입자 분포에 의해 영향을 받는 것으로 나타났다. 따라서 상기 요건을 가장 만족하는 나노입자 합성을 위한 화학 공정을 개발 하였다. 산화 스칸듐(Sc_2O_3)을 텅스텐에 추가하면 전자방출 정도가 텅스텐보다 10배 이상 향상된다고 알려져 있다. 시뮬레이션 결과 입자가 구의 형태를 가지고 있다면 활성물질이 내부에서 표면으로 증발되는 확산율이 낮아지는 것으로 나타났다. 스칸듐이 도핑된 구형 텅스텐 나노입자는 *sol-gel* 공정으로 합성할 수 있다. 합성된 나노입자의 형태는 주사전자현미경(Scanning Electron Microscope)과 투과전자현미경(Tunneling Electron Microscope)으로 측정하였으며, 도핑 균일성은 EDS분광법(Energy-dispersive X-ray Spectroscopy)으로, 입자의 순도는 X-선 회절(X-ray Diffraction)을 이용하였고, 입자의 크기 분포 및 균일도는 동적 광분광법(Dynamic Light Spectroscopy)을 사용하여 측정하였다. 측정결과 합성된 입자는 균일하게 도핑된 구형의 나노입자라는 것이 확인되었다.

또한 본 연구에서는 표면 거칠기가 전자방출에 미치는 영향에 대해서도 수행하였다. 방사표면에서 낮은 방사 손실을 얻기 위해서는 표면 거칠기가 500nm 이하가 되어야 한다는 것을 밝혔다. 합성한 나노입자는 매끈한 표면을 가진 특수 설계된 die-punch로 압력을 가해 눌러 펠렛 형태로 만들고 소결 후 개별 매립형 히터에 장착하였다. 초고진공 챔버내에서 만들어진 음극의 표면특성과 전자방출 측정은 AES 분광법 (Auger Electron Spectroscopy) 및 평판 양극을 이용하여 측정하였다. 측정된 전자 방출 결과는 매우 고무적인데, 제작된 음극이 $1080^{0}C_{B}$의 밝기 온도에서 $100A/cm^{2}$ 의 음극 전류 밀도를 달성함을 확인하였다. 일함수는 제로-전계 방출을 통해 1.75eV으로 계산되었다. 매우 흥미로운 점은 I-V 특성이 높은 양극 전계에서도 포화되지 않은 것이다. 전계 강화를 일으키는 음극표면의 충분히 두꺼운 반도체 활성층의 형성이 이러한 특성이 나타난 이유이다. 이는 B 타입 음극에 비해 높은 활성물질의 범위를 보여주는 AES 데이터에서도 확인 할 수 있다.

주요어: 솔-젤 합성, 나노입자 음극, 디스펜서 음극, 오제 전자 분광법, 테라헤르츠 음극, 나노입자 특성
학번: 2009-31253